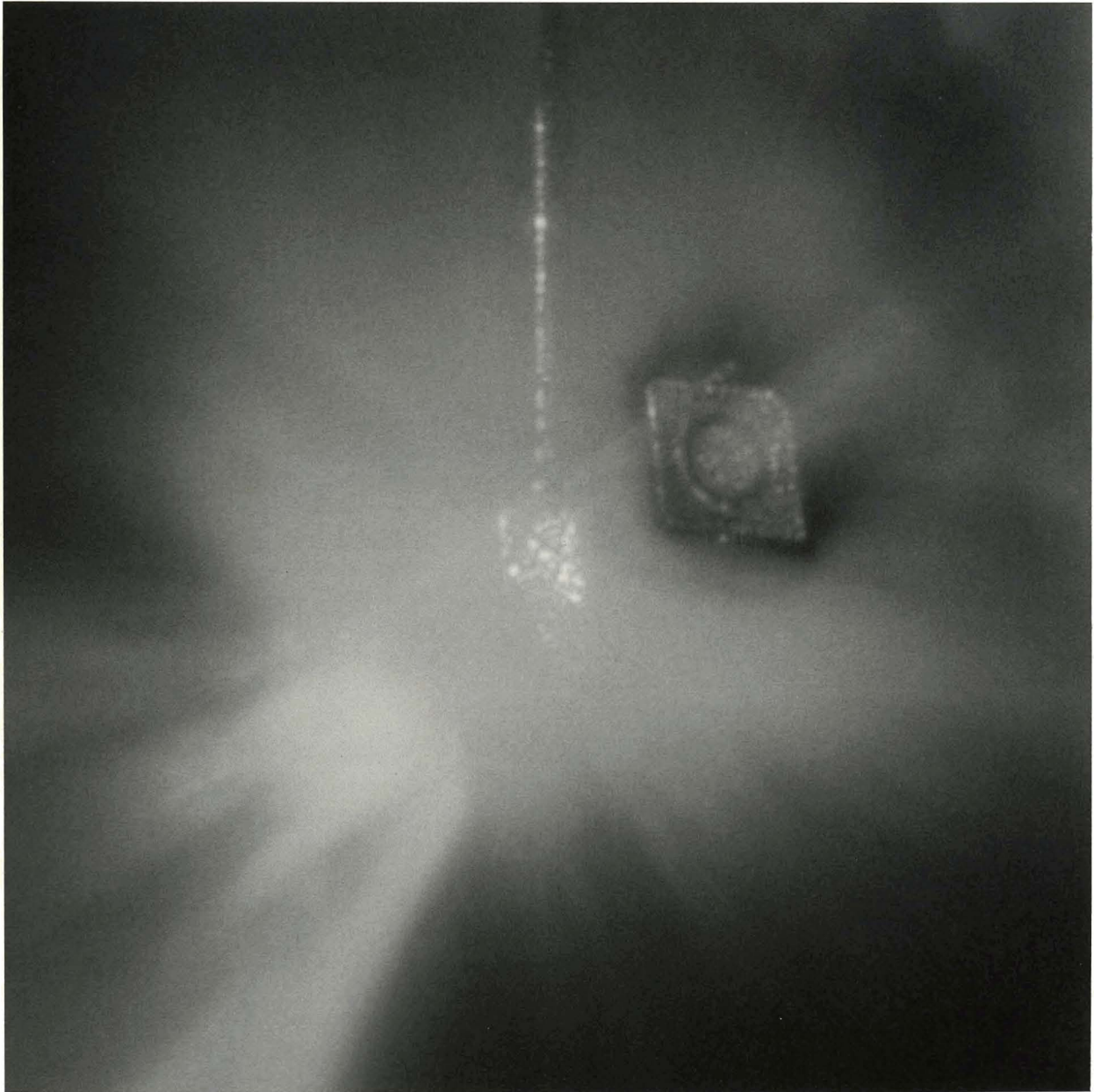


LLE Review

Quarterly Report



About the Cover:

Photograph of planar-foil target used for Rayleigh–Taylor growth-rate measurements on a shot to characterize the properties of the x-ray backlighter. The target is constructed of three foils: a uranium backlighter (bottom left); an aluminum debris shield (middle of field); and a CH drive foil with an imposed perturbation (upper right). In this photograph only the x-ray backlighter was irradiated with laser light.

This report was prepared as an account of work conducted by the Laboratory for Laser Energetics and sponsored by New York State Energy Research and Development Authority, the University of Rochester, the U.S. Department of Energy, and other agencies. Neither the above named sponsors, nor any of their employees, makes any warranty, expressed or implied, or assumes any legal liability or responsibility for the accuracy, completeness, or usefulness of any information, apparatus, product, or process disclosed, or represents that its use would not infringe privately owned rights. Reference herein to any specific commercial product, process, or service by trade name, mark, manufacturer, or otherwise, does not necessarily constitute or imply its endorsement, recommendation, or favoring by the United States Government or any agency thereof or any other sponsor. Results reported in the LLE Review should not be taken as necessarily final results as they represent active research. The views and opinions of authors expressed herein do not necessarily state or reflect those of any of the above sponsoring entities.

The work described in this volume includes current research at the Laboratory for Laser Energetics, which is supported by New York State Energy Research and Development Authority, the University of Rochester, the U.S. Department of Energy Office of Inertial Confinement Fusion under Cooperative Agreement No. DE-FC03-92SF19460, and other agencies.

Printed in the United States of America

Available from

National Technical Information Services

U.S. Department of Commerce

5285 Port Royal Road

Springfield, VA 22161

Price codes: Printed Copy A04

Microfiche A01

For questions or comments, contact David Harding, *Editor*, Laboratory for Laser Energetics, 250 East River Road, Rochester, NY 14623-1299, (716) 275-5850.

LLE Review

Quarterly Report



Contents

In Brief	iii
The Effect of Increased Irradiation Uniformity on Imprinting by 351-nm Laser Light	101
Single-Mode Rayleigh–Taylor Growth-Rate Measurements with the OMEGA Laser System	106
Fabrication of Polyimide Shells for Use as ICF Targets	113
Sideward Stimulated Raman Scattering of a Short Laser Pulse in a Plasma Channel	127
Picosecond Photoresponse in Polycrystalline Silicon	132
Thermal Distortions in Laser-Diode– and Flash-Lamp–Pumped Nd:YLF Laser Rods	137
The OMEGA Target-Positioning System	145
Publications and Conference Presentations	

In Brief

This volume of the LLE Review, covering the period April–June 1997, includes an article discussing the results from recent experiments performed on OMEGA. These experiments used a new beam-smoothing device—distributed polarization rotators—in concert with existing techniques (distributed phase plates and 2-D smoothing by spectral dispersion) to improve the on-target uniformity of each beam. The result of this improved radiation uniformity was a substantive reduction in imprinting—the nonuniformity caused by the laser. A novel way to study the time dependence of this imprinting is also presented in this article.

Additional highlights of the research presented in this issue are

- A study of the growth of mass perturbations due to the Rayleigh–Taylor hydrodynamic instability at the ablation interface. The observed growth of well-defined sinusoidal mass perturbations agreed well with data from the 2-D numerical simulation obtained using the hydrodynamic code *ORCHID*. The detailed analysis of these experiments showed that the determination of the Rayleigh–Taylor growth rate from the experimental x-ray radiograph data is problematic due to the evolution of the target density.
- A technique for fabricating polyimide target shells, together with preliminary material property data for the shells. This study represents the first successful attempt to make shells from polyimide. Polyimide shells withstand greater buckling and bursting pressures, and are more permeable, than existing hydrocarbon shells.
- A theoretical investigation of the spatiotemporal evolution of sideward stimulated Raman scattering in a plasma channel created by the ponderomotive expulsion of the plasma from the region of the laser-pulse axis. The partial reflection of Stokes light by the channel walls enhances the instability by allowing a spatial eigenmode to form in the laser pulse, which grows exponentially in time during the remainder of the pulse. The dependence of the growth rate of sideward SRS on the physical parameters is discussed.
- An experimental examination of the photoconductive impulse response in small-grain-polysilicon thin-film switches. The response was measured to have an upper limit of 3 and 36 ps at 0.8 and 1.55 μm , respectively. Understanding how to optimize this response time will improve the photoconductive switches used in the OMEGA electro-optic pulse-shaping system.

- A study of thermal distortion in xenon-flash-lamp– and laser-diode–pumped Nd:YLF laser rods using interferometric measurements. The thermal distortion was greatest in the flash-lamp–pumped rod; the dominant thermal distortions were astigmatism and defocus.
- A detailed engineering description of the design and operation of the OMEGA target positioner. This equipment allows a target to be precisely aligned using up to 4° of freedom: X , Y , Z , and ω ; a two-axis stage is available to provide θ and ϕ rotation.

David Harding
Editor

The Effect of Increased Irradiation Uniformity on Imprinting by 351-nm Laser Light

The experimental program¹ at LLE supports the national inertial confinement fusion (ICF) effort by performing experiments on OMEGA² to investigate the requirements for attaining ignition using direct-drive targets on the National Ignition Facility. One of the primary challenges in direct-drive ICF is to minimize perturbations in the target that are created by nonuniformities in the drive laser. These imprinted perturbations can seed the Richtmeyer–Meshkov (RM) and Rayleigh–Taylor (RT) instabilities that can amplify target nonuniformities sufficiently large enough to destroy an implosion. Typical high-gain implosions are expected to experience unstable growth factors in excess of 500.

One of the primary experimental efforts is to reduce imprinting by controlling irradiation nonuniformities. Other methods being studied include modifications to the target (foam buffers) and general reduction of growth rates; these methods will be reported on in the future. Eventually, successful ICF implosions may require some level of each of these methods. Here, we report on planar-target experiments that quantify the effect of changes to irradiation nonuniformity on imprinting. In addition, we report on “perturbing-beam” experiments—a novel method to measure the times over which imprinting occurs.

Drive nonuniformities conventionally are expressed in terms of spherical-harmonic ℓ -modes that describe the number of perturbation wavelengths contained in the circumference of a spherical target. The amplitudes of the low-order modes ($\ell \leq 8$) are affected by the configuration, pointing, and focusing of the beams, and by beam-to-beam power balance. In contrast, imprinting occurs predominantly in the high-order modes ($\ell \geq 8$), which largely result from nonuniformities in the intensity distributions of the individual beams. To reduce these nonuniformities, beam-smoothing techniques for glass lasers have traditionally relied on the physical optics associated with optical arrays placed in each of the laser beams. Distributed phase plates³ (DPP’s) act to randomize the phase across the beam wavefront, producing a speckle pattern with high-frequency modulations. Smoothing by spectral dispersion⁴ (SSD)

produces a variable frequency across the wavefront, producing multiple modes that are displaced in the target plane and, when averaged over time, smooth the DPP speckle nonuniformities. The DPP’s transform the long-wavelength beam nonuniformities (typical of high-power lasers) to wavelengths sufficiently short enough that displacements of the speckle pattern (caused by SSD) smooth out most of the nonuniformities.

Distributed polarization rotators⁵ (DPR’s) change the beam polarization across the wavefront (and therefore across the DPP), thereby diminishing the interference responsible for the high-frequency modulations in the DPP pattern. Since beams of orthogonal polarization do not interfere, the uniformity can be increased in proportion to the square root of the number of polarization states one produces in the wavefront, which in the case of the current DPR’s is 2.

To assess the irradiation uniformity, equivalent-target-plane (ETP) images of single beams with various beam-smoothing techniques have been analyzed. Beams with (1) DPP’s only, (2) DPP and 1-D SSD (1.5 Å), and (3) DPP and 2-D SSD (0.6 Å × 1.5 Å) were compared and, when measured over the duration of a 1-ns pulse, had time-averaged nonuniformities of 98%, 25%, and 12%, respectively.⁶ A recent implementation of DPR’s for OMEGA is shown in Fig. 71.1. A wedge of KDP (a birefringent material) is inserted such that the beam polarization bisects the ordinary and extraordinary axes. Since the element is wedged, the two orthogonally polarized beams emerge from the KDP at different angles, thereby producing two speckle patterns that are shifted by $\approx 80 \mu\text{m}$ [see Fig. 71.1(a)]. Since the two beams are orthogonally polarized, the two speckle patterns do not interfere and, therefore, produce a $1/\sqrt{2}$ ($N = 2$ beams) reduction in nonuniformity. This increase occurs instantaneously and is therefore particularly important to direct drive because irradiation imprinting occurs early in the drive and in some cases before appreciable SSD smoothing takes place. Figure 71.1(b) compares the uniformity of single beams with DPP’s only (i.e., no SSD), with and without DPR’s. To produce these plots, the square of the Fourier transform of the ETP images is integrated azimuthally

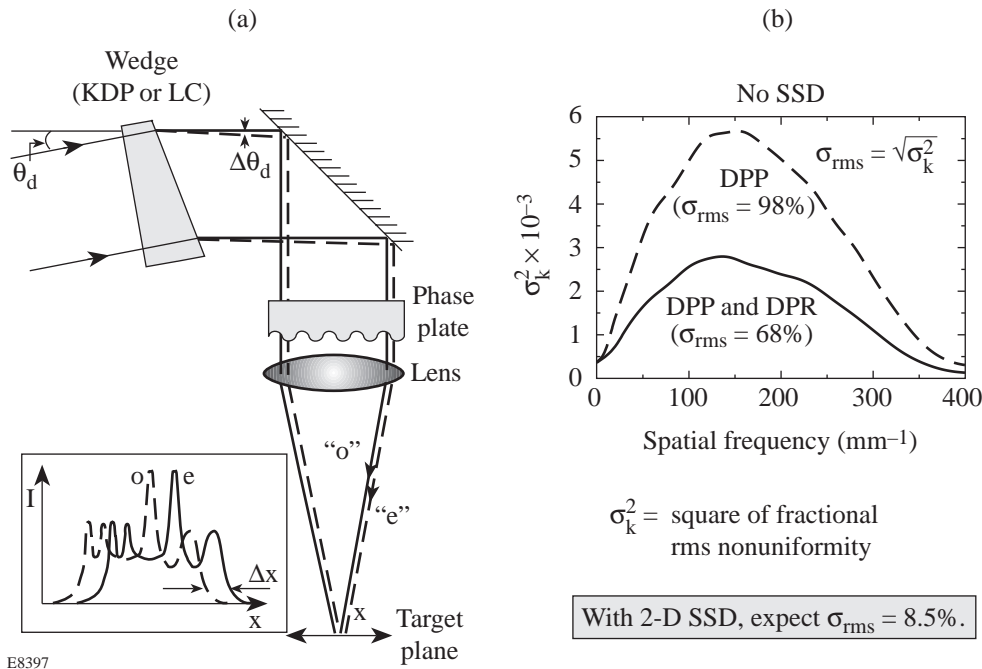


Figure 71.1

(a) Schematic of a DPR (a KDP wedge in the initial implementation on OMEGA) and (b) nonuniformity spectrum on target with and without DPR's for an OMEGA beam with phase plates (DPP's) but no SSD.

at constant radii, i.e., constant spatial frequency. The graphs are the square of the contribution (σ_k^2) to total nonuniformity as a function of spatial frequency. (The upper limit in frequency is the diffraction limit of the OMEGA lenses.) These graphs indicate that the $1/\sqrt{2}$ factor applied to σ_{rms} for the 2-D SSD result (above) should produce a time-integrated uniformity of 8.5% rms. Contributions to nonuniformity from film noise prevented this comparison from being performed on the 2-D SSD beams. We expect to use electronic imaging to further study the highly uniform beams.

Imprinting Experiments

Several multifoil, planar-target experiments were performed on OMEGA to study hydrodynamic instabilities. These experiments, which began on Nova as a collaboration between Lawrence Livermore National Laboratory (LLNL) and LLE,⁷ study two aspects of direct-drive target stability: growth rates and irradiation imprinting. Using x-ray radiography, the target trajectories and the growth of pre-imposed mass perturbation were measured in accelerated targets. These experiments were well simulated by hydrocodes, providing confidence that both the energy coupling⁸ and unstable growth⁹ are well modeled for these experiments. This confirmed our experience in similar experiments conducted on Nova.

The effect of irradiation nonuniformity on laser imprinting was studied using unperturbed CH₂ targets driven by five overlapped UV beams at 2×10^{14} W/cm² in 3-ns square

pulses. The targets were backlit with x rays produced by a uranium backlighter irradiated at $\sim 2 \times 10^{14}$ W/cm² (using 12 beams). X rays transmitted through the target were imaged using a framing camera with 8- μm pinholes filtered with 20 μm of Be and 12 μm of Al. This yielded highest sensitivity at an average photon energy of ~ 1.3 keV. Face-on radiographic images at different times were analyzed to measure the growth of perturbations seeded by imprinting. Since the initial perturbations are too small to be detected by this method, RT growth (driven by the target acceleration) is employed to amplify the imprint perturbations to detectable levels. Unfortunately, the addition of this highly nonlinear “amplifier” somewhat complicates interpretation of the results.

Figure 71.2 shows a series of radiographic images taken at 2.4 ns for each of four different laser configurations (all with DPP's): (a) no SSD, (b) 1-D SSD (1.5 Å), (c) 2-D SSD (0.6 Å \times 1.5 Å), and (d) DPR's and 2-D SSD (0.6 Å \times 1.5 Å). These configurations are listed in order of increasing on-target uniformity, which can be estimated by multiplying the time-integrated single-beam nonuniformities by $1/\sqrt{5}$ ($N=5$ beams), yielding 44%, 11%, 5.4%, and 3.8%, respectively, for the four configurations. Note, however, that at time equals zero, the first three cases present identical nonuniformities (i.e., the DPP speckle patterns) to the target. As time progresses, SSD provides time-averaged smoothing, the level of which depends upon the degree of SSD (bandwidth and number of dimensions). In contrast, the DPR's provide a $1/\sqrt{2}$ increase in

uniformity instantaneously (at time zero and all times) because two speckle patterns (from each beam) are continuously incident on the target.

Figure 71.3 depicts the nonuniformity “power spectra” obtained at different times from radiographic images of targets irradiated with various laser configurations. The spectra for the images in Fig. 71.2 (at 2.4 ns) are the top line in each graph. An estimate of the noise level for the diagnostic is shown as the gray regions. The nonuniformities depicted by these graphs result from acceleration-driven growth that is seeded by imprinting. Each point in these graphs is the azimuthal integral at constant radius (constant frequency) of the two-dimensional Fourier transform of the radiographic images. The summation

of each graph over all frequencies provides the square of the total rms deviation from a smooth envelope, i.e., the nonuniformities in that image. Note that, at a given time, the nonuniformities in these images decrease as the irradiation uniformity is improved. Since the pulse shape and drive intensities were the same, the growth rates are expected to be similar for all cases. The higher uniformity of the accelerated targets is, therefore, indicative of lower initial perturbation amplitudes, i.e., less imprinting. The smallest amount of imprinting occurs for the case with 2-D SSD and DPR’s. Inferences of the actual imprint amplitudes will be made using hydrodynamic simulations that have been normalized using the growth-rate data and include instrument response functions and noise levels.

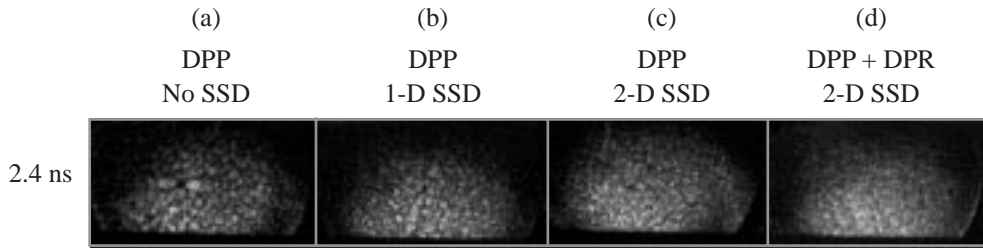


Figure 71.2 Radiographic images of 25- μm CH₂ foils taken at 2.4 ns and irradiated by 3-ns UV pulses having a variety of laser conditions (all with DPP’s): (a) no SSD, (b) 1-D SSD, (c) 2-D SSD, and (d) DPR’s and 2-D SSD. The latter images show higher uniformity of the accelerated target.

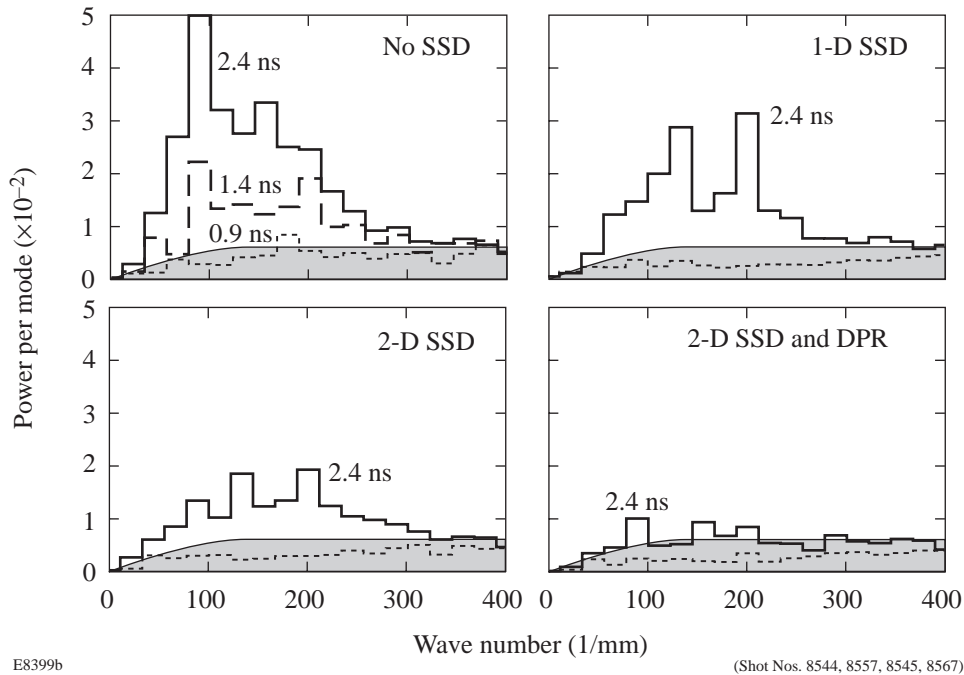


Figure 71.3 Measured nonuniformity power spectra of the x-ray backlighter transmission through accelerated CH foils subjected to a variety of laser-irradiation conditions. Fourier analysis of various x-ray framing camera images is shown for the times indicated. The maximum wave number shown (400 mm⁻¹) corresponds to a spatial wavelength of 16 μm .

This analysis is performed on the optical depth of the target (the natural log of the intensity-converted images). Using calibration targets, it is estimated that ratios of local intensities in Fig. 71.2(a) indicate that many RT “bubbles” have nearly penetrated the foil. The power spectra belie this point because the Fourier amplitudes correspond to modulations of less than $1\ \mu\text{m}$. This is because the target nonuniformities comprise a wide range of frequencies, so the individual amplitudes are relatively small. (This is in contrast to the single-mode experiments where the images are dominated by the imposed modulations.) Furthermore, one cannot estimate growth rates by tracking the amplitudes of individual modes at various times because the radiographic contrast of these measurements is sufficiently low that a significant amount of RT growth (linear and possible nonlinear) is needed to observe the target nonuniformities. This implies that saturation and possibly mode competition and coalescence dramatically affect the shape of the power spectrum. (In fact, many of our results exhibit a shift to longer wavelengths for late times.) Also, the MTF of the device has not been included in the measurements; if it were, the noise-dominated signal at shorter wavelength would appear as a dominant factor. To properly analyze these experiments we are investigating other image-analysis techniques and will use hydrodynamic simulations that include the instrument response. This is particularly important for spatial wavelengths $20\ \mu\text{m}$ and lower.

The time dependence of imprinting is important for determining the requirements for beam-smoothing rates. Imprint-

ing occurs until sufficient coronal plasma is produced and laser nonuniformities (those with wavelength shorter than the distance from the critical to the ablation surfaces) are smoothed by that plasma. Simulations¹⁰ indicate that for pertinent ICF conditions, irradiation nonuniformities decouple from the ablation surface after 300 to 500 ps. As shown above, SSD reduces imprinting, yet the addition of DPR’s shows continued reduction of imprinting. This indicates that imprinting occurs before this level of SSD smoothing is fully effective.

To understand the time over which imprinting occurs, a series of preliminary experiments were conducted on OMEGA before DPP’s and SSD were available. In these experiments, five beams without DPP’s accelerated initially smooth targets, and a sixth beam of smaller diameter was added at different times and with different energies. The relative effect of the sixth beam is gauged by observing the nonuniformities in the accelerated target. One can estimate the duration of imprinting by determining the perturbing-beam delay that no longer produces observable effects in the accelerated target.

For these experiments, the nominal drive beams were $1000\ \mu\text{m}$ in diameter and the perturbing beam was $400\ \mu\text{m}$. The drive intensity was $\sim 1 \times 10^{14}\ \text{W}/\text{cm}^2$ in 1-ns Gaussian pulses. Qualitatively, dramatic differences can be seen in the radiographic images for different conditions of the perturbing beam. Figure 71.4 depicts images from two shots with different timing of the perturbing beam. The upper images [Fig. 71.4(a)] show that, when timed 150 ps before the drive pulses, the

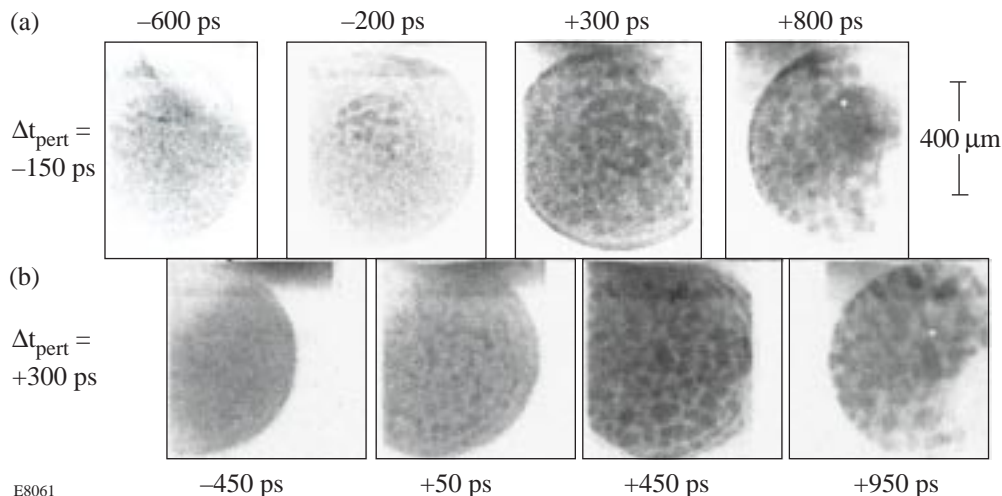


Figure 71.4

Framing camera images at various times relative to the peak of the Gaussian 1-ns drive beams for two shots: (a) perturbing beam at $-150\ \text{ps}$ and (b) perturbing beam at $+300\ \text{ps}$. The effect of the $400\text{-}\mu\text{m}$ -diam perturbing beam on the accelerated target uniformity is diminished when it arrives sufficiently late in time.

perturbing beam imprinted its features (smaller circle of nonuniformities) onto the target. The perturbing beam also produced similar effects when it was timed coincident (0 ps) with drive beams. Figure 71.4(b) shows the diminished effect of the perturbing beam when it is delayed by 300 ps with respect to the drive beams. This is likely the result of sufficient plasma formation (by the primary beams) to allow smoothing of the irradiation nonuniformities produced by the perturbing beam. In both cases, the perturbing beam had an intensity equal to the total drive-beam intensity, i.e., $\sim 1 \times 10^{14}$ W/cm². When the intensity of the perturbing beam was reduced to 7% of the drive beams' intensity, its effect was no longer observed in the radiographic images. The mottled patterns in Fig. 71.4 are the growth of features imprinted by the 1-mm drive beams. Similar features can be seen in the outer annulus of the images in Fig. 71.4(a). We expect that refinement of these experiments will provide insight into imprinting mechanisms and their time dependence, as well as provide information on the effectiveness of uniformity enhancements to the laser.

The next step in this effort will be to study the growth and mitigation of short-wavelength imprinting and to diagnose smaller amplitude perturbations. By relying less on the RT instability to amplify the perturbations, measurements performed at earlier times may provide better estimates of the spectrum and amplitude of imprinting. These measurements will require higher-resolution x-ray imaging ($<10 \mu\text{m}$) and higher-contrast measurements and will be attempted using a Kirkpatrick–Baez microscope or curved-crystal x-ray imaging, and high-resolution imaging of a 250-eV backlighter. In addition, imprint mitigation and growth-rate reduction will be studied using target modifications such as foam buffers and high-Z dopants.

Summary

The mitigation of the deleterious effects of laser imprinting in direct-drive ICF targets is crucial to LLE's experimental program. The primary approach—increased irradiation uniformity—has been shown to reduce imprinting levels, particularly for a new beam-smoothing device called distributed polarization rotator (DPR). The perturbing-beam experiments presented here demonstrate a novel way to study the time dependence of imprinting—an important issue for the design of certain uniformity schemes. To study imprinting earlier in time and perturbations with shorter wavelengths, we are investigating other diagnostics for radiography, including a number of advanced x-ray and XUV diagnostics.

ACKNOWLEDGMENT

This work was supported by the U.S. Department of Energy Office of Inertial Confinement Fusion under Cooperative Agreement No. DE-FC03-92SF19460, the University of Rochester, and the New York State Energy Research and Development Authority. The support of DOE does not constitute an endorsement by DOE of the views expressed in this article.

REFERENCES

1. R. L. McCrory, J. M. Soures, C. P. Verdon, T. R. Boehly, D. K. Bradley, R. S. Craxton, J. A. Delettrez, R. Epstein, P. A. Jaanimagi, S. D. Jacobs, R. L. Keck, J. H. Kelly, T. J. Kessler, H. Kim, J. P. Knauer, R. L. Kremens, S. A. Kumpan, S. A. Letzring, F. J. Marshall, P. W. McKenty, S. F. B. Morse, A. Okishev, W. Seka, R. W. Short, M. D. Skeldon, S. Skupsky, M. Tracy, and B. Yaakobi, in *Plasma Physics and Controlled Nuclear Fusion Research 1994* (IAEA, Vienna, 1996), Vol. 3, pp. 33–37.
2. T. R. Boehly, D. L. Brown, R. S. Craxton, R. L. Keck, J. P. Knauer, J. H. Kelly, T. J. Kessler, S. A. Kumpan, S. J. Loucks, S. A. Letzring, F. J. Marshall, R. L. McCrory, S. F. B. Morse, W. Seka, J. M. Soures, and C. P. Verdon, *Opt. Commun.* **133**, 495 (1997).
3. Y. Lin, T. J. Kessler, and G. N. Lawrence, *Opt. Lett.* **20**, 764 (1995); Laboratory for Laser Energetics LLE Review **65**, 1, NTIS document No. DOE/SF/19460-117 (1995). Copies may be obtained from the National Technical Information Service, Springfield, VA 22161.
4. S. Skupsky, R. W. Short, T. Kessler, R. S. Craxton, S. Letzring, and J. M. Soures, *J. Appl. Phys.* **66**, 3456 (1989).
5. Laboratory for Laser Energetics LLE Review **45**, 1, NTIS document No. DOE/DP40200-149 (1990). Copies may be obtained from the National Technical Information Service, Springfield, VA 22161.
6. T. Boehly, R. S. Craxton, P. A. Jaanimagi, R. L. Keck, J. H. Kelly, T. J. Kessler, R. L. Kremens, S. A. Kumpan, S. A. Letzring, R. L. McCrory, S. F. B. Morse, W. Seka, S. Skupsky, J. M. Soures, M. D. Tracy, and C. P. Verdon, in *Conference on Laser and Electro-Optics*, Vol. 9, 1996 OSA Technical Digest Series (Optical Society of America, Washington, DC, 1996), p. 324.
7. S. G. Glendinning, S. V. Weber, P. Bell, L. B. DaSilva, S. N. Dixit, M. A. Henesian, D. R. Kania, J. D. Kilkenny, H. T. Powell, R. J. Wallace, P. J. Wegner, J. P. Knauer, and C. P. Verdon, *Phys. Rev. Lett.* **69**, 1201 (1992).
8. D. D. Meyerhofer, J. P. Knauer, T. R. Boehly, D. Ofer, C. P. Verdon, P. W. McKenty, V. A. Smalyuk, O. Willi, and R. G. Watt, *Bull. Am. Phys. Soc.* **41**, 1480 (1996).
9. J. P. Knauer, D. D. Meyerhofer, T. R. Boehly, D. Ofer, C. P. Verdon, D. K. Bradley, P. W. McKenty, V. A. Smalyuk, S. G. Glendinning, and R. G. Watt, "Single-Mode Rayleigh-Taylor Growth-Rate Measurements with the OMEGA Laser System," to be published in the *Proceedings of the Thirteenth International Conference on Laser Interactions and Related Plasma Phenomena (LIRPP)*, Monterey, CA, 13–18 April 1997.
10. R. J. Taylor *et al.*, *Phys. Rev. Lett.* **76**, 1643 (1996).

Single-Mode Rayleigh–Taylor Growth-Rate Measurements with the OMEGA Laser System

Understanding the growth of perturbations due to hydrodynamic instabilities is important to the design of direct-drive targets for the National Ignition Facility (NIF). Direct-drive inertial confinement fusion (ICF) has the potential to be more efficient than indirect-drive ICF; however, there is the potential for greater growth of hydrodynamic instabilities due to the lower ablation velocities, which will prevent a NIF target from igniting. The primary instability of concern is the Rayleigh–Taylor (RT) instability, where a less dense fluid “supports” a more dense fluid and as such merits a thorough investigation. Direct-drive targets are subject to the RT instability twice during an ICF target implosion: first during the ablative acceleration phase of the implosion and second when the deceleration phase begins core assembly. Target imperfections and laser-irradiation nonuniformities act as amplitude seeds for the acceleration RT instability, while interior target imperfections and feedthrough of the ablation surface growth to the fuel–pusher interface act as amplitude seeds for the deceleration RT instability.

The importance of the RT instability problem is reflected in the number of experiments conducted^{1–5} to determine the RT growth rates in directly driven systems. Experiments of interest have used laser irradiation of 527 nm and 351 nm and have employed a number of beam-smoothing schemes. It is the development of these advanced laser-irradiation smoothing techniques like induced spatial incoherence (ISI)⁶ and smoothing by spectral dispersion (SSD)⁷ that has enabled the RT growth experiments to yield quantitative data. Without the beam-smoothing techniques, irradiation nonuniformity can dominate the experimental observables, even in initial-large-amplitude, single-mode, mass-perturbation experiments.

The RT growth rate at the ablation surface has typically been described by the Takabe⁸ or modified Takabe dispersion formula given by

$$\gamma = \alpha \cdot \sqrt{k \cdot g} - \beta \cdot k \cdot V_a$$

and

$$\gamma = \alpha \cdot \sqrt{\frac{k \cdot g}{1 + k \cdot L}} - \beta \cdot k \cdot V_a,$$

respectively, where γ is the growth rate, k is the wave number of the perturbation, g is the acceleration of the interface, V_a is the ablation velocity, α is a constant approximately equal to 0.9, β is a constant with an approximate value of 3, and L is the density scale length at the ablation surface. The importance of thermal conduction⁹ has been investigated and leads to a modification of the Takabe formula for the growth rate through changes in the values α and β that depend on the details of the thermal transport at the ablation surface.

Details of the dispersion formula for RT growth rates remain an active subject of research at this time. Previous measurements¹⁰ of the growth rate, conducted using x-ray radiography, have yielded values that are substantially lower than that calculated by either of the above formulae. The need for nonthermal electron transport has been proposed as the cause for these lower growth rates.

The results from a series of single-mode RT-instability growth experiments performed on the OMEGA laser system using planar targets are presented. Planar targets with imposed mass perturbations were accelerated using five to six 351-nm laser beams overlapped with a total overlapped intensity up to 2.5×10^{14} W/cm². Experiments were performed with both 3-ns ramp and 3-ns flat-topped temporal pulse shapes. The use of distributed phase plates (DPP’s)¹¹ and SSD resulted in a laser-irradiation nonuniformity of 4%–7% over a 600- μ m-diam region defined by the 90% intensity contour.

The temporal growth of the modulation in optical depth was measured using through-foil radiography and was detected with an x-ray framing camera. The temporal-growth evolution of the measured variation in the optimal depth for both 31- μ m and 60- μ m wavelength perturbations was found to be in good agreement with *ORCHID* simulations when the experimental details, including noise, were included. In addition, it has been found that for current experiments care must be taken in

relating the actual ablation-surface RT growth rate from the experimental observables used in these experiments.

Experimental Configuration

A schematic of the experimental layout (Fig. 71.5) shows the orientation of the three foils and diagnostics used in these experiments. The foils are supported by a 140- μm boron-coated carbon fiber. Five to six beams are incident onto the 20- μm -thick CH-foil drive target, which is mounted on a 50- μm -thick Mylar washer with a 1-mm hole in the center. A 2-mm \times 2-mm piece of 25- μm -thick uranium is mounted at the other end of the boron-coated carbon fiber 9 mm from the drive foil. Six to twelve beams were used to irradiate the uranium foil in order to generate the x rays needed to radiograph the accelerated foil. A third foil composed of 6- μm -thick aluminum was centered between the drive and backlighter foils to act as a bandpass filter for x rays between 1.0 and 1.5 keV. This prevents the very-low-energy x rays from the uranium target from preheating the accelerated foil.

The typical mass-modulated accelerated foil is composed of a 20- μm -thick CH foil that had perturbations imposed on the side irradiated by the laser. The 20- μm thickness was chosen because it represents about two attenuation depths for the 1.0- to 1.5-keV x rays used for radiography. Perturbation wavelengths of either 31 μm or 60 μm were imposed onto the foils with initial amplitudes of 0.45 μm and 0.5 μm , respectively. The face of the foil irradiated by the laser was overcoated with a 500- \AA to 1000- \AA layer of Al to prevent shinethrough.¹² (Foils used for acceleration measurements had no initial imposed mass perturbations.)

The primary diagnostic is an x-ray framing camera.¹³ The pinhole array is composed of eight 8- μm pinholes arranged in a checkerboard pattern to minimize interference from adjacent images. The framing camera used for the perturbation amplitude measurement has a magnification of 14.1 \pm 0.1 with

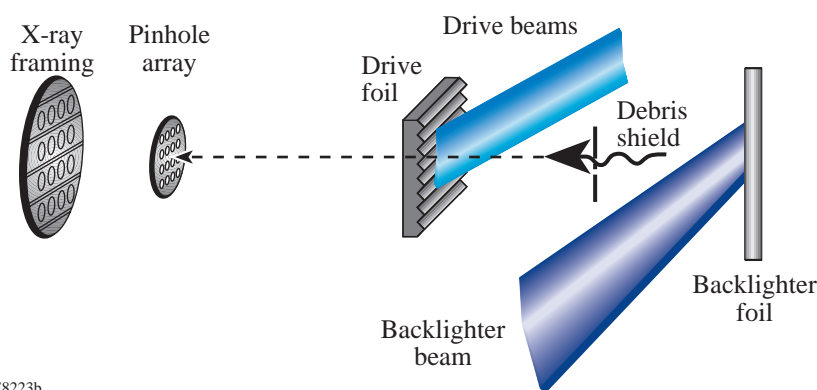
the pinhole array located 24.8 mm from the rear surface of the accelerated foil. A second x-ray framing camera measured the spatial and temporal emissions of the backlighter at a magnification of 6 with a standard 16-pinhole array. Each pinhole is 10 μm in diameter. Data from the backlighter framing camera are shown in Fig. 71.6. The images are timed so that the backlighter reaches full emission in the end of the second strip (i.e., between images 3 and 4). Each image is separated by 50 ps, and the timing of the backlighter emission is known to about 50 ps. The gating pulses for uniform strips of each of the two framing cameras are recorded by an oscilloscope, and the time of each image relative to the drive beams is known to about 100 ps. The temporal resolution of both x-ray framing cameras was 80 ps. The current noise levels on the framing camera allow the instrument to measure perturbations with amplitudes $\geq 0.4 \mu\text{m}$. As a result, the early-time amplitude of the accelerated foils was at the detection limit and, therefore, difficult to resolve.

Laser Irradiation

Typical planar-foil experiments use two independent drivers so that separate pulse shapes could be used for the drive and backlighter beams. The beams were overlapped onto their respective targets with a radial displacement accuracy of 35 μm from the center of each foil.

The backlighter pulse shape used was a 3-ns-wide flat-topped pulse. Each backlighter beam was focused to a 1.5-mm-diam spot at the 5% intensity contour and had an energy of ~ 400 J for a total of 3.2 to 4.8 kJ on the uranium backlighter.

The two pulse shapes used for the drive beams are shown in Fig. 71.7. The first was a 3-ns ramp pulse, and the second was a 3-ns flat-topped pulse. Each of the drive beams was focused to a ~ 900 - μm -diam spot size (at the 5% intensity contour) and incorporated DPP's with an on-target intensity distribution measured to be $I \propto \exp[-(r/r_0)^4]$. The resultant five- to six-



E8223b

Figure 71.5

Experimental schematic of the target and primary diagnostic. The target is constructed from three foils: a uranium backlighter, an aluminum debris shield, and a CH drive foil with an imposed perturbation. The primary diagnostic is an x-ray framing camera with a 14.1 magnification provided by 8- μm pinholes located 24.8 mm from the accelerated target.

beam overlapped spot had a region of constant intensity of $\sim 600\text{-}\mu\text{m}$ diameter. The drive beams were temporally smoothed by 2-D SSD with a total bandwidth of 0.135 THz at 351 nm with an angular dispersion of $33\ \mu\text{rad}/\text{\AA} \times 33\ \mu\text{rad}/\text{\AA}$ (IR bandwidths of $1.5\ \text{\AA} \times 0.7\ \text{\AA}$). The total drive intensity for six irradiation beams peaked at $2.5 \times 10^{14}\ \text{W}/\text{cm}^2$ for the ramp pulse and $2.0 \times 10^{14}\ \text{W}/\text{cm}^2$ for the flat-topped pulse.

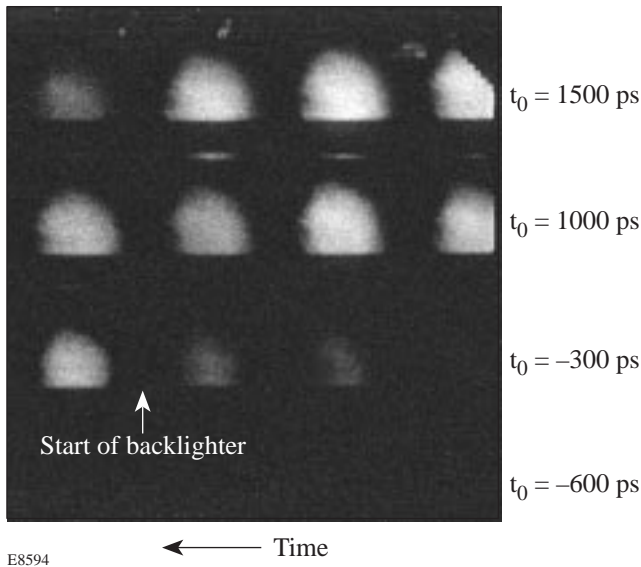


Figure 71.6

Framing camera image of backlighter x-ray emission. The four strips are timed from bottom to top and right to left. The values for t_0 reflect the trigger time of the strip relative to the start of the backlighter pulse.

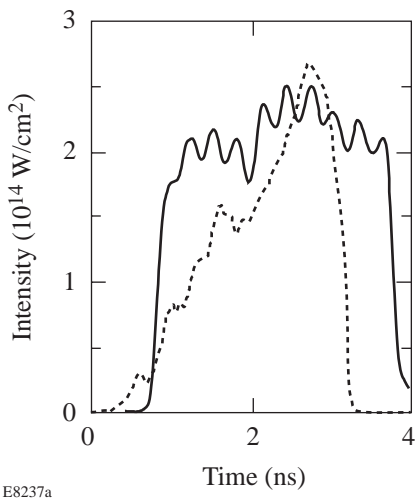


Figure 71.7

Laser illumination pulse shapes used to accelerate the CH target. The 3-ns ramp pulse (dashed curve) has a peak intensity of $2.5 \times 10^{14}\ \text{W}/\text{cm}^2$, and the 3-ns flat-topped pulse (solid curve) has an intensity of $2.0 \times 10^{14}\ \text{W}/\text{cm}^2$.

The uniformity of a single beam with a DPP and SSD at the maximum bandwidth for these experiments was measured by imaging the focal spot onto UV-sensitive film and analyzing the intensity distribution.¹⁴ The resultant nonuniformity for a single beam was measured as 12% integrated over $\sim 1\ \text{ns}$. The overlay of six of these beams onto the drive target is, therefore, expected to give an overall nonuniformity of 5%.

Acceleration Measurements

The measured acceleration for a $20\text{-}\mu\text{m}$ -thick CH foil driven with the 3-ns ramp pulse with a peak intensity of $2.5 \times 10^{14}\ \text{W}/\text{cm}^2$ is shown in Fig. 71.8. The data are shown as squares with error bars that reflect the accuracy of the position measurement. The round points are the position of the foil as simulated by the 1-D hydrodynamics code *LILAC*. The agreement between the measured foil position and the *LILAC* simulation is excellent and shows that the target drive is being accurately modeled.

While the data shown in Fig. 71.8 are consistent with a constant acceleration, the *LILAC* simulation shows that the acceleration (Fig. 71.9) for a 3-ns ramp pulse is not constant and changes by a factor of 2 during the experimental measurement. This points to the importance of complete simulations rather than the application of simplified models that generally assume constant acceleration.

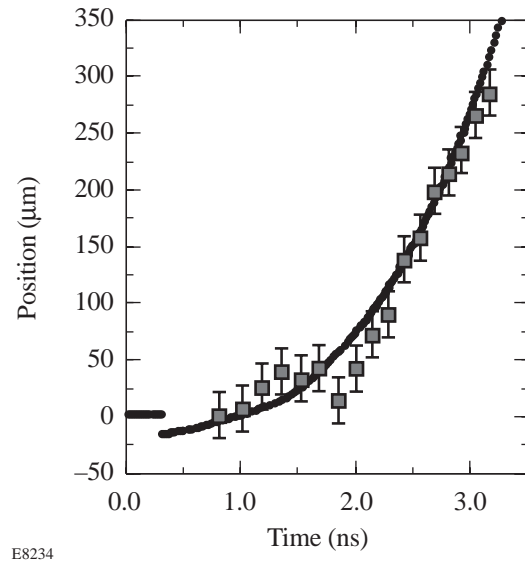
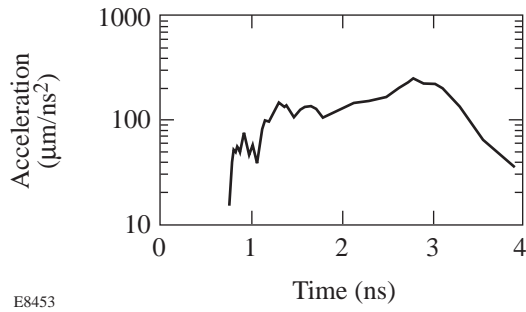


Figure 71.8

Comparison of the measured acceleration of a $20\text{-}\mu\text{m}$ -thick CH foil with a *LILAC* 1-D hydrodynamic simulation. The data are shown as squares with error bars and the calculation as circles.



E8453

Figure 71.9

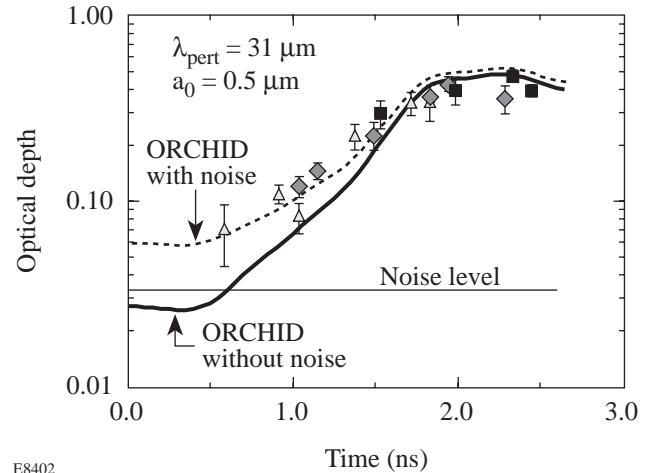
The calculated acceleration of a 20- μm -thick CH foil illuminated with a 3-ns ramp pulse with a peak intensity of $2.5 \times 10^{14} \text{ W/cm}^2$. The acceleration predicted by the simulation is not constant in time but continues to increase during the target illumination.

RT Growth Measurements

Face-on radiography was used to measure the RT growth of imposed perturbations. The modulation in the optical depth is calculated by analyzing a 250- $\mu\text{m} \times 250\text{-}\mu\text{m}$ region of the target for each temporal frame. The backlighter spatial distribution is taken out by fitting a two-dimensional, fourth-order polynomial to the natural log of the intensity. The fourth-order polynomial fit was used to model the x-ray intensity distribution from the backlighter for shots where no drive foil was present. It has also been verified by using higher-order polynomial fits (up to eighth order) and showing no significant improvement in the quality of the polynomial fit as determined from the value of χ^2 . This fit is then subtracted from the data, leaving the difference. This analysis tacitly assumes that the low-order polynomial adequately models the backlighter emission profile and does not affect the perturbation measurement. The analyzed region for the 31- μm -wavelength perturbation is chosen to be exactly eight wavelengths across the frame. A 2-D Fourier transform (FFT) then yields the optical depth at the perturbation wavelength. One dimension of the FFT is used to measure the imposed perturbation temporal evolution, and the orthogonal direction is used to determine the residual noise in the measurement.

Data from three target shots (plotted in Fig. 71.10) were taken with the 3-ns ramp pulse with a peak intensity of $2.5 \times 10^{14} \text{ W/cm}^2$. The measured data are shown as either diamonds, squares, or triangles. The error bars are calculated by analyzing separate regions in the x-ray images. The results are averaged and the standard deviation is plotted as error bars. The framing camera was triggered at three different times to study the evolution of the perturbation over 2.5 ns. The thick solid line in Fig. 71.10 is the optical depth calculated by the 2-D hydrody-

namics code *ORCHID*. It agrees with the measured optical depth late in time but not at early times. The thin solid line is an estimate of the noise in the experimental measurement as determined using the FFT technique outlined above. We thus estimate a minimum measurable optical depth of 0.033 as a noise source. The dashed line in Fig. 71.10 is the sum of the optical depth as calculated by *ORCHID*, and the noise and results are a good fit over the entire measurement time.



E8402

Figure 71.10

A comparison of the experimentally measured optical depth and the predictions of the *ORCHID* 2-D hydrodynamic simulations. Data are shown for three shots as diamonds, squares, and triangles; the calculated optical depth is shown as a solid line. Good agreement with the experimental data is achieved only when the experimental noise is added to the calculated optical depth.

The 3-ns square pulse data are shown in Figs. 71.11(a) and 71.11(b). The growth of an initial perturbation with a wavelength of 60 μm and an initial amplitude of 0.5 μm is shown in Fig. 71.11(a), and the growth of a 31- μm -wavelength perturbation with an initial amplitude of 0.45 μm is shown in Fig. 71.11(b). The data are plotted as points, and the *ORCHID* simulation is plotted as a solid line. In these data the experimental noise has been subtracted from the data before being plotted with the simulation output. Several shots are plotted together so that the temporal development of the modulation in the optical depth can be shown. The agreement between the variation in the optical depth measured with x-ray radiography and the *ORCHID* simulations for both cases is quite good over the temporal range of interest to determining the linear RT growth rate.

The *ORCHID* calculations are a complete end-to-end simulation of the experiment and include the backlighter spectrum,

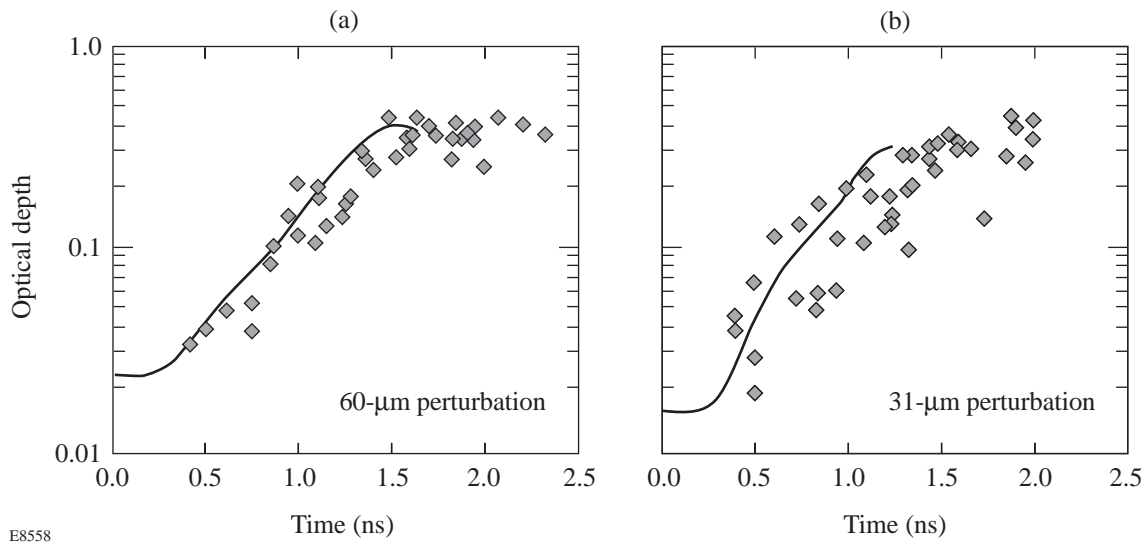


Figure 71.11

A comparison of the experimentally measured optical depth and the predictions of the *ORCHID* 2-D hydrodynamic simulations for both the 60- μm and 31- μm perturbations. Data are shown as diamonds; the calculated optical depth is shown as a solid line. Good agreement with the experimental data is achieved only when the experimental noise is subtracted from the measured optical depth. These are data for a 3-ns square drive pulse.

all filtering of the x-ray framing camera, and a correction for the camera resolution. The comparison of the optical depth calculated from the simulation with the experimental data shows the quality of the simulation. A simple comparison of the growth rate as calculated by a simulation and the growth rate taken from a set of experimental data is not sufficient. Detailed comparisons of the data from a series of planar-foil experiments and their associated numerical simulations show that associating the measured growth rate of the modulation in optical depth with that due to the ablative RT instability must be done with great care, if done at all. During this study, we have identified two important sources of departure in the growth rates inferred from variations in the optical depth as compared to determinations based on variations in the actual displacement at the ablation surface. The first source of discrepancy that must be accounted for is the “noise” in the measurement. Figure 71.10 indicates that using the measured variation in the optical depth yields a growth rate value of 1.6 ns^{-1} , while *ORCHID* (without noise) predicts approximately 2.1 ns^{-1} . Therefore, the accurate determination and treatment of experimental noise are important in determining growth rates. The second, and possibly more important, cause of problems in determining growth rates from the variations in the optical depth has been found to be the initial shock propagation through the foil. The *ORCHID* simulations of these experiments have shown that for the pulse shape-foil combinations used, the shock propagation through the foil has

a large influence on the temporal evolution of the modulation in optical depth early in time. The comparison within a given simulation of the growth rate from the evolution of the optical depth with the growth rate determined from the evolution of the ablation surface gives substantially different results. In all cases of large-initial-amplitude mass perturbations considered to date, we have found that the growth rate determined from the modulation in the optical depth is lower than that determined from the modulation in spatial position of the ablation surface (illustrated in Fig. 71.12). Analysis of the *ORCHID* results shows that the propagation of the initial shock through the foil results in a change in the $\rho\Delta x$ of the foil (predominantly through a change in the density) even before the ablation surface has accelerated (or moved) appreciably. A simple approximation to the temporal history of the variation in the $\rho\Delta x$ data has a functional form of $a = a_0 \cdot e^{\gamma t} + \text{constant}$, where the constant is due to the initial shock propagation.

To check this finding one can take the time derivative of $\rho\Delta x$. A closer analysis of the *ORCHID* simulation of a 31- μm -wavelength perturbation is plotted for the time of linear growth (0.8 ns to 1.1 ns) in Fig. 71.13. The data plotted as diamonds are the amplitude of the optical depth of the planar target as determined from the uranium backlighter. The amplitude of the $\rho\Delta x$ at the ablation interface is plotted as squares. The Δx amplitude from the variation in position at the ablation surface is plotted as x 's. The growth rate as determined by the $\rho\Delta x$ and

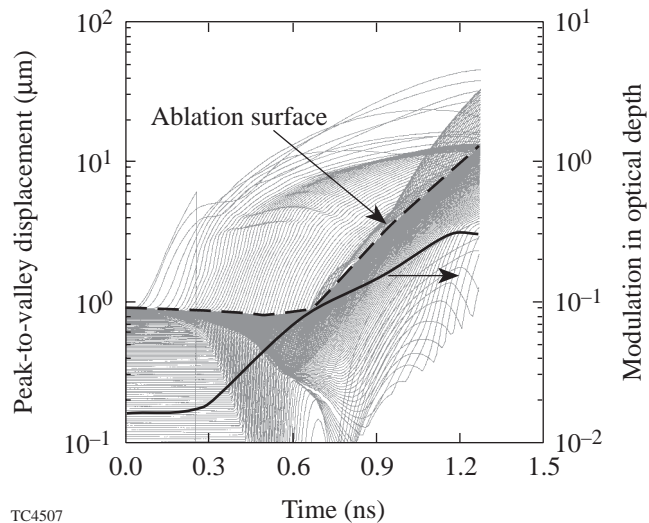


Figure 71.12

ORCHID simulation results for the growth of the perturbation at the ablation surface and the modulation in the optical depth are shown for one of the 31- μm , 0.45- μm initial amplitude experiments.

the optical depth are in agreement, but there is a significant difference in the growth rates as determined by radiography (optical depth) and the growth rate as determined from the ablation surface. The data plotted as triangles are the time derivative of the amplitude from the $\rho\Delta x$. When the time derivative of $\rho\Delta x$ is taken, the value of γ as determined by the variation in the displacement of the ablation surface is recovered. This behavior was also found for the 60- μm , 0.5- μm -initial-amplitude case and for both pulse shapes considered. (This second reason for growth-rate departures is reminiscent of the experimental noise effect encountered during the analysis of the framing camera data.)

Summary

The OMEGA laser facility has been used to study the growth of perturbations due to the RT instability at the ablation interface. The targets were accelerated with 351-nm illumination at $2.5 \times 10^{14} \text{ W/cm}^2$ for 3-ns ramp pulses and at $2.0 \times 10^{14} \text{ W/cm}^2$ for 3-ns flat-topped pulses. The comparison of target acceleration with 1-D hydrodynamics simulation is good and suggests that the laser drive is correctly modeled. The comparison for the growth of initial perturbations as measured by the change in optical depth agrees with 2-D *ORCHID* simulation when the measurement noise is included. It is important to compare the values of the measured optical depths and not simply the growth rates in order to understand the underlying physics and infer RT growth rates.

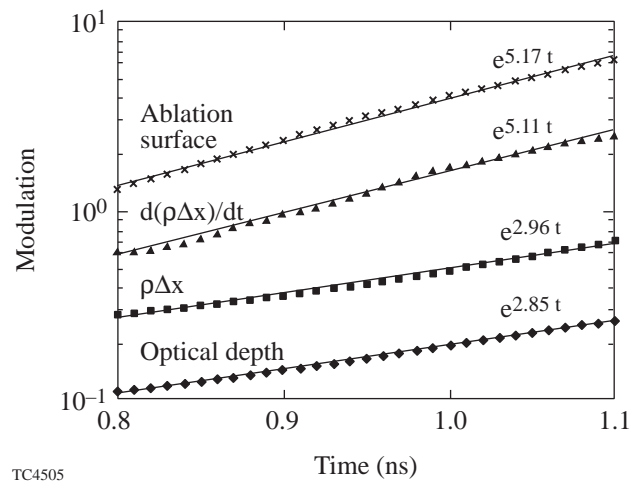


Figure 71.13

The growth of the perturbation as a function of time is plotted for three different simulation quantities: optical depth, $\rho\Delta x$, and ablation-surface amplitude. Both the optical depth and $\rho\Delta x$ show growth rates that are substantially different from the ablation-surface amplitude. The time derivative of $\rho\Delta x$ shows a growth rate that agrees with the ablation-surface amplitude.

The pulse shapes used in our experiments produce both accelerations and ablation velocities that evolve in time. This implies that care must be taken when determining growth rates from experimental data to ensure the validity of the underlying assumptions. The growth rates can be used to compare experimental data for targets with similar perturbations when the temporal region studied coincides with regions where the acceleration and ablation velocity are relatively constant.

It is important that the numerical simulations include as many details associated with the actual experiment and diagnostic configuration as possible. The comparisons between the hydrodynamic simulations and the experimental data should be made with the temporal evolution in optical depth modulation. If good agreement is found between the experimental data and the simulations, then the ablation-surface growth rate as determined from the simulation can be used with some level of confidence, as the RT growth rate for the initial perturbation used in the experiment.

It is evident from the effect of the noise on the comparison with calculations that future experiments will need to address this issue. Instruments and experimental techniques are needed that will reduce the level of noise so smaller initial perturbation amplitudes can be studied. Instruments are also needed that will allow shorter-wavelength perturbations to be studied.

ACKNOWLEDGMENT

This work was supported by the U.S. Department of Energy Office of Inertial Confinement Fusion under Cooperative Agreement No. DE-FC03-92SF19460, the University of Rochester, and the New York State Energy Research and Development Authority. The support of DOE does not constitute an endorsement by DOE of the views expressed in this article.

REFERENCES

1. J. Grun *et al.*, Phys. Rev. Lett. **58**, 2672 (1987).
2. M. Desselberger *et al.*, Phys. Rev. Lett. **65**, 2997 (1990).
3. S. G. Glendinning, S. V. Weber, P. Bell, L. B. DaSilva, S. N. Dixit, M. A. Henesian, D. R. Kania, J. D. Kilkenny, H. T. Powell, R. J. Wallace, P. J. Wegner, J. P. Knauer, and C. P. Verdon, Phys. Rev. Lett. **69**, 1201 (1992).
4. K. Shigemori *et al.*, Phys. Rev. Lett. **78**, 250 (1997).
5. S. G. Glendinning, S. N. Dixit, B. A. Hammel, D. H. Kalantar, M. H. Key, J. D. Kilkenny, J. P. Knauer, D. M. Pennington, B. A. Remington, R. J. Wallace, and S. V. Weber, Phys. Rev. Lett. **78**, 3318 (1997).
6. R. H. Lehmburg, A. J. Schmitt, and S. E. Bodner, J. Appl. Phys. **62**, 2680 (1987).
7. S. Skupsky, R. W. Short, T. Kessler, R. S. Craxton, S. Letzring, and J. M. Soures, J. Appl. Phys. **66**, 3456 (1989).
8. H. Takabe *et al.*, Phys. Fluids **28**, 3676 (1985).
9. R. Betti, V. N. Goncharov, R. L. McCrory, P. Sorotokin, and C. P. Verdon, Phys. Plasmas **3**, 2122 (1996).
10. M. Honda and K. Mima, to be published in Physical Review Letters.
11. Y. Lin, T. J. Kessler, and G. N. Lawrence, Opt. Lett. **20**, 764 (1995).
12. D. K. Bradley, T. Boehly, D. L. Brown, J. Delettrez, W. Seka, and D. Smith, in *Laser Interaction and Related Plasma Phenomena*, edited by H. Hora and G. Miley (Plenum Press, New York, 1991), Vol. 9, pp. 323–334.
13. O. L. Landen, P. M. Bell, J. A. Oertel, J. J. Satariano, and D. K. Bradley, in *Ultrahigh- and High-Speed Photography, Videography, and Photonics '93*, edited by P. W. Roehrenbeck (SPIE, Bellingham, WA, 1993), Vol. 2002, pp. 2–13.
14. T. R. Boehly, D. D. Meyerhofer, J. P. Knauer, D. K. Bradley, R. L. Keck, V. A. Smalyuk, W. Seka, and C. P. Verdon, "Laser-Imprinting Studies on the OMEGA Laser System," to be published in the *Proceedings of the Thirteenth International Conference on Laser Interactions and Related Plasma Phenomena (LIRPP)*, Monterey, CA, 13–18 April 1997.

Fabrication of Polyimide Shells for Use as ICF Targets

The current target-shell material for direct-drive experiments on OMEGA is a low-density hydrocarbon polymer fabricated using a low-pressure plasma polymerization process. This material meets the immediate requirements for an inertial confinement fusion (ICF) target shell: low density; smooth surfaces (outer and inner); spherical and concentric; and the capability of being fabricated with dopants at discrete radial positions in the shell wall. Future ICF experiments, especially those conducted at cryogenic temperatures, would benefit if the targets possessed additional properties: higher tensile strength; larger elastic moduli; greater room-temperature permeability; greater radiation resistance; higher thermal conductivity and lower electrical conductivity; and greater opacity at ~ 351 nm. These desirable properties will allow targets to be filled more rapidly with DT; be cooled faster to the DT triple point (19.8 K); survive higher temperature gradients in a cryostat; better resist the damaging effects of β -decay from tritium; and more readily accommodate augmented layering techniques such as RF-coupled joule heating. These properties will also allow decreasingly thin-walled shells to be used to contain the DT fuel; the goal is a 1-mm-diam target with a 1- μm -thick wall.

Polyimide is the only polymeric material with the potential for meeting these additional material requirements. Scientists at Lawrence Livermore National Laboratory were the first to suggest polyimide¹ targets for the National Ignition Facility (NIF). If targets could be fabricated with the same strength as commercial polyimide films, then cryogenic targets could be filled and transported at room temperature and frozen only immediately prior to the experiment. (The requirements for a NIF target are 2.2-mm outer diameter, 160- μm walls, and a DT room-temperature fill pressure of ~ 360 atm.) These simplifications would substantially reduce the complexity and cost of implementing indirect-drive cryogenic targets on the NIF.

Postulating and theoretically validating polyimide shells as a viable ICF target design were necessary first steps. Fabricating polyimide shells to experimentally quantify the material properties is the next phase. No polyimide shells have been

made until now because the available polyimide fabrication techniques could not be adapted to current target-fabrication technology. Two recent developments, one in the area of ICF target-fabrication methods and the other in the area of polyimide fabrication for microelectronics applications, have provided a method for fabricating polyimide targets: (1) the development of a decomposable polymer mandrel for making the present ICF targets and (2) the development of a technique for vapor-depositing polyimide films. This study employs the combination of these two techniques to produce polyimide shells and presents property data of the resultant material.

Background

1. Preparation of Solution-Cast Polyimide Films

Polyimides are usually produced in a two-step synthesis:² First, an aromatic diamine (e.g., ODA) is dissolved in a polar solvent such as dimethylformamide. An aromatic dianhydride (e.g., PMDA) is then added to the solution to form the soluble polyamic acid. The polyamic acid solution is spun-cast onto flat substrates and then thermally cured at 300°C to form the polyimide. The chemical structures are shown in Fig. 71.14. There is no straightforward way this technique can be adapted to make ICF targets using established microencapsulation methods. Furthermore, there are technical issues with this technique that may render the material unsuitable as a target shell material: polyamic acids are hydrolytically unstable; solvents may remain in the film; adverse interaction may occur between the solvent and the substrate (i.e., mandrel); and the viscosity of the polymer solution may make it difficult to control the thickness and uniformity of the shell wall.

2. Preparation of Vapor-Deposited Polyimide Films

The vapor-deposition-polymerization^{3,4} (VDP) technique of making polyimide film was developed to provide a solventless method of depositing conformal dielectric coatings. The process involved three steps: (1) dianhydride and diamine monomers were sublimed under high vacuum, (2) the vapor phase monomers reacted to form polyamic acid on the surface of the substrate, and (3) the polyamic acid was thermally cured at 300°C to form polyimide. The advantages of this pro-

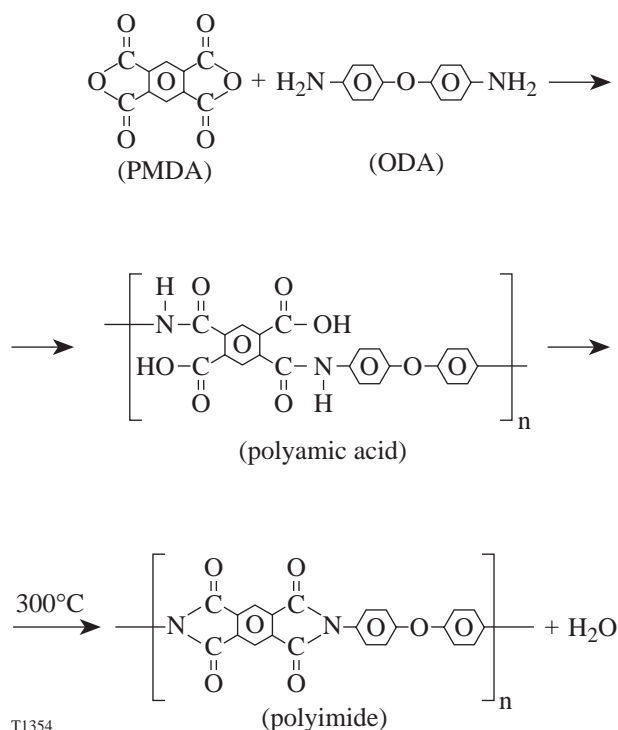


Figure 71.14
Formation of polyimide from pyromellitic dianhydride (PMDA) and oxydianiline (ODA) precursors.

cessing technique are the lack of detrimental solvent effects (i.e., vacuoles) and the uniformity of the film thickness. This technique was used in this study to make OMEGA-size ICF targets by depositing the film on spherical depolymerizable mandrels.

3. Fabrication of Targets Using Depolymerizable Mandrels

The depolymerizable mandrel technique was recently developed to fabricate plastic ICF targets.⁵ The mandrels were either solid beads or hollow shells made from poly(α -methylstyrene) (PAMS) that were overcoated with plasma polymer using the traditional low-pressure glow discharge polymerization process.⁶ Heating the overcoated mandrel to 300°C decomposes the mandrel into its individual monomer units that permeate through the shell wall. The importance of the PAMS formulation is that it undergoes complete depolymerization into gaseous monomers at a relatively low temperature (160°C–300°C), where the plasma polymer outer shell is thermally stable.

Currently, the PAMS mandrels are thin-walled ($\sim 20\text{-}\mu\text{m}$) shells (0.70- to 0.95-mm diam) fabricated by the micro-encapsulation method.⁷ (This method was initially developed to

make polystyrene shells for ICF experiments but is better suited for making mandrels.) A critical requirement of the mandrel, which has been demonstrated,⁸ is a smooth, spherical surface.

4. Comparison of Target-Material Relevant Properties

Table 71.I compares the relevant properties of the current target-shell material against the properties of polyimides fabricated using both solution-cast and vapor-phase-deposition techniques.

There are many formulations of solution-cast polyimide films, and the material properties are well defined. The values listed here are the optimal values reported for two types of commercially available polyimide: Upilex-S and Kapton. The values listed for vapor-deposited polyimide films are from the literature. However, these values possess greater uncertainties and are likely to be more process dependent. The strength and modulus values listed for ICF shells are the best estimates derived from a limited set of burst and buckle tests of 1-mm-diam shells.

Fabrication and Characterization

1. Materials

Pyromellitic dianhydride (PMDA) (1,2,4,5-benzenetetracarboxylic dianhydride; 97% purity) and 4,4'-oxydianiline (ODA) (99+% purity; zone refined) were received from Aldrich Chemical and used without further purification. Poly(α -methylstyrene) mandrels were received from General Atomics (850- to 950- μm inner diam; $\sim 20\text{-}\mu\text{m}$ wall thickness; MW 400,000) or fabricated in-house (700- to 950- μm inner diam; $\sim 10\text{-}\mu\text{m}$ wall thickness; MW 97,500).

2. Deposition Equipment

The deposition system consists of a vacuum chamber, mechanical pump, and two identical evaporation sources, one each for PMDA and ODA (Fig. 71.15). The chamber was a stainless steel cube with an adapting tee (6-liter internal volume) and three glass viewports. The system was pumped with a mechanical pump (Alcatel model 2010) through two liquid nitrogen foreline traps and achieved a base pressure of 1 mTorr. Each evaporation source was a copper cylinder containing a 0.3-cm-outer-diam \times 5-cm cartridge heater (Watlow Firerod; 50 W max) and a K-type thermocouple. The temperature was maintained within $\pm 1.0^\circ\text{C}$ of the set point using a proportional-integral-derivative controller (Omega CN9000).

Each evaporation source contained ~ 50 mg of monomer, which was sufficient material for an 8-h process cycle. The

Table 71.I: A comparison of available relevant material properties of existing ICF shells and two types of polyimide.

	Current ICF Plasma Polymer Shell	Vapor-Deposited Polyimide Film	Solution-Cast Polyimide Film
Ultimate tensile strength (MPa) at 300 K at cryogenic temperatures	75±15 ^a 160±12 at 40 K ^b	120–170 ^{c,d} –	420 ^e 500 at 77 K ^e
Elastic modulus (GPa) at 300 K at cryogenic temperatures	3.1 ^a 9.7 at 15 K [*]	2.3–4.0 ^{c,d} –	9.3 ^e 12 at 77 K ^e
Density (g/cm ³)	1.039	1.39 ^d	1.42 ^f
Coefficient of thermal conductivity (W/m•K)	0.04 at 20 K ^{**}	– –	0.82 at 293 K ^g 0.08 at 20 K ^g
Dielectric constant	2.5 (at 1 MHz) ^{**}	2.91 (at 1 MHz) ^c	3.4 (at 1 GHz) ^f
Radiation resistance (electron) (dose required to reduce the maximum elongation by 50%)	–	–	6 × 10 ⁷ Gy ^f (1 × 10 ¹⁴ Ci•s)
Permeability at 300 K (mol•m/m ² •Pa•s)	6.5 × 10 ⁻¹⁵ (for D ₂) ^a	1 × 10 ⁻¹⁹ (for O ₂) [*]	2.9 × 10 ⁻¹⁵ (for H ₂) ^h

* data for a polyamide film.

** data for a polystyrene film.

^a R. Gram, UR/LLE (private communication).

^b N. Alexander, General Atomics (private communication).

^c Ref. 3.

^d M. Iijima, Y. Takahashi, High Perform. Polym. **5**, 229 (1993).

^e H. Yamaoka, K. Miyata, O. Yano, Cryogenics **35**, 787 (1995).

^f DuPont Technical Bulletin. Product information for Kapton Type-H film.

^g H. Yokoyama, Cryogenics **35**, 799 (1995).

^h Ref. 15.

optimal processing conditions that yielded a uniform distribution of each monomer in near-stoichiometric proportions are listed in Table 71.II. The partial vapor pressure of PMDA and ODA at these conditions was 0.35 and 0.15 mbar⁹ (0.26 and 0.11 Torr), respectively.

The preferred experimental configuration for making particulate-free coatings is to suspend the substrate upside down in the vacuum chamber with the evaporation sources directly beneath the substrate. This configuration cannot be used with the existing bounce-coating method for coating shells, so the evaporation sources were built to direct the monomer flow downward onto the substrate. The substrates were either flat witness plates (NaCl and silicon wafers) mounted on a thermally isolated support or spherical mandrels placed in a bounce pan. The bounce pan consisted of a 2-cm curved dish with a piezoelectric element attached to the base. A 5-V, 3-kHz signal applied to the piezo-material maintained the shells in a gentle, random motion during the deposition process. Unlike previous techniques used to coat shells (e.g., plasma parylene

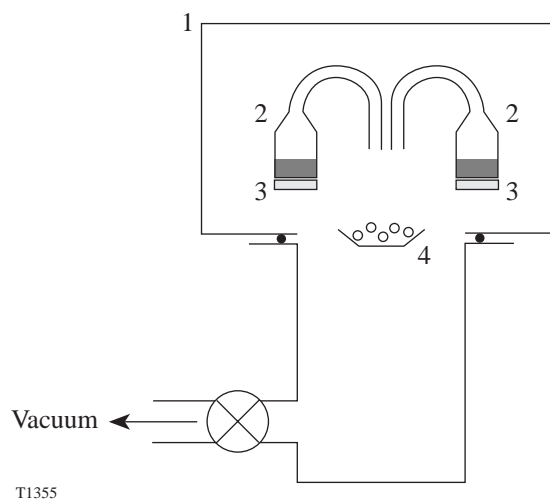


Figure 71.15
Schematic of the deposition chamber: (1) vacuum chamber, (2) deposition source, (3) heater, and (4) bounce pan containing shells.

Table 71.II: Processing conditions used to deposit polyamic acid films from PMDA-ODA monomers.

PMDA temperature	160°C
ODA temperature	140°C
System pressure	1 to 30×10^{-3} Torr
Separation between evaporation sources and substrate	5 cm
Diameter of substrate that received a uniform coating	3 cm
Coating rate on shells	0.8–1.0 $\mu\text{m/h}$
Coating rate on flat substrates	$\sim 3 \mu\text{m/h}$

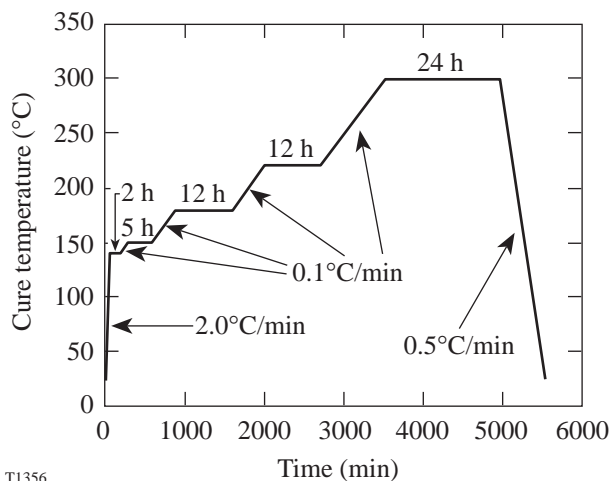
and plasma polymer), the VDP-polyimide technique does not require a plasma to initiate or accelerate the polymerization process. However, the plasma had an essential serendipitous benefit of preventing shells from sticking together by overcoming the static charge that developed as targets rubbed against each other. (Shells bouncing in the sheath of the RF plasma developed a similar potential that swamped the friction-induced static charge and caused the shells to mutually repel.)

The experimental equipment was modified to add a mechanism to overcome the induced static charge. First, a copper electrode was added inside the vacuum chamber to ignite an argon plasma (glow discharge). The pressure was increased from 1 to ~ 30 mTorr (using argon), and the plasma was maintained for the minimum period necessary to dislodge the shells from the pan (~ 15 s every 15 min). An alternative method of dissipating the static charge used a thermionic electron source directed at the pan. A tungsten filament was positioned ~ 1 cm from the pan, and a constant current (6 mA) was maintained through the filament. The resulting flood of electrons negatively biased the shells and prevented them from sticking together. This process was independent of pressure, which permitted the base pressure of 1 mTorr to be maintained during deposition. Both techniques successfully prevented shells from sticking to themselves or the pan during the >6 -h processes, and shells made by both techniques were evaluated in subsequent tests.

3. Heating Cycle

A programmable vacuum furnace (Ney Centurion VPM) was used to thermally convert (i.e., imidize) the polyamic acid shells to polyimide, and to decompose the inner PAMS mandrel. The furnace's cylindrical heated zone was 10-cm diam \times 6.3-cm high, and the progress of the depolymerization process was monitored through a glass viewport. The heating cycle was performed in a static air environment. The heating rate was controlled with an accuracy of $\pm 0.1^\circ\text{C/min}$.

Each shell was placed in a separate glass tube in the furnace to protect it from fratricidal impact should any shell burst during curing. The optimum heating cycle (Fig. 71.16) required the temperature to be raised from 25°C to 140°C at 2.0°C/min , with a 2-h dwell, then raised to 150°C (5-h dwell), 180°C (12-h dwell), 220°C (12-h dwell), and 300°C (24-h dwell), at a rate of 0.1°C/min . After the final heating stage the furnace cooled to room temperature at $\sim 0.5^\circ\text{C/min}$.



T1356

Figure 71.16

Curing cycle used to imidize the polyamic acid and depolymerize the PAMS mandrel.

4. Chemical Analysis—FTIR Measurements

The monomer precursors were co-deposited onto NaCl substrates for Fourier transform infrared (FTIR) characterization. FTIR spectra were taken on the as-deposited, partially cured, and fully cured films, as shown in Fig. 71.17. The spectrum of the as-deposited film showed absorption peaks at ~ 1850 and 1780 cm^{-1} due to the carboxylic acid anhydride and peaks at ~ 1650 and 1550 cm^{-1} due to amide couplings $\{[\text{C}=\text{O}(\text{CONH})]$ and $(\text{C}-\text{NH})$, respectively}. These spectra indicated that the as-deposited film consisted of nonreacted

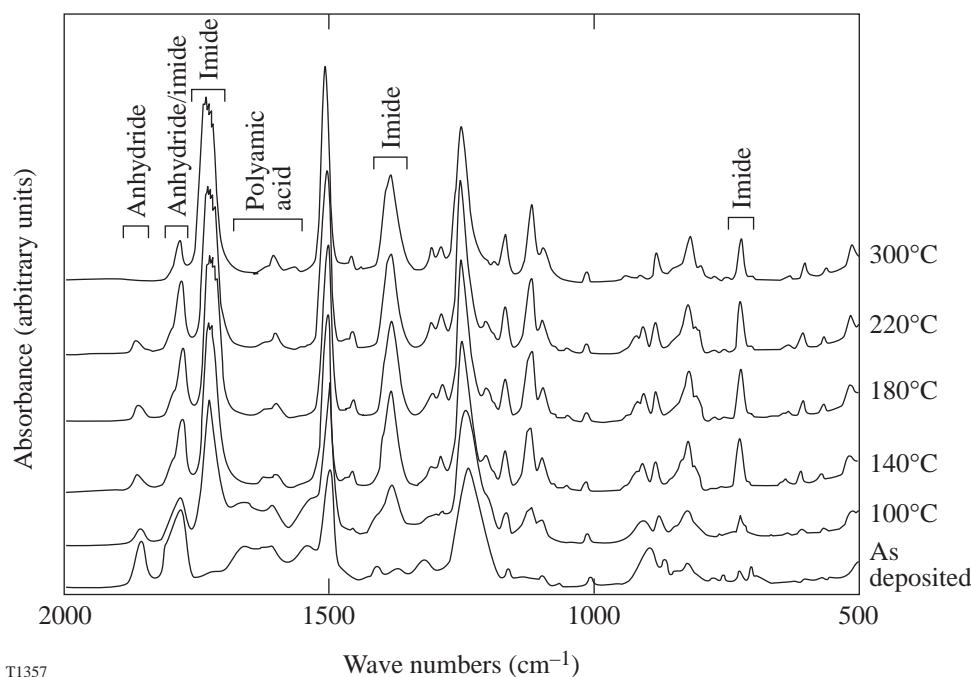


Figure 71.17
FTIR spectra of the as-deposited, partially cured, and fully cured PMDA-ODA/polyamic acid/polyimide film. The characteristic polyimide peaks appear as the material cures.

T1357

monomers and polyamic acid. After curing at 300°C for 60 min, the imide absorption peaks were dominant: 1780 cm⁻¹ (C=O asym. stretch), 1720 cm⁻¹ (C=O sym. stretch), 1380 cm⁻¹ (C-N stretch), and 725 cm⁻¹ (C=O bend), and the amide coupling and carboxylic acid anhydride absorption peaks had disappeared. These spectra agree with similar results published in the literature.^{3,10} [The formal name for this polymer is poly(N,N'-bis(phenoxyphenyl) pyromellitimide) and is commonly known as PMDA-ODA polyimide. A solution-cast version is sold under the trade name Kapton®.]

5. Shell Dimensions

The outside diameter of the shells was measured to an accuracy of ±1 μm using a Nikon Optiphot optical microscope equipped with a HMOS Micro-Measure digital scaler. The wall thickness was determined from SEM micrographs of cross sections through the shell with an accuracy of ±0.3 μm. (The targets were too opaque to use interferometry to measure the wall thickness.)

The sphericity was determined by measuring the outer diameter along a single axis and then repeating the process for additional axes. The sphericity s of a shell was defined as $s = [1 - (D_{\max} - D_{\text{avg}})/D_{\text{avg}}] \times 100\%$, where D_{\max} is the maximum diameter and D_{avg} is the average diameter from 12 measurements. The sphericity of the polyimide shells was >99%, a value consistent with plasma polymer shells fabricated by the decomposable mandrel technique.

Imidizing the polyamic acid and depolymerizing the mandrel caused the resulting polyimide shell to be smaller and thinner than the original polyamic acid shell. The polyimide shell's outer diameter was 1% to 2% smaller than the original diameter. The polyimide wall was 20% to 30% thinner than the wall of the polyamic acid shell. The range of dimensions of all the polyimide shells is listed in Table 71.III.

Table 71.III: Typical dimensions of polyimide shells successfully fabricated in this study.

Inner diameter	700 to 950 μm
Wall thickness	4 to 13 μm
Sphericity	> 99%
Shrinkage: wall outer diameter	20%–30% 1%–2%
Density	1.21 to 1.40 g/cm ³

6. Elemental Composition—RBS Measurements

The elemental composition of the fully imidized polyimide film was measured using Rutherford backscattering (RBS) analysis. The RBS technique has the advantage of providing absolute quantitative data without calibrating against NIST-traceable standards. Also, the technique can be used to study a single shell (probe size ~5-μm-diam circle) and can provide depth-resolved compositional data.

The data were acquired using the Dynamitron at the Nuclear Laboratory at the State University of New York at Albany. The recoil data were fitted using the RUMP program. A 2-MeV He beam was used to acquire the backscattered signal. The total charge from the beam was kept below 6 μC to prevent the beam from heating the film and changing the elemental composition.

The measured elemental composition of one of the polyimide films was 50 at.% carbon; 37 at.% hydrogen; 9 at.% oxygen; and 4 at.% nitrogen. The uncertainty was $\sim 20\%$. The theoretical composition of a PMDA-ODA polyimide is 56 at.% carbon; 26 at.% hydrogen; 13 at.% oxygen; and 5 at.% nitrogen.

7. Burst and Buckle Pressure Measurements

The equipment consisted of a pressure cell with opposing windows, a microscope, a CCD camera, and a pressure transducer (Omega PX621) with an accuracy of ± 1 psi. The shells were viewed through a microscope with transmitted light. The shell's image, the gas pressure in the cell, and the lapsed time were all recorded on videotape.

To burst (or buckle) a shell, the pressure in the chamber was lowered (or raised) at a faster rate than the rate the internal shell pressure changed due to permeation through the shell wall. Typical pressure-rate changes ranged from 0.01 atm/s to 3.5 atm/s for buckle tests and up to 50 atm/s for burst tests. After the shell failed, the video tape was reviewed frame-by-frame to determine the exact rupture pressure. If the permeation time constant of the shell was known, the pressure difference across the shell wall at the point of failure could be accurately calculated, and the strength measurement was corrected for this change.

8. Permeability and Time Constant Measurements

a. For shells. The permeability of a shell was measured¹¹ by permeating gas into the shell and then transferring it into a (pre-baked) chamber of known volume (2.4 cm³). The pressure rise in the chamber was monitored as a function of time, and the data were fitted with the expected exponential function. A correction term was added to this function to account for outgassing from the chamber walls ($\sim 4 \times 10^{-11}$ Torr $\cdot\ell/\text{cm}^2\cdot\text{s}$). The equation gives the shell's permeation time constant (for the specific gas) and the total quantity of gas in the shell at the time the pressure measurement began. The technique allowed permeation time constants as short as 1 min and as long as 50 h to be measured with an accuracy greater than 95%.

The permeation time constant τ was determined from the plot of pressure rise versus time. The material permeability coefficient K_p was determined using the permeation time constant of a thin spherical container, $\tau^{-1} = (K_p A R_g T) / wV$, where A is the shell's mean surface area, R_g is the ideal gas constant, T is the absolute temperature, w is the shell wall thickness, and V is the shell volume. For a thin-walled spherical shell this simplifies to $K_p = w \langle r \rangle / 3\tau R_g T$, where $\langle r \rangle$ is the average shell radius.

b. For flat films. The equipment and test method were based upon the ASTM procedure, which estimates the steady-state rate of transmission of a gas through plastics in the form of a film, sheeting, laminates, and plastic-coated papers or fabrics.¹² A flat, freestanding polyimide film was mounted in a gas transmission cell to form a sealed semibarrier between two chambers. One chamber contained the test gas at a specific high pressure, and the other chamber, initially evacuated, received the permeating gas. The rate of gas transmission through the polyimide film was determined from the measured pressure rise in the downstream chamber. The permeability of 1-cm-diam, 14.7- μm -thick polyimide films was then measured using deuterium and nitrogen. Equipment accuracy was tested by comparing the measured permeability of commercial polyimide films (Kapton and Upilex-R) against the reported values; the agreement was within 50%.

9. Roughness Measurements

Surfaces of the shells and flat films along with cross sections of the shell walls were inspected using a scanning electron microscope (Cambridge Instruments, model S200). The micrographs provided a qualitative measurement of the surfaces' morphology and roughness. Quantitative measurements were obtained using atomic force microscopy (AFM): flat polyimide films on silicon witness plates were analyzed using a Nanoscope III instrument (Digital Instruments); and shells were analyzed using an AFM modified to measure 1-mm-diam shells. The latter technique, performed by General Atomics, measured the roughness along great arcs of a circle around a sphere. Generally, the flat films were very smooth and the spheres were rough (data discussed in detail later).

10. Mechanical Behavior—Stress Measurements

The residual stress that develops in the polymer during the imidizing cycle must be known so that the heating cycle can be optimized to minimize the induced stress. Shells that crack during curing behave this way because of the rate and magnitude at which the stress develops in the shell wall. In this

process, the change in the residual stress was expected to be significant; imidization involves an appreciable mass loss and a substantial change in the structure and morphology of the polymer as the polyamic acid is converted into an increasingly high-molecular-weight polyimide.

Thin polyamic acid films were deposited on high-aspect-ratio silicon (100) substrates (1 cm × 0.1 cm × 0.25 mm thick). The curvature of the substrate was measured prior to, and following, deposition using a profilometer (Rank Taylor Hobson Talysurf). The measured change in the radius of curvature (ΔR) due to the polymer film yielded the total stress (σ_{total}) in the film.¹³

$$\sigma_{\text{total}} = \left[E_s / 6(1 - \nu_s) \right] \left[t_{\text{substrate}}^2 / t_{\text{film}} \right] \left[\Delta R^{-1} \right],$$

where E_s is the elastic modulus of the silicon substrate, ν_s is the Poisson ratio, and t is the thickness of the film/substrate. The total stress was the sum of the intrinsic stress and the induced thermal stress (due to the thermal coefficient mismatch between the silicon substrate and the deposited film) that arises because the film was imidized at an elevated temperature and the stress was measured at room temperature. The thermal stress (σ_{thermal}) is given by

$$\sigma_{\text{thermal}} = \left[E_f / (1 - \nu_f) \right] \left[\alpha_{\text{silicon}} - \alpha_{\text{polyimide}} \right] \Delta T,$$

where E_f and ν_f are the elastic modulus and Poisson ratio of the polyimide film, respectively, α is the coefficient of thermal expansion for the silicon/polyimide, and ΔT is the difference between the cure and measurement temperatures. Subtracting the thermal stress determined the intrinsic component of the residual stress. These data are discussed later.

Discussion

1. Optimizing the Processing Conditions

The first task was to define the operating parameters required to deposit thin films of polyamic acid with a stoichiometric balance of PMDA and ODA monomers. Optical macrographs and FTIR spectra of the films deposited on flat NaCl witness substrates showed the importance of (1) positioning the substrate relative to the PMDA and ODA evaporation sources and (2) the temperature of the evaporation sources. The film deposited at the center of the substrate experienced an equivalent flux of each monomer and was opaque. FTIR spectra of this region identified polyamic acid as the primary

component. The perimeter of the substrate possessed a film that was thinner and more transparent than the center and contained excess PMDA or ODA, depending upon the substrate's position relative to the evaporation sources. Rotating the substrate during deposition improved the uniformity of the film's thickness and composition. These experiments defined the optimal distance between the evaporation sources and the substrate, the required temperature of the evaporation sources, the maximum diameter of the substrate that was uniformly coated with polyamic acid, and the resultant deposition rate (see Table 71.II). Examples of the FTIR data for this analysis are shown in Fig. 71.18 and compared to spectra reported in the literature.³ Here, the relation between the film's composition and the evaporation source temperature was demonstrated. When the source temperatures for PMDA and ODA were 160°C and 120°C, respectively, excess PMDA was present in the film, and the characteristic dianhydride peaks at 1780, 925, 905, and 720 cm⁻¹ were proportionally greater than the peaks attributed to ODA. Raising the ODA temperature to

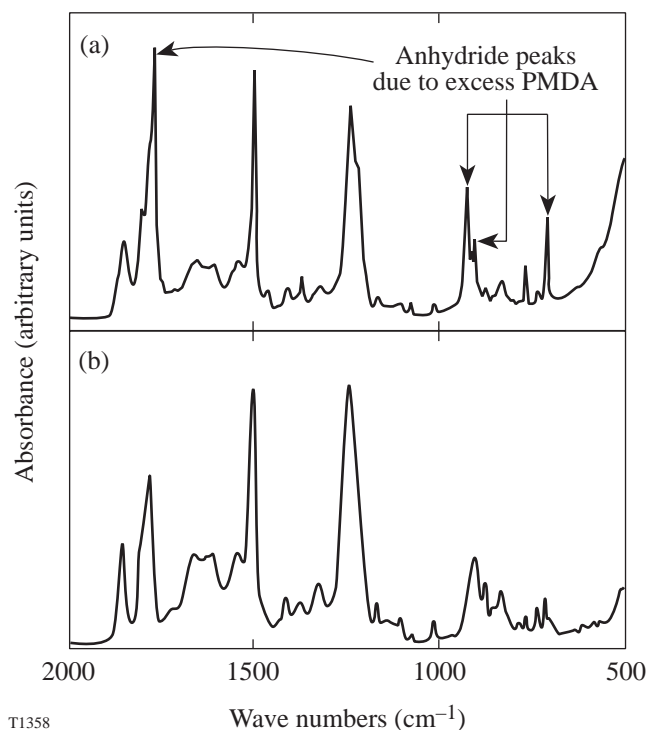


Figure 71.18 FTIR spectra of the as-deposited films made with varying ODA deposition temperatures: (a) $T_{\text{ODA}} = 122^\circ\text{C}$, $T_{\text{PMDA}} = 160^\circ\text{C}$; (b) $T_{\text{ODA}} = 140^\circ\text{C}$, $T_{\text{PMDA}} = 160^\circ\text{C}$. Spectrum (b) is identical to the polyamic acid spectrum as reported in the literature. Spectrum (a) shows anhydride peaks due to excess PMDA.

130°C provided an observed improvement, but the best results (based upon comparisons with the literature) were obtained with the source temperatures of 160°C and 140°C for PMDA and ODA, respectively. The spectrum shown in Fig. 71.18(b) is identical to that reported in the literature as a 1:1 molar ratio polyamic acid film.³

The next phase was to define the thermal cycle required to convert the polyamic acid into the polyimide. Typically, VDP polyamic acid films were heated to 175°C for 30 min, then to 300°C for 30 min. The cycle used for the current films included a slower ramp and was interrupted at 100, 140, 180, and 220°C to monitor the changing chemical and mechanical composition of the film. FTIR spectra of the polyamic-acid-coated NaCl substrate were acquired, and the change in curvature of the coated Si substrate was measured.

Conversion of polyamic acid into polyimide was evident at the first inspection at 100°C. Two characteristic absorption peaks were present: the C-N stretch frequency at 1380 cm⁻¹ and the C=O asymmetric stretch at 1720 cm⁻¹ (Fig. 71.17). This observation is consistent with reports that state VDP polyamic acid films begin imidization at lower temperatures than do solution-cast films.¹⁴ As the heating cycle progressed, the imide peaks became more prominent and the polyamic acid absorption peaks (at 1650 to 1550 cm⁻¹) diminished. Anhydride peaks (1850 cm⁻¹) were still visible after heating to 220°C but disappeared after the final curing stage at 300°C. The changes in the stress that accompanied these chemical changes are described later.

The heating cycle used above was inadequate for imidizing polyamic-acid-coated PAMS shells; the simultaneous depolymerization of the PAMS mandrel overpressurized the shells, causing them to burst. A considerably slower heating ramp (see Fig. 71.16), with longer dwells at critical temperatures,

was required to balance the rate at which PAMS decomposed with the rate at which α -methylstyrene permeated through the polyamic acid/polyimide/PAMS shell wall. This heating cycle was determined empirically since the mechanical and permeability properties of the wall could not be predicted. Several events complicated the process because they occurred simultaneously: excess monomer was subliming; PAMS was depolymerizing; the polyamic acid was reacting to form the polyimide; the softening PAMS was slumping, and the weight of the viscous material was adding a nonuniform strain to the shell wall; and the shell wall was resisting an increasing burst-pressure as the α -methylstyrene partial pressure increased with increasing temperature. Identifying a successful heating cycle is the most important component of making thin-walled, high-aspect-ratio polyimide shells. Currently the thinnest shells successfully fabricated have 4- μ m walls and 700- to 950- μ m inner diameters.

2. Morphology of the Polyimide Material

Polyimide films (3- to 15- μ m thickness) deposited on flat substrates were evaluated using optical, electron, and atomic-force microscopy and were observed to be very smooth. The rms roughness was 0.81 nm with most of the power attributed to features with a wavelength between 1 and 0.1 μ m (Fig. 71.19). These results indicate that the deposition and imidizing process provided a material with a smooth surface that is acceptable for use in ICF experiments.

In contrast to the flat film, the shells possess substantial roughness. The rms roughness of a polyamic-acid shell deposited using plasma assistance was ~800 nm. This quantified roughness was consistent with SEM micrographs that showed a nodular surface with a high density of nodes 1 to 5 μ m in diameter [Fig. 71.20(a)]. This roughness may be attributed to either the special processing conditions required to coat shells (the plasma- or thermionic-assisted technique) or a prob-

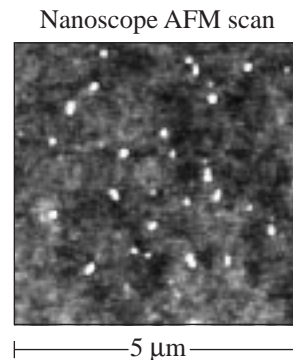
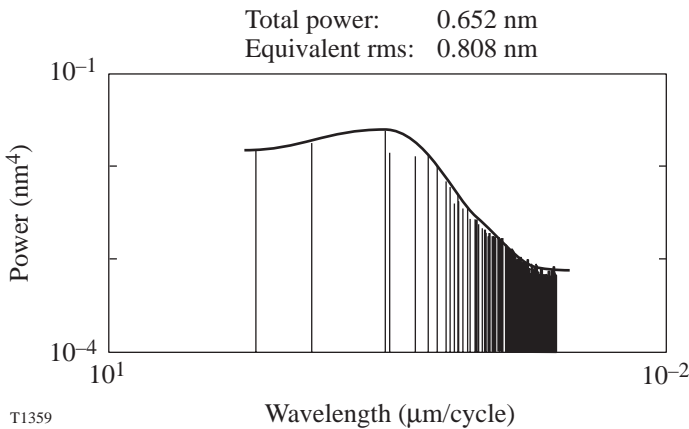


Figure 71.19
Power spectrum of a flat polyimide film. The rms roughness is 0.81 nm.

lem specific to forming a rigid polyimide structure in a spherical geometry.

One reason that shells possess a greater roughness than flat films is the high background pressure (20 to 30 mTorr) required by the plasma-assisted technique. A high pressure causes reacting monomers to experience thermalizing gas phase collisions before they reach the shell's surface. This reduces the mobility of the adsorbed atoms (adatoms), which prevents the nascent layer from fully relaxing before the subsequent atomic layer arrives at the surface and freezes the current distribution of adatoms in place. This loss of surface diffusivity generates nodular features with sizes inversely proportional to the adatom diffusion distance. These effects on the magnitude and frequency of the nodes are compounded by statistical fluctuations in the vapor flux, and the amplitude of the roughness grows with increasing film thickness, due to self-shadowing effects.

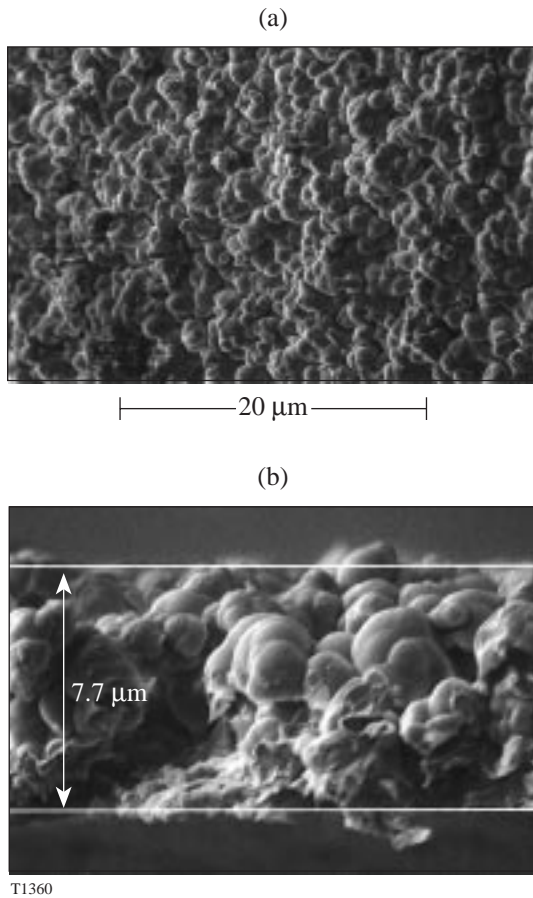


Figure 71.20
Outer surface (a) and cross section through the wall (b) of a polyimide shell made in the presence of a plasma. The nodular structure is seen through the shell wall.

Polyimide shells made by the plasma-assisted method were rougher and more nodular than the shells made by the thermionic emission method. Examination of the cross sections of fractured shells deposited with plasma assistance showed that the nodular morphology and internodular porosity extend through the wall to the inner surface (Fig. 71.20), while shells deposited with thermionic assistance possessed denser walls with no visible porosity and a smooth inner surface (Fig. 71.21). Despite the improved smoothness achieved at lower processing pressures, the smoothness of the shells deposited using thermionic assistance did not qualitatively approach the smooth-

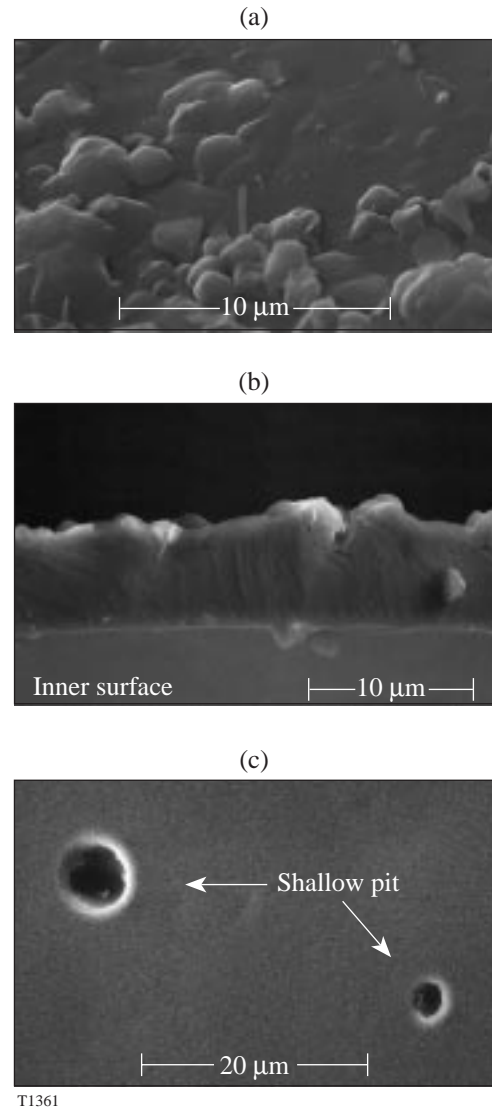


Figure 71.21
Outer surface (a), cross section through the wall (b), and inner surface (c) of a polyimide shell made in the presence of thermionic emission. The wall appears to be fully dense. The indentations on the inner surface are imprints from imperfections and debris on the PAMS mandrel.

ness of the flat films. (A quantitative comparison remains to be performed.) These observations suggest that the increased pressure contributes to, but is not solely responsible for, the shell's roughness. The only remaining differences between the processing conditions used to make flat films and spheres are the bouncing motion, spherical geometry, and substrate material of the shells, from which we conclude that one or all of these effects contribute to the observed roughness.

The inner surface of the shells deposited by thermionic emission appeared similar to the surface of plasma polymer shells currently made using the PAMS mandrel. Shallow domes (~1- to 5- μm diameter and <10 μm deep) were sparsely distributed over the inner surface [Fig. 71.21(c)]. These features are replicates of the underlying mandrel imprinted into the overcoated polyimide as a consequence of the highly conformal mapping capability of the deposition process.

3. Material Property: Permeability

The rate at which hydrogen isotopes permeate through the polyimide material is a major factor that will determine the viability of vapor-deposited polyimide films as target shell material. A high room-temperature permeation rate will allow targets to be rapidly filled to the designated pressure (maximum is 1500 atm) for cryogenic ICF experiments. A slow room-temperature permeation rate will require that the targets be filled at elevated temperatures (200°C max); otherwise the material cannot be used. It is necessary that the material be impermeable below 26 K and desirable, although unlikely, that the material be permeable above ~50 K. This latter capability will prevent a pressure differential from developing across the shell wall during the cooling cycle (due to temperature gradients in the permeation vessel).

The permeation time constant τ of deuterium for a PAMS shell at 298 K was $\tau = 1.2$ to 3.9 min (τ depends on the shell dimensions). The permeation time constant for the PAMS shells with a polyamic acid coating was $\tau = 1.12$ h. (The polyimide shells discussed here were made using the thermionic emission technique.) After the polyamic acid was imidized and the mandrel removed, the permeation time constant could not be measured. There was insufficient gas in the target to obtain a pressure reading on the apparatus; the time constant was either less than ~45 s or greater than ~50 h. The results were similar when nitrogen—a less permeable gas—was used (a time constant could not be measured with the current equipment). Unfortunately, literature values could not clarify whether the time constant was short or long: permeation rates obtained from the literature for solution-cast polyimide films

with a similar composition indicate a short time constant for hydrogen,¹⁵ ~2.4 min, while the limited data available for vapor-deposited films suggest a very long time constant.¹⁶

The permeability of the shell material and underlying mandrel was measured after curing to increasingly higher temperatures of the imidizing cycle to determine at which point in the cycle the shell became more, or less, permeable. (The results are listed in Table 71.IV.) (These data are also a measure of the changing composition and structure of the shell.) The permeability of the PAMS mandrel was high ($K_p = 4.7 \times 10^{-15}$ mol·m/m²·Pa·s), which yields $\tau = 1.2$ min. The permeability of the polyamic-acid-coated mandrel (6.4 μm of polyamic acid) was considerably smaller ($K_p = 0.074 \times 10^{-15}$ mol·m/m²·Pa·s), which yields $\tau = 74$ min. Heating the shell to 100°C for 1.5 h decreased τ to 17 min. Further heating to 120, 140, and 150°C lowered τ to 8 to 10 min. After the 165°C cure stage, the time constant could not be measured. These data indicated the shell was becoming more permeable as imidization progressed, but more positive evidence was necessary to determine whether or not the fully imidized shell was permeable.

Table 71.IV: Permeation data for polyamic acid/polyimide shells (D₂ at 298 K).

Curing Condition	τ (min)	$K_p \times 10^{17}$ (mol·m/m ² ·Pa·s)
PAMS mandrel	1.18	470
Polyamic acid + PAMS mandrel: as-deposited	74.4	7.4
After 100°C at 1.5 h	16.9	32
After 120°C at 1.5 h	8.54	64
After 140°C at 3 h	10.8	51
After 150°C at 5 h	8.52	64

Since critical permeation data were unobtainable for polyimide shells, a more sensitive technique using flat, vapor-deposited polyimide films was tested to obtain the values. (The results are listed in Table 71.V.) The deuterium permeability was 2.0×10^{-14} mol·m/m²·Pa·s at 298 K, and the nitrogen permeability was 8.0×10^{-15} mol·m/m²·Pa·s at 298 K. While we cannot exclude the possibility that the rapid permeation may be due to interconnected pores or pinholes in the film, no pinholes have been observed (using both AFM and SEM scans) and the size and density of any porosity are unknown. These permeability values were used to calculate time constants for typical OMEGA-size shells (Table 71.V). The time constant

Table 71.V: Measured permeability of different shell materials used to calculate time constants for an OMEGA-size shell.

	Permeability at 25°C (mol•m/m ² •Pa•s)		Time constant for 1-mm-outer-diam, 5-μm-wall shell	
	D ₂	N ₂	D ₂	N ₂
PAMS	4.7 × 10 ⁻¹⁵	1.6 × 10 ⁻¹⁶	1.2 min	34 min
Polyamic acid/PAMS	8.4 × 10 ⁻¹⁷	–	66 min	–
VDP polyimide	2.0 × 10 ^{-14*}	8.5 × 10 ^{-15*}	17 s	39 s

*Data obtained using flat films.

for a 1-mm-outer-diam, 5-μm-wall shell would be 17 s for deuterium and 39 s for nitrogen. These very short values may explain why we were unable to measure time constants of actual shells.

4. Mechanical Properties and Behavior of Polyimide Shells

The elastic modulus and tensile strength of the polyimide shells must be known to define the necessary conditions to deliver DT-filled cryogenic targets: (1) the greater the elastic modulus, the greater the buckling pressure the target can withstand, and (2) the greater the tensile strength, the greater the burst pressure the target can endure. When combined with the permeation rate, these values determine the maximum rate at which the target can be filled and cooled for ICF cryogenic experiments.

Shells with a diameter between 800 and 900 μm and a wall thickness between 5 and 9 μm were repeatedly pressurized and depressurized using the protocol and equipment described previously. The shell’s buckle- and burst-pressure differential was measured with an accuracy of ±5 psi (0.34 atm). The initial pressurization rate was 0.01 atm/s and the maximum pressure was 45 atm. The depressurizing rate was 50 atm/s. (The minimum pressurization rate was based on initial estimations for permeability and elastic modulus of polyimide.) All of the shells survived every test. The pressurizing rate was increased to 3.5 atm/s, the maximum that could be achieved, to minimize permeation that would decrease the pressure differential across the shell wall. Shells deposited using the plasma-assisted technique buckled at an overpressure of ~36 atm. The failure mechanism was atypical of polystyrene and plasma polymers: an indent developed in the shell and the shell did not catastrophically disintegrate (Fig. 71.22). These shells exhibit a greater fracture toughness than do existing ICF targets. The shells deposited by the thermionic-assisted technique were more durable than those deposited by the plasma-assisted technique and did not buckle or burst.

The maximum pressure rating of the test apparatus was increased to 105 atm; shells deposited using thermionic assistance were repeatedly tested at incrementally higher pressures. The 8-μm-wall polyimide shell survived the maximum pressurization rate of 3.5 atm/s to 105 atm. Using the calculated permeation rate for nitrogen through polyimide (measured above), the maximum pressure differential across the shell wall (the buckle pressure) was ~60 atm, and, using the standard expression for the crush pressure,

$$P_{\text{buckle}} = \frac{2E}{\sqrt{3(1-\nu^2)}} \left(\frac{w}{r}\right)^2,$$

where *E* is the Young’s modulus, *ν* is the Poisson ratio, *w* is the wall thickness, and *r* is the shell radius;¹⁷ the modulus of the material was calculated to be ~15 GPa. For comparison, the

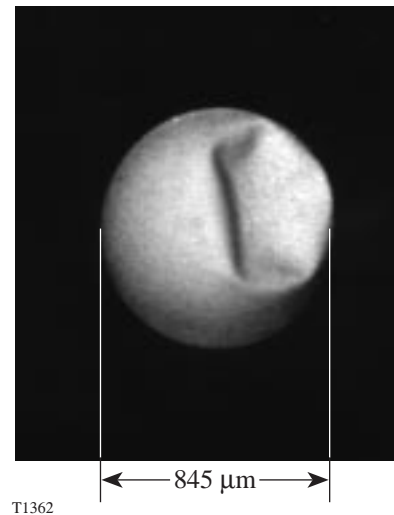


Figure 71.22 Plasma-assisted polyimide shell buckled at an external overpressure of ~36 atm. The shell did not brittle fracture, indicating a high fracture toughness.

largest reported literature value for the modulus of a solution-cast polyimide is 9.3 GPa. (A 1-mm-diam, 10- μ m-thick shell would crush with an external overpressure of 44 atm.)

All attempts to burst the shells deposited by the thermionic-assisted technique were unsuccessful. Shells were gradually filled with nitrogen at a rate of ~ 4 atm/min to a final pressure of 110 atm and rapidly depressurized at the maximum rate possible (~ 50 atm/s). Assuming that negligible permeation occurred during the 2-s depressurizing cycle, the burst pressure was greater than 100 atm. Using this pressure value and the standard hoop stress equation, $P_{\text{burst}} = 2T(w/r)$, the tensile strength T was calculated to be greater than 300 MPa. For reference, the highest reported tensile strength for a solution-cast polyimide is 420 MPa.

The same polyimide shell was sputter coated with a 1- μ m-thick aluminum layer to provide a permeation barrier layer, and the identical pressurization test was repeated. The shell neither buckled during pressurization nor burst during rapid depressurization. The calculated strength and modulus of polyimide shells are compiled in Table 71.VI.

5. Residual Stress Induced in Polyimide Films

As discussed previously, the imidizing cycle is the critical processing phase that affects the survivability and the resulting properties of the shells. The chemical changes that occur during the curing cycle have been described, and the effect these changes have on the mechanical properties of the film are now discussed.

As the temperature increases through the imidizing cycle, polyamic acid reacts (loses water) to form a polyimide. Unreacted monomers present in the film are sublimed, and the molecular weight and rigid structure of the polyimide increase. These mass, morphology, and structural changes alter the intrinsic stress in the polymer. If the polyamic acid was an unconstrained freestanding shell, the induced stress would be reduced by the shell shrinking or expanding to relieve the induced radial and hoop stresses. However, that stress-relief

mechanism does not occur at lower temperatures where the PAMS mandrel possesses sufficient strength to resist these dimensional changes.

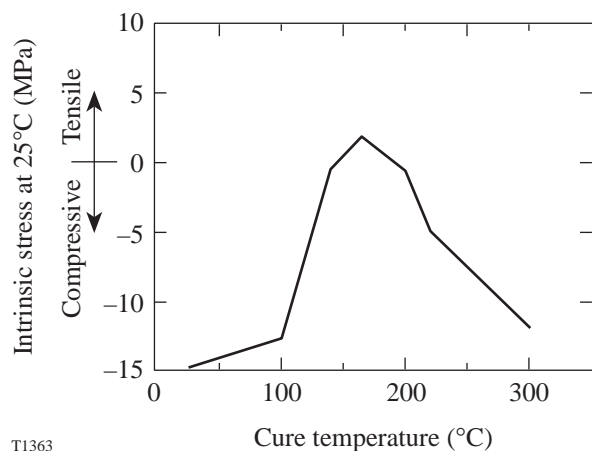
Below 110°C, the mandrel possesses significant material strength that constrains the polyamic acid. Above 110°C, the mandrel softens and the polyamic acid/polyimide can increasingly shrink or expand to relax the induced stress. Between 110°C and 180°C the α -methylstyrene vapor pressure increases within the shell and, together with the slumping PAMS mandrel, produces a nonuniform burst pressure on the polyamic acid/polyimide wall. (All the shells heated at rates greater than 1°C/min through the 110°C to 180°C regime exploded. Depolymerization of a typical PAMS mandrel would produce an estimated burst pressure of 45 atm at 150°C in the absence of permeation.) Above 180°C the polyamic acid continues to imidize and the PAMS mandrel has a decreasing influence on the process. All these effects contribute at varying degrees to the instantaneous stress in the shell wall.

The magnitude of stress in the polyamic acid/polyimide composite film at the important processing temperatures (100, 140, 165, 220, and 300°C) was measured using a 14- μ m polyamic acid film deposited on a silicon witness beam, as shown in Fig. 71.23. These data are corrected for the extrinsic thermal stress. (Flat films were used because no suitable technique was available to measure the stress that evolves in a shell.) Note: The data measured only the stresses that develop in polyimide during a specific cure cycle; additional stresses will exist in the polyimide shell because of the spherical geometry and the presence of the mandrel.

The intrinsic stress in the as-deposited film was ~ 15 MPa compressive. Heating the film to 100°C for 3 h induced a tensile stress. The maximum induced stress was 17 MPa at 165°C, where, coincidentally, the induced tensile stress offset the initial compressive stress. The tensile nature of the stress was expected as the film lost mass but was constrained at the interface by the substrate.

Table 71.VI: Calculated strength and modulus of polyimide shells made by the two techniques.

	Elastic Modulus (GPa)	Ultimate Tensile Strength (MPa)
Plasma-assisted polyimide	5.5	95
Thermionic-assisted polyimide	~ 15 (minimum)	300 (minimum)



T1363

Figure 71.23
Temperature dependence of the intrinsic stress at 25°C in a polyamic acid/polyimide film.

As the temperature increased to 300°C, the compressive stress in the film returned to 14 MPa. The origin of this stress may be explained by steric considerations: as the molecular weight of the polyimide increased, the polymer chains became more rigid and the scale length of the polyimide increased. This repelling interference of the polyimide chains was constrained by the chains being intertwined and cross-linked, resulting in a compressive force. This behavior would be expected to increase the porosity (nanoscale) of the material and may also explain why the imidized material is more permeable than the polyamic acid.

The geometry of the shell creates an additional stress not present in an unconstrained film: the inner surface will be under greater compressive strain than will the outer surface, and the resulting stress will be in addition to the intrinsic stress measured above. The stress difference will be small for thin-walled, OMEGA-size shells, and, since the magnitude of the intrinsic stress is expected to be small, the induced residual stresses in the shell wall are not significant. Knowing how the intrinsic stress changes with temperature will be used to optimize the imidizing cycle to obtain thinner-walled shells.

By contrast, NIF targets are thick-walled shells, and it is possible that a sizable stress gradient will exist across the wall. When the shell is filled to its specified pressure (currently 360 atm), the maximum tensile stress will be at the inner surface. And, if a sizable residual stress is also present, the maximum pressure rating of the target will be reduced. These considerations make it important to know the magnitude of the

induced stress. A desirable property of the polyimide shells observed here was the fracture toughness of the material; if the inner surface of a target experienced a localized highly strained region and a crack developed, the crack would help dissipate the stress, thereby avoiding catastrophic shell failure. This property may make transporting NIF cryogenic targets at room temperature more feasible.

Summary

A viable method for fabricating polyimide shells as potential targets for direct-drive ICF cryogenic experiments on OMEGA has been demonstrated. Shells with diameters ranging from 0.7 to 0.9 mm and wall thicknesses from 4 to 13 μm have been fabricated. Initial estimates of the elastic modulus, tensile strength, permeability, stress, composition, surface roughness, and burst/buckle pressures have been obtained. All of the effort discussed here has been devoted to obtaining polyimide shells and characterizing the resulting properties. No attempt has been made to optimize the processing conditions to improve the material properties. Importantly, no fundamental impediments were observed that would prevent polyimide shells being used as ICF targets. However, there are clearly many areas where the quality of the shell must be improved before the targets can be used for cryogenic experiments. That effort is the subject of future work.

The initially proposed mechanical-strength advantages of polyimide material have been experimentally substantiated: The shells are significantly stronger than existing polystyrene and plasma polymer shells. An initial concern about the low permeability of polyimide has been dispelled. In fact, the permeability is so high that future study is required to confirm that the permeability is an inherent material property and that the data are not distorted by unobserved interconnected porosity. Also, the impermeability of the shell at 20 K must be demonstrated.

ACKNOWLEDGMENT

This work was supported by the U.S. Department of Energy Office of Inertial Confinement Fusion under Cooperative Agreement No. DE-FC03-92SF19460, the University of Rochester, and the New York State Energy Research and Development Authority. The support of DOE does not constitute an endorsement by DOE of the views expressed in this article.

REFERENCES

1. J. J. Sanchez and S. A. Letts, *Fusion Technol.* **31**, 491 (1997).
2. T. Takekoshi, in *Polyimides: Fundamentals and Applications*, edited by M. Ghosh and K. Mittal, *Plastics Engineering*, Vol. 36 (Marcel Dekker, New York, 1996), p. 7.

3. J. R. Salem *et al.*, *J. Vac. Sci. Technol. A* **4**, 369 (1986).
4. M. Iijima *et al.*, *J. Vac. Sci. Jpn.* **28**, 437 (1985).
5. S. A. Letts *et al.*, *Fusion Technol.* **28**, 1797 (1995).
6. S. A. Letts, D. W. Myers, and L. A. Witt, *J. Vac. Sci. Technol.* **19**, 739 (1981).
7. E. L. Alfonso, S.-H. Chen, M. D. Wittman, S. Papernov, and D. Harding, *Polymer* **38**, 1639 (1997).
8. B. McQuillan, presented at the ICF Target Fabrication Meeting, FY97 Mid-Year Review, San Diego, CA, 23–25 April 1997.
9. C. W. Hutchings and M. Grunze, *Rev. Sci. Instrum.* **66**, 3943 (1995).
10. Y. Takahashi *et al.*, *Macromolecules* **24**, 3543 (1991).
11. M. Bonino, R. Q. Gram, D. Harding, S. Noyes, J. Soares, and M. Wittman, presented at the Eleventh Target Fabrication Specialists' Meeting, Orcas Island, WA, 9–12 September 1996.
12. *Annual Book of ASTM Standards*, ASTM Designation: D 1434 - 82 (Reapproved 1992) (1994), Vol. 15.09, pp. 204–215.
13. G. G. Stoney, *Proc. R. Soc. Lond. A* **82**, 172 (1909).
14. J.-H. Jou *et al.*, *J. Polym. Sci. Polym. Phys. Ed.* **34**, 2239 (1996).
15. M. Langsam, in *Polyimides: Fundamentals and Applications*, edited by M. Ghosh and K. Mittal, *Plastics Engineering*, Vol. 36 (Marcel Dekker, New York, 1996), p. 697.
16. R. M. Ikeda *et al.*, *J. Appl. Polym. Sci.* **25**, 1391 (1980).
17. T. H. Hsu, *Structural Engineering & Applied Mechanics Data Handbook*, Volume 4: Shells (Gulf Publishing Company, Houston, 1991), p. 349.

Sideward Stimulated Raman Scattering of a Short Laser Pulse in a Plasma Channel

Stimulated Raman scattering (SRS)¹ is the decay of an incident, or pump, light wave (0) into a frequency-downshifted, or Stokes, light wave (1) and an electron-plasma wave (2). The conservation of energy and momentum in this decay is signified by the frequency and wave-vector matching conditions

$$\omega_0 = \omega_1 + \omega_2, \quad \mathbf{k}_0 = \mathbf{k}_1 + \mathbf{k}_2, \quad (1)$$

in which (ω_0, \mathbf{k}_0) and (ω_1, \mathbf{k}_1) satisfy the dispersion relation $\omega = (\omega_e^2 + c^2 k^2)^{1/2}$, where ω_e is the electron-plasma frequency,¹ and (ω_2, \mathbf{k}_2) satisfies the dispersion relation $\omega = \omega_e$. The wave-vector matching condition is illustrated in Fig. 71.24(a).

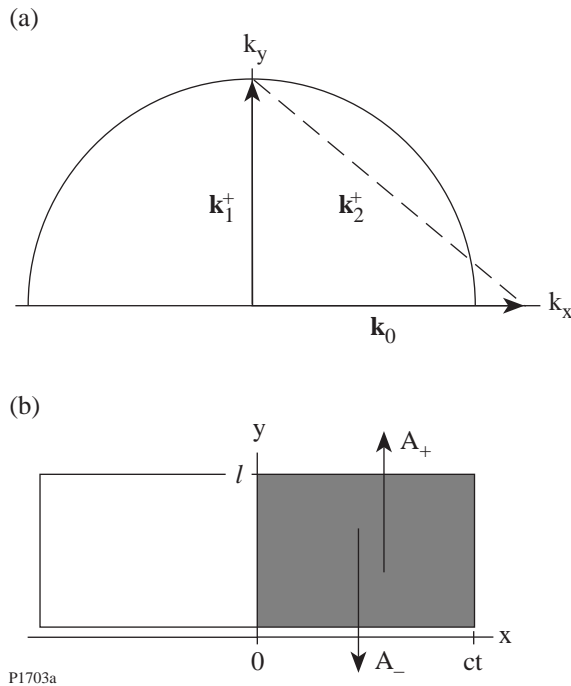


Figure 71.24
Geometry of sideward SRS. (a) Wave-vector diagram for the upward (+) decay. The wave-vector diagram for the downward (-) decay is similar. (b) Region of the plasma illuminated by the laser pulse.

The SRS of a short laser pulse is important in the contexts of particle acceleration² and inertial confinement fusion.^{3,4} In previous studies of the spatiotemporal evolution of SRS,⁵⁻¹³ the Stokes waves were allowed to pass freely through the pulse boundaries. However, the radial ponderomotive force associated with the pulse can expel plasma from the neighborhood of the pulse axis, in which case SRS occurs in a plasma channel.¹⁴ A channel can also be preformed by a second pulse.¹⁵ The reflection of light by the channel walls couples Stokes waves propagating symmetrically relative to the pulse axis, as shown in Fig. 71.24(b), and enhances the growth of oblique SRS.

In this study we investigate the effects of reflections on sideward SRS in a plasma channel. Sideward SRS is a useful paradigm of oblique SRS because its two-dimensional geometry is representative of oblique SRS, but simple enough to preclude some of the mathematical complications associated with oblique SRS.¹³ To analyze SRS in an optical fiber, one decomposes the radial structure of the waves into the eigenmodes of the fiber.¹⁶ We avoid the difficulties associated with the determination of the (evolving) channel profile and the associated radial eigenmodes by using an empirical parameter r to characterize reflections from the channel walls.¹⁷

Mathematical Analysis

In the weak-coupling regime, the initial evolution of sideward SRS in an underdense plasma is governed by the linearized equations

$$(\partial_t \pm c\partial_y)A_{\pm} = \gamma_0 N_{\pm}, \quad \partial_t N_{\pm} = \gamma_0 A_{\pm}, \quad (2)$$

where A_{\pm} represents the vector potentials associated with the Stokes waves, N_{\pm} represents the density fluctuations associated with the electron-plasma waves, and $\gamma_0 = \omega_2 c |\mathbf{k}_2| A_0 / 4(\omega_0 \omega_2)^{1/2}$ is the temporal growth rate of SRS in an infinite plasma.¹ It is advantageous to define the characteristic variables $\tau = (ct - x)/l$ and $\eta = y/l$, in terms of which Eqs. (2) become

$$(\partial_\tau \pm \partial_\eta)A_\pm = \gamma N_\pm, \quad \partial_\tau N_\pm = \gamma A_\pm, \quad (3)$$

where $\gamma = \gamma_0 l/c$.¹⁸ These equations are to be solved subject to the initial conditions

$$A_\pm(0, \eta) = 0, \quad N_\pm(0, \eta) = 1, \quad (4)$$

which are representative of a pulse convecting into fresh plasma, in which a constant level of density fluctuations is available to seed the instability, and the boundary conditions

$$A_+(\tau, 0) = r A_-(r, 0), \quad A_-(\tau, 1) = r A_+(\tau, 1). \quad (5)$$

It follows from Eqs. (3)–(5) that $A_-(\tau, \eta) = A_+(\tau, 1 - \eta)$ and $N_-(\tau, \eta) = N_+(\tau, 1 - \eta)$. Consequently, only the solutions for A_+ and N_+ will be stated explicitly.

One can solve Eqs. (3)–(5) by using Laplace transforms. For the special case in which $r = 0$ the wave amplitudes are given by

$$A_+(\tau, \eta) = \begin{cases} \sinh(\gamma\tau), \\ \sum_{n=0}^{\infty} F_{2n+1}(\tau, \eta), \end{cases} \quad N_+(\tau, \eta) = \begin{cases} \cosh(\gamma\tau), \\ \sum_{n=0}^{\infty} F_{2n}(\tau, \eta), \end{cases} \quad (6)$$

where

$$F_n(\tau, \eta) = [\eta/(\tau - \eta)]^{n/2} I_n \left\{ 2\gamma [\eta(\tau - \eta)]^{1/2} \right\} \quad (7)$$

and I_n is the modified Bessel function of order n . The first forms of Eqs. (6) are valid for $\tau \leq \eta$ and the second forms are valid for $\tau > \eta$. At any point (x, y) in the plasma, the pulse arrives and initiates the instability at $t = x/c$, after which the Stokes amplitude experiences exponential growth with growth rate γ_0 . The information that the side boundary at $y = 0$ is present reaches that point at $t = (x + y)/c$, after which the Stokes wave experiences Bessel growth. Since $I_n(z) \approx \exp(z)/(2\pi z)^{1/2}$ when $z \gg 1$, the Stokes amplitude grows in proportion to $\exp[2\gamma_0(yt/c)^{1/2}]$ when $t \gg (x + y)/c$. At these late times, $t \gg (yt/c)^{1/2}$. Thus, *the sideward convection of the Stokes wave converts fast exponential growth to slow Bessel growth*. A snapshot of the Stokes amplitude is displayed in Fig. 71.25(a) for the case in which $ct/l = 2$ and $\gamma_0 l/c = 2$.¹⁹ The transition from one-dimensional exponential growth to two-dimensional Bessel growth is evident.

For the special case in which $r = 1$, the wave amplitudes are given by

$$A_+ = \sinh(\gamma\tau), \quad N_+ = \cosh(\gamma\tau). \quad (8)$$

Thus, *the total reflection of the Stokes light maintains the fast exponential growth of sideward SRS, even after the information that the pulse boundaries are present has reached the pulse interior*. A snapshot of the Stokes amplitude is displayed in Fig. 71.25(b) for the case in which $ct/l = 2$ and $\gamma_0 l/c = 2$. It is evident that total reflection allows the wave evolution to remain one-dimensional and enhances the wave growth. What must be determined is how large a reflectivity is needed to have a significant effect.

For the general case in which $0 < r < 1$, the wave amplitudes satisfy the reflection principle

$$A_+(\tau, \eta|r) = \sum_{n=0}^{\infty} r^n A_+(\tau, \eta + n|0), \quad (9)$$

$$N_+(\tau, \eta|r) = \sum_{n=0}^{\infty} r^n N_+(\tau, \eta + n|0).$$

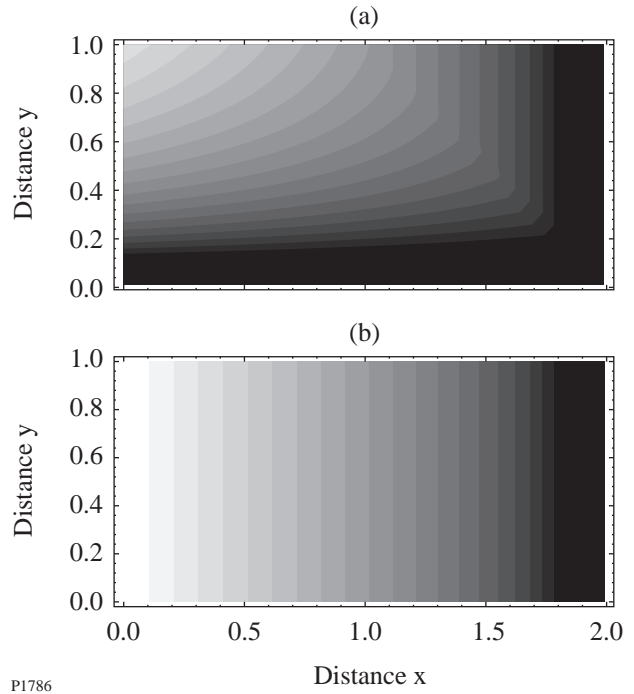


Figure 71.25

Contour plots of the logarithm of the Stokes intensity for cases in which $ct/l = 2$ and $\gamma_0 l/c = 2$. White corresponds to high intensity and black corresponds to low intensity. (a) $r = 0$; (b) $r = 1$.

For $0 \leq \eta \leq 1$ the fundamental solutions $A_+(\tau, \eta|0)$ and $N_+(\tau, \eta|0)$ are given by Eqs. (6). For $\eta > 1$ the fundamental solutions are zero until $\tau = \eta - 1$. Subsequently,

$$A_+(\tau, \eta|0) = \begin{cases} \sinh(\gamma\tau) - \sum_{n=0}^{\infty} F_{2n+1}(\tau, \eta-1), \\ \sum_{n=0}^{\infty} F_{2n+1}(\tau, \eta) - \sum_{n=0}^{\infty} F_{2n+1}(\tau, \eta-1), \end{cases} \quad (10)$$

$$N_+(\tau, \eta|0) = \begin{cases} \cosh(\gamma\tau) - \sum_{n=0}^{\infty} F_{2n}(\tau, \eta-1), \\ \sum_{n=0}^{\infty} F_{2n}(\tau, \eta) - \sum_{n=0}^{\infty} F_{2n}(\tau, \eta-1), \end{cases}$$

where the first forms are valid for $\eta - 1 < \tau \leq \eta$ and the second forms are valid for $\tau > \eta$. The modification of solutions (6) described by Eqs. (10) is associated with a pulse of infinite width and the initial condition $N_+(0, \eta) = H(1 - \eta)$, where H is the Heaviside step function. At early times, the wave amplitudes grow exponentially in time with growth rate γ_0 . At intermediate and late times the solutions involve doubly infinite sums of Bessel functions that represent the fundamental contributions to the wave amplitudes and the contributions caused by reflections at the pulse boundaries. A snapshot of the Stokes amplitude described by the exact Eqs. (6), (9), and (10) is displayed in Fig. 71.26(a) for the case in which $r = 0.5$, $ct/l = 2$, and $\gamma_0 l/c = 2$. By comparing Figs. 71.25(a) and 71.26(a), one can see that reflections do not affect the wave evolution in the region $y \geq ct - x$. Reflections affect the wave evolution significantly in the region $y < ct - x$. Despite the complexity of solutions (9), by analyzing the Laplace-transformed solutions from which they originated one can show that, at late times,

$$A_+(\tau, \eta|r) \approx \frac{\gamma(1-r)\exp(v\eta + \lambda\tau)}{v(2\lambda + v)}, \quad (11)$$

$$N_+(\tau, \eta|r) \approx \frac{\gamma^2(1-r)\exp(v\eta + \lambda\tau)}{\lambda v(2\lambda + v)},$$

where

$$\lambda = -v/2 + (\gamma^2 + v^2/4)^{1/2} \quad (12)$$

is the growth rate and

$$v = -\log r \quad (13)$$

characterizes the convective loss of Stokes light through the pulse boundaries. A snapshot of the Stokes amplitude de-

scribed by the approximate Eqs. (11)–(13) is displayed in Fig. 71.26(b). Although the approximate solutions (11) are inaccurate near the leading edge of the pulse, as one should expect, they are extremely accurate in the body of the pulse. The growth rate (12) is plotted as a function of r in Fig. 71.27 for the case in which $\gamma_0 l/c = 2$. For this case $r = 0.05$ is

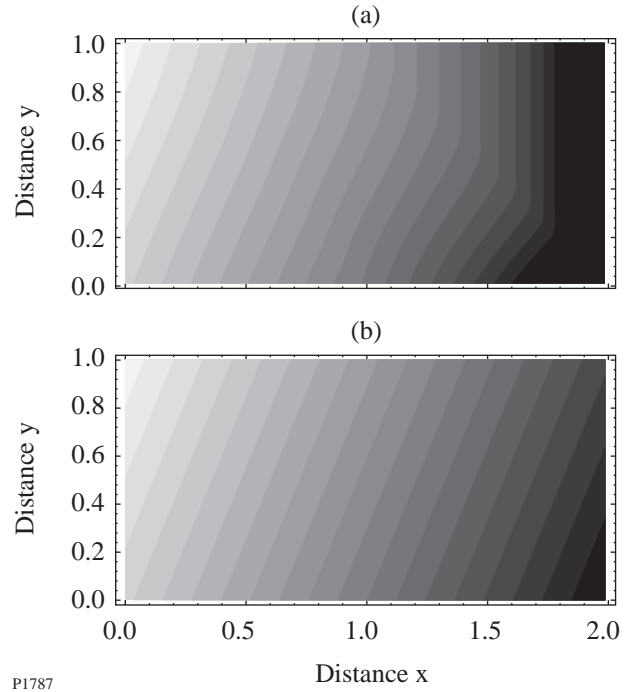


Figure 71.26
Contour plots of the logarithm of the Stokes intensity for the case in which $ct/l = 2$, $\gamma_0 l/c = 2$, and $r = 0.5$. White corresponds to high intensity and black corresponds to low intensity. (a) Exact solution described by Eqs. (6), (9), and (10); (b) approximate solution described by Eqs. (11)–(13).

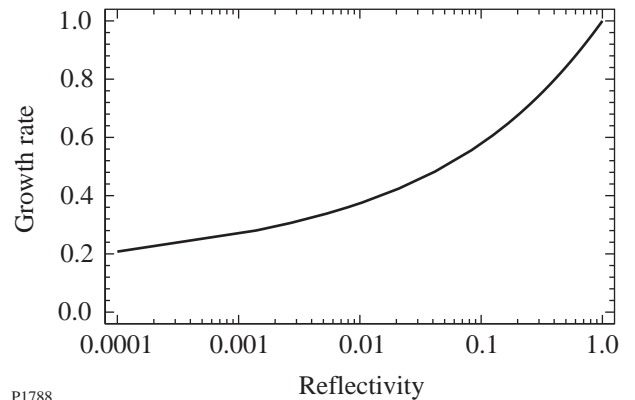


Figure 71.27
Normalized growth rate [Eq. (12)] plotted as a function of r for the case in which $\gamma_0 l/c = 2$.

sufficient to maintain exponential growth with $\lambda = 0.5\gamma$. In general, $r = \exp(-3\gamma/2)$ is sufficient to maintain this rate of exponential growth. Thus, *even weak reflections enhance the growth of sideward SRS significantly.*

Physical Model

Because of the significance of Eqs. (11)–(13), it is important to understand the physical principles on which they are based. The eigenmodes of a fiber are formed by internal reflection, and their existence is not predicated on the existence of SRS.¹⁶ These facts prompt the solution of Eqs. (3) and (5), with $\gamma = 0$. Subject to the initial conditions

$$A_{\pm}(0, \eta) = 1, \quad (14)$$

the solution of these equations is

$$A_+(\tau, \eta) = \sum_{n=0}^{\infty} r^n [H(\tau + 1 - \eta - n) - H(\tau - \eta - n)]. \quad (15)$$

Solution (15) is displayed in Fig. 71.28, together with the function

$$A_+(\tau, \eta) = [(1 - r)/\nu] \exp(\nu\eta - \nu\tau), \quad (16)$$

which is the fundamental term in the residue series expansion of solution (15). Because of the tendency of the Stokes wave to propagate out of the plasma, the Stokes amplitude at the right boundary is reduced by a factor of $1/r = \exp(\nu)$ when $\tau = n$. The continuous function $\exp(-\nu\tau)$ captures this essential feature of the temporal wave evolution. When $\tau \neq n$, the right part of the Stokes wave has experienced one less reflection than the left part. Consequently, the Stokes amplitude at the right boundary is larger than the Stokes amplitude at the left boundary by a factor of $1/r$. The continuous function $\exp(\nu\eta)$ captures this essential feature of the spatial wave evolution. If one substitutes the ansatz $A_+(\tau, \eta) = a_+(\tau) \exp(\nu\eta)$ in Eqs. (3) and (5), with $\gamma = 0$, one finds that the wave amplitude decays exponentially in time, with decay rate ν , in agreement with Eq. (16). Similarly, if one substitutes the ansatz $A_+(\tau, \eta) = a_+(\tau) \exp(\nu\eta)$ and $N_+ = n_+(\tau) \exp(\nu\eta)$ in Eqs. (3) and (5), with $\gamma \neq 0$, one finds that the wave amplitudes grow exponentially in time, with growth rate $\lambda = -\nu/2 + (\gamma^2 + \nu^2/4)^{1/2}$, in agreement with Eq. (12). Thus, solutions (11) are consistent with the formation of a spatial eigenmode that grows in the presence of the pulse.

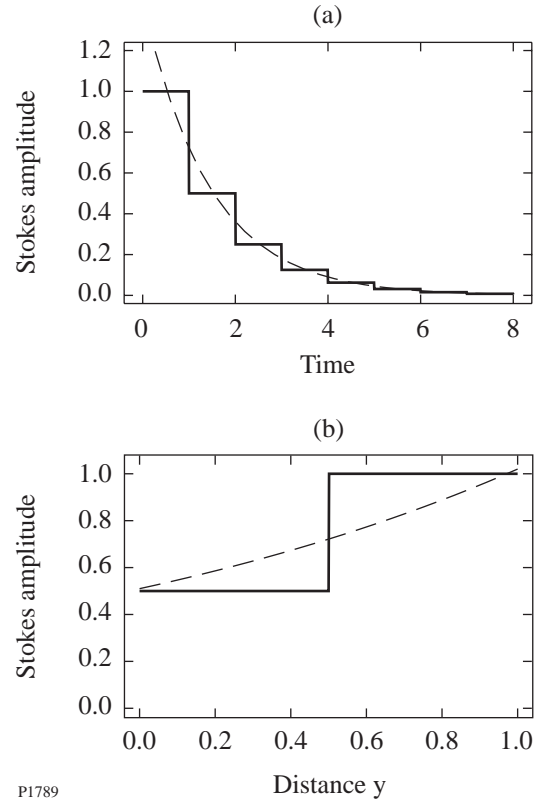


Figure 71.28

Evolution of the Stokes wave for the case in which $\gamma_0 l/c = 2$. The solid lines denote the exact solution (15) and the broken lines denote the approximate solution (16). (a) Stokes amplitude at $y/l = 1$ plotted as a function of ct/l ; (b) Stokes amplitude at $ct/l = 0.5$ plotted as a function of y/l .

Summary

In summary, we studied the spatiotemporal evolution of sideward SRS in the weak-coupling regime. In a uniform plasma the sideward convection of the Stokes wave inhibits the growth of sideward SRS. In a plasma channel the partial reflection of Stokes light by the channel walls allows a spatial eigenmode to form in the body of the laser pulse. After this eigenmode has formed, it grows exponentially in time for the subsequent duration of the pulse. The growth rate (12) depends directly on the reflectivity of the channel walls, which, in turn, depends directly on their height. Even weak reflections enhance the growth of sideward SRS significantly. We also made a preliminary analysis of sideward SRS in the strong-coupling regime. Although strong coupling changes the rate at which the instability grows, it does not change the qualitative features of instability growth described herein. In particular, the partial reflection of Stokes light by channel walls allows a spatial

eigenmode to form in the body of the pulse, and the ansatz described after Eq. (16) can be used to determine the rate at which it grows. For channels created by the pulse, the height of the channel walls depends directly on the pulse intensity. However, since pulses of high intensity evacuate the channel completely, sideward SRS is most important for pulses of moderate intensity. In future work we will apply the physical insights gained in this study of sideward SRS to the study of near-forward and near-backward SRS. Reflections are stronger for these instabilities than for sideward SRS because the Stokes waves approach the channel walls at grazing, rather than normal, incidence. A significant amount of near-forward SRS was observed in recent particle-in-cell simulations of pulse propagation in an underdense plasma.^{20,21}

ACKNOWLEDGMENT

We acknowledge useful conversations with V. T. Tikhonchuk and E. A. Williams. This work was supported by the National Science Foundation under Contract No. PHY-9415583, the Department of Energy (DOE) Office of Inertial Confinement Fusion under Cooperative Agreement No. DE-FC03-92SF19460, the University of Rochester, and the New York State Energy Research and Development Authority. The support of DOE does not constitute an endorsement by DOE of the views expressed in this article.

REFERENCES

1. W. L. Kruer, *The Physics of Laser Plasma Interactions*, Frontiers in Physics, Vol. 73 (Addison-Wesley, Redwood City, CA, 1988), Chap. 7.
2. J. M. Dawson, *Sci. Am.* **260**, 54 (1989).
3. R. S. Craxton, R. L. McCrory, and J. M. Soures, *Sci. Am.* **255**, 68 (1986).
4. M. Tabak *et al.*, *Phys. Plasmas* **1**, 1626 (1994).
5. C. J. McKinstrie and R. Bingham, *Phys. Fluids B* **4**, 2626 (1992).
6. T. M. Antonsen, Jr. and P. Mora, *Phys. Rev. Lett.* **69**, 2204 (1992).
7. T. M. Antonsen, Jr. and P. Mora, *Phys. Fluids B* **5**, 1440 (1993).
8. W. B. Mori *et al.*, *Phys. Rev. Lett.* **72**, 1482 (1994).
9. S. C. Wilks *et al.*, *Phys. Plasmas* **2**, 274 (1995).
10. C. J. McKinstrie, R. Betti, R. E. Giacone, T. Kolber, and E. J. Turano, *Phys. Rev. E* **51**, 3752 (1995).
11. C. D. Decker *et al.*, *Phys. Plasmas* **3**, 1360 (1996).
12. C. J. McKinstrie and E. J. Turano, *Phys. Plasmas* **3**, 4683 (1996).
13. C. J. McKinstrie and E. J. Turano, "Spatiotemporal Evolution of Parametric Instabilities Driven by Short Laser Pulses: Two-Dimensional Analysis," to be published in *Physics of Plasmas*.
14. P. Monot *et al.*, *Phys. Rev. Lett.* **74**, 2953 (1995).
15. H. M. Milchberg *et al.*, *Phys. Plasmas* **3**, 2149 (1996).
16. G. P. Agrawal, *Nonlinear Fiber Optics* (Academic Press, Boston, 1989), Chap. 2.
17. V. L. Ginzburg, *The Propagation of Electromagnetic Waves in Plasmas*, International Series of Monographs on Electromagnetic Waves, Vol. 7 (Pergamon Press, Oxford, 1964), p. 204.
18. When the plasma corrections to the group speeds of the light waves are important, the first of Eqs. (2) becomes $(\partial_t \pm v_1 \partial_y) A_{\pm} = \gamma_0 N_{\pm}$, where v_1 is the group speed of the Stokes waves and $\gamma_0 = \omega_2 c |\mathbf{k}_2| A_0 / 4 [(\omega_0 - \omega_2) \omega_2]^{1/2}$, and the characteristic variables become $\tau = (v_0 t - x)/l$ and $v_0 y / v_1 l$. Equations (3)–(5) are unchanged.
19. For sideward SRS in an underdense plasma, $\gamma_0 l / c \approx 2.2(n_e/n_c)^{1/4} (l/\lambda_0)(v_0/c)$, where λ_0 is the laser wavelength and v_0 is the quiver speed of electrons oscillating in the laser field. One possible set of parameters for which $\gamma_0 l / c \approx 2$ is $n_e/n_c = 0.01$, $l/\lambda_0 = 10$, and $v_0/c = 0.3$.
20. C. D. Decker, W. B. Mori, and T. Katsouleas, *Phys. Rev. E* **50**, R3338 (1994).
21. K.-C. Tzeng, W. B. Mori, and C. D. Decker, *Phys. Rev. Lett.* **76**, 3332 (1996).

Picosecond Photoresponse in Polycrystalline Silicon

The OMEGA laser driver line currently incorporates silicon (Si) photoconductive switches as part of the electro-optic pulse-shaping system. These switches conceptually serve two functions: (1) to generate an electrical square pulse with a sharp leading and trailing edge, when illuminated by a short optical pulse;¹ (2) to appropriately direct a broadband (0.1- to 10-GHz) shaped electrical pulse to the Mach–Zehnder integrated-optic modulator. The operating characteristics of the switches are optimized by minimizing the rise and fall times of the generated electrical square pulse and by maximizing the bandwidth of the directed broadband electrical shaped pulse.² Because the performance requirements of photoconductive switches in OMEGA pulse shaping are stringent and sometimes conflicting, a thorough exploration of the silicon photoconductive process is important.

In this article we address the generation of laser-pulse-induced electrical transients with short rise times, using silicon photoconductive switches. Related aspects of photoconductive switching, such as response at different laser wavelengths and Si integrated-circuit compatibility, are considered. We also explore the optimization of electrical pulse generation by probing the intrinsic limits of the Si and polycrystalline Si (polySi) material. In the 1980s Auston³ and others studied processing methods to reduce the Si intrinsic photoresponse time far below the microsecond limit set by its free-carrier lifetime. Although very fast responses were generated, the temporal resolution of the measurement equipment at that time was not sufficient to directly resolve the rise and fall times of the resulting photoresponse. To circumvent this measurement bandwidth limitation, optoelectronic correlation methods were developed.⁴ Correlation takes advantage of the switch itself by using another, similarly fast photoconductive switch in a pulser/sampler configuration. The measured response from the sampler is then a correlation of the two switch responses. This procedure, however, does not allow direct reconstruction of the switch response because, even if the switch geometries are identical, the measured response is not equivalent to a true autocorrelation since the electric fields across the gaps have different time evolutions. This is important because many

parameters of the photoconductive switches, such as carrier mobility and trapping, vary with the applied electric field strength. Therefore, detailed knowledge of the Si photoresponse and how it depends on the switch bias and illumination for different Si process conditions could not be determined.

We have measured the Si switch response at 800 nm and at the typical communication wavelength of 1.55 μm , using a 34-GHz sampling oscilloscope to quickly and easily measure properties dependent on charge (current integral) effects, such as quantum efficiency and saturation. We have also used an electro-optic (EO) sampling system capable of measuring submillivolt and subpicosecond responses.⁵ This allowed direct observation of the Si photoresponse rise and fall times.

Sample Preparation and Characterization

The tested samples were 2.3- μm -thick, 2 \times 2-mm, low-pressure chemical-vapor-deposited (LPCVD) films of polySi grown at a substrate temperature of 600°C in 200 mTorr of silane. A 1- μm -thick multilayer of metal was evaporated onto the polySi in an interdigitated fashion. The top layer was Au for solderability, while the bottom layer was Al for good adhesion to Si and to promote ohmic-like contacts. The samples were not annealed, and no implantation or etching was performed. Instead of growing the film on a silicon substrate with an oxide insulating layer, we used a fused silica substrate to facilitate switch illumination. This optimized the oscilloscope test fixture bandwidth because the sample could be directly soldered in a flip-chip manner across a microstrip gap, eliminating bandwidth-limiting discontinuities such as inductive wire-bond leads. Illuminating the sample from the back side (through the silica) also leads to reflection of the incident laser illumination from the top metal contacts, increasing rather than decreasing the number of photons absorbed, as front-side illumination would have done.

For characterization purposes, the polySi surface was etched preferentially at the grain boundaries, and a scanning electron microscope (SEM) image taken of the surface (see Fig. 71.29) revealed a polygrain size of approximately 30 nm. A sample

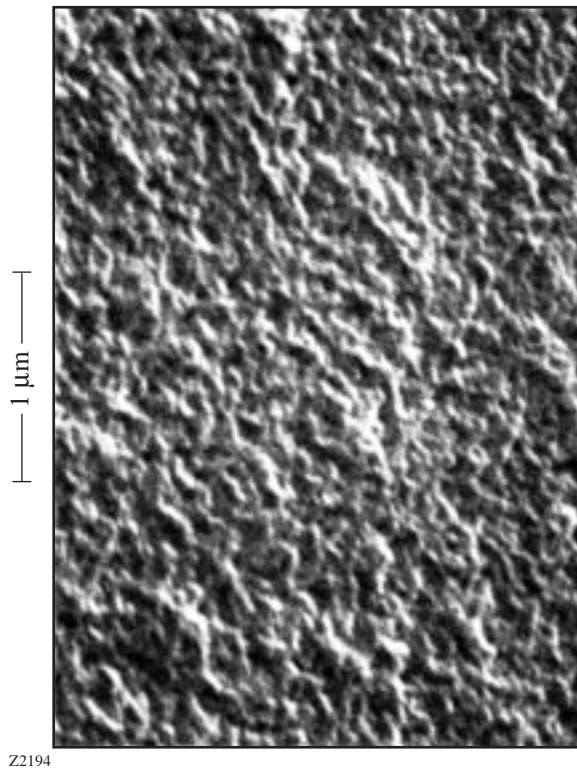


Figure 71.29
An SEM image of the polySi surface taken after preferential etching at grain boundaries reveals grain sizes of the order of 30 nm.

was also cleaved, and a 4-nm conductive silver layer was evaporated onto the exposed face, allowing a high-resolution SEM photograph of the switch cross section to be taken (see Fig. 71.30). The image shows the silica substrate beneath the 2.3- μm layer of polySi; on the top is a multilayer of metal that allows a robust, repeatable low-temperature-solder contact between the polySi and the microstrip transmission line. Close inspection of the grown polySi layer reveals some evidence of columnarity in the growth direction of the Si grains, which is not unexpected; however, the measurements were not significantly affected since the current flow was primarily in the direction normal to the silicon growth.

To independently confirm the polySi grain size and obtain preliminary data on absorption depth, a Perkin-Elmer Lambda 9 spectrophotometer was used to measure the transmission of the polySi-on-silica sample (see Fig. 71.31). The data, corrected for thin-film etalon fringes, show a broadened absorption band edge and a small but measurable amount of absorption in the energy bandgap, which is consistent with the small-grain microcrystalline film morphology observed in the SEM.

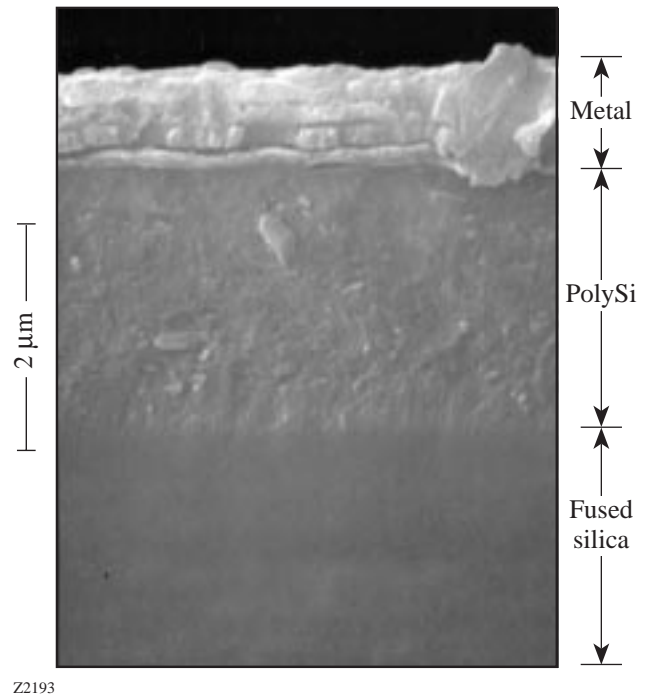


Figure 71.30
An SEM cross-section image showing the metal multilayer on the 2.3- μm polySi layer.

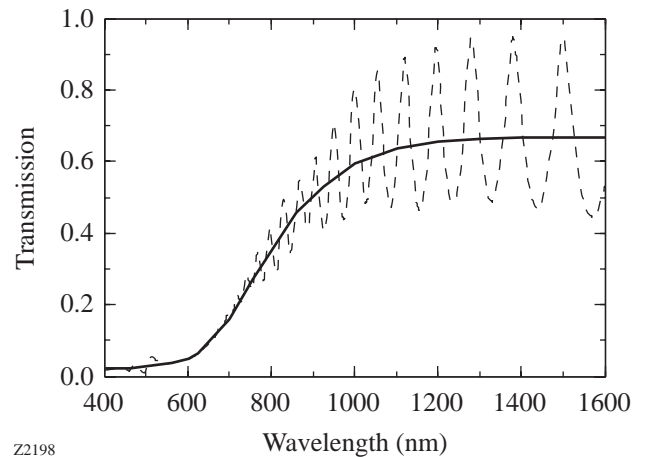


Figure 71.31
Transmission spectra of the polySi sample (solid line), corrected for thin-film etalon effects (dashed line).

Measurement and Experimental Results

A 34-GHz (10-ps intrinsic rise time) sampling oscilloscope measurement setup, shown in Fig. 71.32, allowed convenient measurement of relative quantum efficiencies for various laser wavelengths, since our EO sampling system operated up to only near-infrared wavelengths and did not extend into the fiber optic communication wavelengths. The oscilloscope measurements also permitted convenient testing of the switch signal's dependence on voltage bias (Fig. 71.33) and illumination power (Fig. 71.34). These two plots, taken at a laser wavelength of 800 nm, show that the switch response is linear

with both the voltage bias and incident laser fluence, indicating that the switch was not saturated. Additionally, the pulse-width dependence (Fig. 71.35) on bias voltage was nearly nonexistent, indicating that the photoresponse time was not due to carrier sweep-out but limited by either the free-carrier lifetime or the RC time constant of the switch. Since, as we will demonstrate later, EO sampling measurements show that the material response is in the 3-ps range, we can conclude that the observed photoresponse of our polySi switch is limited by the switch interdigitated geometry and the switch fixture RC time constant.

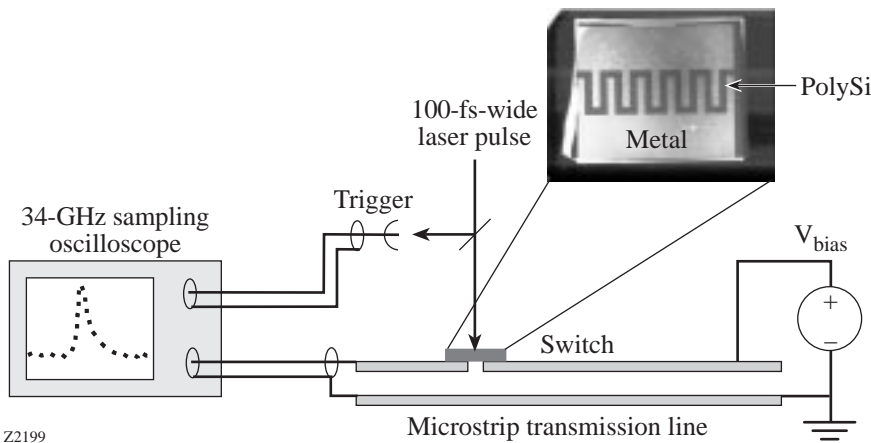
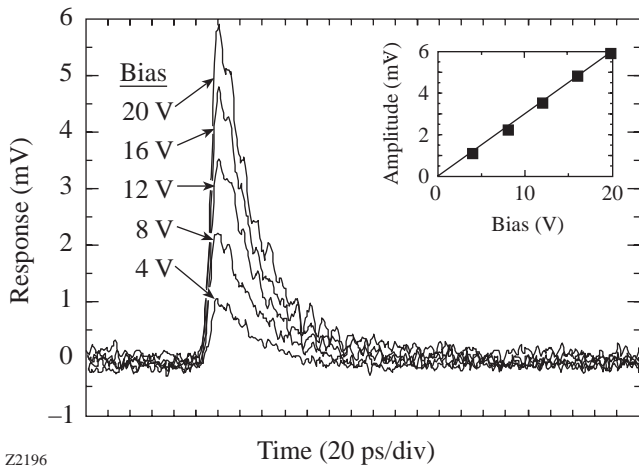
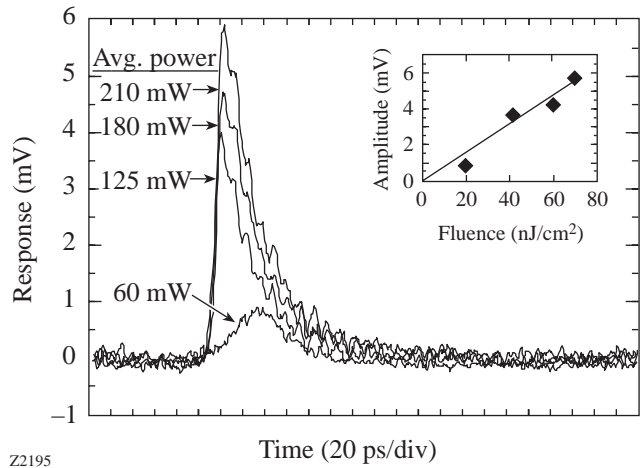


Figure 71.32 Sampling oscilloscope measurement setup. Inset shows the interdigitated switch geometry. Switch dimension is 2 mm × 2 mm; finger separation as well as finger width is 100 μm.



Z2196

Figure 71.33 The photoresponse at 800-nm illumination wavelength measured for different switch bias levels. The inset plots a linear dependence on gap voltage bias.



Z2195

Figure 71.34 The photoresponse at 800-nm illumination wavelength measured for different pulse average-power levels. The inset shows linear response versus illumination fluence.

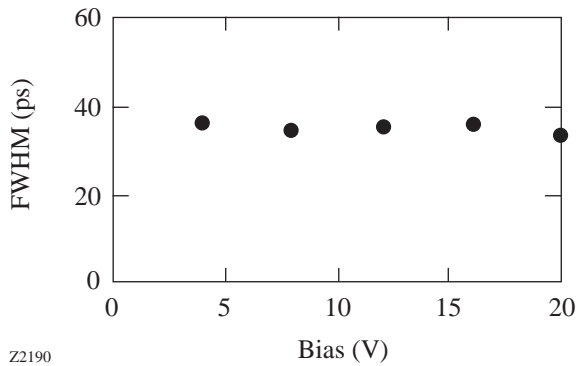


Figure 71.35
The photoresponse FWHM at 800-nm wavelength and 40-nJ/cm² fluence versus the switch bias.

An optical parametric amplifier (OPA) pumped by an 810-nm regenerative amplifier and a white-light continuum system at 1-kHz repetition rate were used to measure the response at 1.55 μm . Since our switch was not processed to improve its subband absorption characteristics, the quantum efficiency of the device in the infrared was less than 10^{-4} . We were able, however, to observe a response at 1.55 μm (Fig. 71.36), which was again a switch-limited signal of 36-ps full-width at half-maximum (FWHM). This result indicates that with suitable efficiency improvement, a high-speed, monolithic, all-silicon, optoelectronic integrated circuit is feasible, using, for example, porous silicon⁶ as the transmitter and a type of polySi material for the detector.

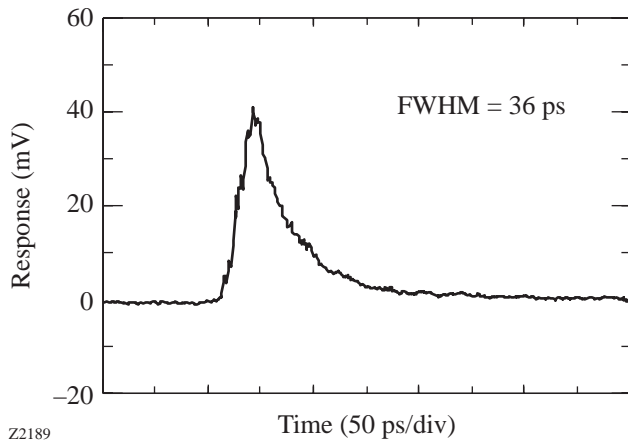


Figure 71.36
The photoresponse at 1.55- μm illumination wavelength. The quantum efficiency was less than 10^{-4} .

Our switch configuration was not designed for EO measurements.⁵ Nevertheless, we managed to get preliminary results by connecting the switch as a meander-type slot line. The signal was generated and measured entirely on the face of the switch structure. It propagated in a meander line fashion along the gap from one end of the switch to the other. The transient measured before entering the first bend is shown in Fig. 71.37. We note a subpicosecond (system-limited) rise time, followed by a decay with an initial fall time of approximately 3 ps.

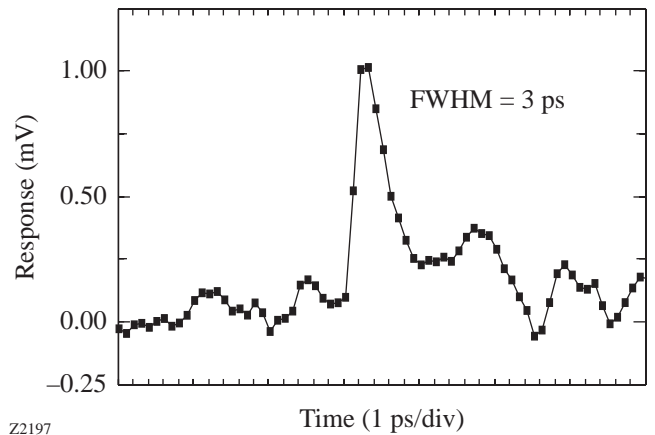


Figure 71.37
Electro-optically measured signal from a polySi switch connected as a meander-type slot line.

Conclusions

A standard fabrication technique was implemented to design small-grain polySi photoconductive switches fully compatible with Si VLSI processing. By means of EO sampling, a material photoresponse of 3-ps FWHM was observed. The switch responded to 800 nm and 1.55- μm femtosecond laser illumination with switch-geometry-limited photocurrent pulses shorter than 40-ps FWHM. The far-infrared response time was generated in nonimplanted silicon with ohmic-like metal-semiconductor contacts, indicating the response was limited by the relaxation time of the extended-state (free) carriers into localized (nonmobile) states. Our preliminary measurements of response time and efficiency can be optimized using simple process changes such as annealing at moderate temperatures, sputter-etching for surface damage, or Fe and Au deep-level defect doping, while still allowing the switch to be integrated with Si IC's.

ACKNOWLEDGMENT

This work was supported by the U. S. Department of Energy Office of Inertial Confinement Fusion under Cooperative Agreement No. DE-FC03-92SF19460 and the University of Rochester. The support of DOE does not

constitute an endorsement by DOE of the views expressed in this article. The author also acknowledges the support of the Frank Horton Graduate Fellowship Program. Additional support was provided by NSF Grant ECS-9413989.

REFERENCES

1. M. D. Skeldon, A. Okishev, S. A. Letzring, W. R. Donaldson, K. Green, W. Seka, and L. Fuller, in *Optically Activated Switching IV*, edited by W. R. Donaldson (SPIE, Bellingham, WA, 1994), Vol. 2343, pp. 94–98.
2. K. Green, W. R. Donaldson, R. Sobolewski, A. Okishev, M. D. Skeldon, S. A. Letzring, and W. Seka, in *First Annual International Conference on Solid State Lasers for Application to Inertial Confinement Fusion*, edited by M. André and H. T. Powell (SPIE, Bellingham, WA, 1995), Vol. 2633, pp. 615–621.
3. D. H. Auston *et al.*, *Appl. Phys. Lett.* **36**, 66 (1980).
4. R. B. Hammond and N. M. Johnson, *J. Appl. Phys.* **59**, 3155 (1986).
5. S. Alexandrou, R. Sobolewski, and T. Y. Hsiang, *IEEE J. Quantum Electron.* **28**, 2325 (1992).
6. K. D. Hirschman, L. Tsybeskov, S. P. Duttagupta, and P. M. Fauchet, *Nature* **384**, 338 (1996).

Thermal Distortions in Laser-Diode– and Flash-Lamp–Pumped Nd:YLF Laser Rods

Laser-diode pumping of solid-state laser materials is proving to be much more advantageous over the more conventional technique of flash-lamp pumping. The electrical to optical efficiency of laser diodes is significantly higher than for flash lamps. In addition, the emission wavelength of laser diodes can be chosen to couple efficiently to the absorption band of the laser ion, resulting in very high overall laser efficiencies. Despite this level of efficiency, both laser-diode– and flash-lamp–pumped systems deposit unwanted heat into the gain medium. The resultant thermal loading of the gain medium leads to thermal-optical wavefront distortions that can degrade the performance of a laser system. Exact eigenmode solutions of optical resonators with phase-aberrating elements can be numerically calculated using high-speed computers. These calculations require a detailed knowledge of the wavefront distortions induced by optical pumping in order to design compensating optics for the system. This is especially important when designing a high-average-power laser system.

A practical constraint for large Nd:glass master oscillator power amplifier (MOPA) laser systems, such as those for laser fusion, is that the laser oscillator must be wavelength matched to the Nd:phosphate-glass amplifiers (gain peak at 1053 nm).¹ A convenient laser crystal with this property is Nd:YLF. A Nd:YLF crystal is naturally birefringent and exhibits gain at 1053 nm for radiation polarized with the electric field perpendicular to the crystalline c axis (σ -polarization state) and exhibits gain at 1047 nm for radiation polarized with the electric field parallel to the crystalline c axis (π -polarization state). This crystal has many other features that make it desirable for other applications, but these will not be elaborated on here.

Thermal-lensing measurements on a Nd:YLF laser rod were first performed by Murray² using pulsed excitation at a fixed input energy. The measurements were made by passing a beam through the rod followed by a lens and a movable pinhole (a standard technique for measuring isotropic crystals). Detailed measurements were later made by Vanherzeele^{3–5}

with a different technique showing strong thermal astigmatism as well as thermal lensing. Astigmatism was measured by using a slit (as opposed to a pinhole) oriented parallel and perpendicular to the crystal c axis. This gives two thermal-focal-length measurements for each polarization state (σ and π): one focal length for a narrow slit of rays oriented parallel to the crystal c axis and one for a narrow slit of rays oriented perpendicular to the crystal c axis. Vanherzeele shows how these thermal distortions, which can adversely affect the performance of a laser system, can be effectively eliminated by proper choice of compensating optics and by the use of a dual-laser-rod system. Further thermal-lensing measurements were made by Reed and Frangineas⁶ who give the rod thermal-focal lengths at a fixed input power both parallel and perpendicular to the c axis for σ - and π -polarization states. Later Cerullo *et al.*⁷ provided additional thermal-lensing data taken as a function of their krypton-flash-lamp electrical-pumping power. In the above experiments, krypton flash lamps were used as excitation sources for all measurements with the exception of the work by Murray, who used xenon flash lamps.

In this article we describe detailed interferometric measurements of the thermal distortions in two Nd:YLF laser rods. One rod is pumped with a xenon flash lamp and the other with laser diodes. Each rod is pumped to the same small-signal gain to compare its distortions under similar laser-operating conditions. We characterize these thermal distortions in terms of a set of primary aberrations of defocus, astigmatism, coma, and spherical. We show that defocus and astigmatism are the dominant aberrations. We interpret our interferometric measurements in terms of the conventional thermal-focal lengths parallel and perpendicular to the c axis of the crystal for both polarization states. We compare the thermal-focal lengths measured with our xenon-flash-lamp– and laser-diode–pumped rods when pumped to the same small-signal gain. We calculate effective dioptric-power coefficients from our data to compare to those reported in the literature for krypton-flash-lamp pumping. We also directly measure the thermal relaxation of these thermal distortions with time for our laser-diode–pumped rod.

We believe that our measurements comparing flash-lamp to laser-diode pumping, as well as our thermal relaxation measurements, are the first measurements of this kind.

Experimental Setup

To measure the thermal distortions in our flash-lamp- and laser-diode-pumped Nd:YLF laser rods, the rods were separately placed in one arm of a Mach-Zehnder interferometer as shown in Fig. 71.38. The laser source for the interferometer was a Nd:YLF cw-mode-locked laser operating at a 1053-nm wavelength (this laser was chosen for convenience). The detection system (CCD camera) integrated over many milliseconds and, hence, could not resolve individual pulses in the mode-locked pulse train. The path lengths of the two interferometer arms were carefully adjusted to be approximately equal in order to produce high-contrast fringes. Wedge was introduced in the interferometer by adjusting the mirrors to provide approximately 40 fringes of tilt. To analyze the fringes, the rod was imaged onto a CCD camera with a lens placed outside the interferometer. The images of the high-contrast fringes from the camera were digitized with a computer equipped with a frame-grabber board. The camera was spectrally filtered with appropriate blocking filters to pass only the 1053-nm radiation of the interferometer laser source. The gain at the 1053-nm wavelength provided by the rod being tested did not significantly degrade the fringe contrast. Fluorescence from the pumped rod was effectively blocked with an aperture placed in the rod arm of the interferometer approximately 50 cm from the rod. The aperture diameter was adjusted to limit the angular field of view of the camera-collection optics while not introducing additional aberrations. The laser used for the interferometer was linearly polarized, and the rod was placed between two half-wave plates (HWP). The laser rods were fabricated with the crystalline a axis along the length of the rod and were placed in the interferometer with the a axis parallel to the interferometer optical axis. The crystalline c axis for

both the laser-diode and flash-lamp systems was therefore perpendicular to the interferometer optical axis and located in the plane of the rod end face. The interferometer laser polarization through the rod could be adjusted perpendicular to the c axis (σ) or parallel to the c axis (π) of the rod by adjusting the half-wave plate before the rod. The half-wave plate after the rod was used to realign the laser polarization state parallel to the interferometer reference arm for maximum fringe contrast on the camera. Fringes were captured by the computer and analyzed.

The digitized fringe patterns were transformed into wavefronts using a spatial-synchronous phase-detection technique.⁸⁻¹⁰ The high-frequency interferogram was captured by the frame grabber, stored in memory, and then Fourier analyzed to obtain the amplitude and phase of the two-dimensional wavefront exiting the laser rod. Fringe data were analyzed over only a portion of the rod's clear aperture (approximately 90% of the rod diameter) to obtain the wavefront distortions. To accomplish this, a circular software aperture centered on the rod was placed over the rod image. Only the fringe data within this aperture were used in the analysis. To calibrate the fraction of the rod aperture used in the analysis, a reticle was placed at the equivalent rod position in the opposite interferometer arm, imaged to the camera with the lens outside the interferometer, and overlapped in software with the image of the rod and the software aperture used for fringe analysis. A background wavefront was taken for each rod with no pumping (but with the simmer on for the flash-lamp data) and subtracted from all other wavefronts. The background-subtracted wavefronts of the pumped rods were then analyzed to determine the number of waves of defocus, astigmatism, spherical, and coma produced by pumping. The overall accuracy of this fringe analysis technique is believed to be $<\lambda/50$ (<0.02 waves). To calibrate this interferometric-measurement system, the focal length of a 1-m lens was measured with an accuracy of greater than 99%.

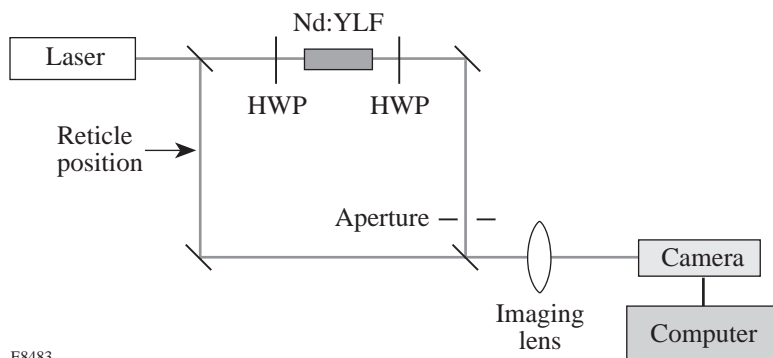


Figure 71.38
Experimental setup for measuring the pump-induced wavefront distortions in Nd:YLF laser rods.

E8483

The thermal-time constant of our laser-diode-pumped Nd:YLF rod was also measured with the above equipment. The fringes were recorded on tape with a video camera recorder (VCR) as the rod pumping was turned off (and the liquid cooling left on). A frame sequencer was used to number the individual frames from the camera. By replaying the video tape through the computer, sequential data frames could be captured and analyzed. In this way, the aberrations could be measured at 60 frames (data points) per second.

The flash-lamp system had a 4-mm-diam \times 54-mm-long Nd:YLF laser rod pumped with a single 4-mm bore \times 24-mm-arc-length xenon flash lamp. The flash lamp was simmered with approximately a 400-V drop across the lamp and 50 mA of simmer current. The pulse-forming network for the lamp used a 150- μ f capacitor charged to 385 V (i.e., 11 J per pulse). The lamp's current pulse was approximately Gaussian with a pulse width of 250 μ s (FWHM). A small-signal gain of 1.8 at 1053 nm was measured in the Nd:YLF rod with these conditions (sufficient to operate the regenerative amplifier for our application). The system was operated to 60 pulses per second. Fringes within a 3.4-mm-diam software aperture centered on the rod were used to analyze this rod.

The laser-diode-pumped system, including the diode arrays, was designed and built by the McDonnell-Douglas Electronic Systems Company (no longer a part of McDonnell-Douglas) and is similar in performance (although operating at a different wavelength) to the one reported in Ref. 11. The system had a 5-mm-diam \times 54-mm-long Nd:YLF laser rod pumped with three banks of laser diodes along the length of the rod. Each bank consisted of 16 diode bars arranged symmetrically around the circumference of the rod for a total of 48 diode bars arranged around the rod. The length of the rod pumped with this diode arrangement was 34 mm. The laser diodes had their polarization states parallel to the a axis of the crystal and hence perpendicular to the c axis. The diode emission wavelengths were centered around the 797-nm absorption peak of Nd:YLF. The absorption coefficient of Nd:YLF for this case is approximately 3 cm^{-1} . The pulse-forming network produced a 250- μ s-wide, 50-A square current pulse with approximately 100 V applied across the diode bars connected in series. With these conditions each diode bar emitted approximately 45 W of peak optical power (2.16-kW peak array optical power) for an optical-output-to-electrical-input diode-array efficiency of greater than 40%. A small-signal gain of 1.8 at 1053 nm was measured in the rod under these conditions. If we assume a stimulated emission cross section of $1.2 \times 10^{-19} \text{ cm}^2$ for this

transition,¹² the stored energy in the rod was 0.18 J, resulting in an optical-pumping efficiency (stored energy to diode-array output-optical-energy) of approximately 33%. This system was operated to 200 pulses per second. Fringes within a 4.4-mm-diam software aperture centered on the rod were used to analyze this rod.

Interpretation of Interferometric Data

When the Nd:YLF laser rod is unpumped, the wavefront distortion measured in transmission through the rod by the interferometer gives the amount of static aberration in the rod due to internal crystal strain. This wavefront is stored and is the background wavefront that is subtracted from all other measured wavefronts. The background-subtracted wavefronts measured with optical pumping, therefore, provide detailed information of the thermally induced refractive-index changes in the pumped laser rods. The distorted wavefronts exiting the thermally loaded laser rods are quantified in lowest order (using the third-order aberration theory¹³) by the linear superposition of a set of primary aberrations of defocus, astigmatism, coma, and spherical, which are defined below.

The thermally distorted wavefront exiting the rod can be expressed as a surface of constant phase:

$$\Phi_{\text{total}}(\rho, \theta) = \Phi_{\text{def}}(\rho) + \Phi_{\text{ast}}(\rho, \theta) + \Phi_{\text{coma}}(\rho, \theta) + \Phi_{\text{sph}}(\rho), \quad (1)$$

where the surface of constant phase for each of the primary aberrations is given by

$$\Phi_{\text{def}} = \lambda \Delta_{\text{def}} \rho^2, \quad (2a)$$

$$\Phi_{\text{ast}} = -\frac{\lambda \Delta_{\text{ast}}}{2} \rho^2 \cos(2\theta), \quad (2b)$$

$$\Phi_{\text{coma}} = -\lambda \Delta_{\text{coma}} (\rho^3 - \rho) \cos(\theta), \quad (2c)$$

$$\Phi_{\text{sph}} = \lambda \Delta_{\text{sph}} (\rho^4 - \rho^2), \quad (2d)$$

with $\rho = r/r_0$ the normalized radius r within the rod aperture, r_0 is the radius of the rod clear aperture used in the analysis ($r_0 = 1.7 \text{ mm}$ for the flash-lamp-pumped rod and $r_0 = 2.2 \text{ mm}$ for the laser-diode-pumped rod), θ is the polar angle in the rod

aperture measured from the c axis of the crystal, λ is the interferometer wavelength (1053 nm), and the Δ_i 's are the number of waves of the primary aberration measured (i.e., the weighting factors in the linear superposition).

We show experimentally that the dominant thermal aberrations are defocus and astigmatism (discussed in the next section). Both defocus and astigmatism have a quadratic dependence on the aperture coordinate r , and from these a focal length can be defined for two orthogonal planes. If we neglect the aberrations of coma and spherical, then we can define a focal length for the two orthogonal planes that contain the a axis (optical axis) of the crystal. (The plane containing the a and c crystal axes with $\theta = 0$ is referred to as $\parallel c$, and the plane containing the a and b crystal axes with $\theta = \pi/2$ is referred to as $\perp c$.) The wave fronts (surfaces of constant phase) associated with defocus and astigmatism are shown in Fig. 71.39. Pure defocus [Fig. 71.39(a)] is seen to be a spherical wavefront with equal curvatures in all directions (i.e., $0 \leq \theta < 2\pi$). Pure astigmatism [Fig. 71.39(b)] is seen to be a wavefront with curvatures of equal magnitude but opposite sign in two orthogonal directions (i.e., $\theta = 0$ and $\theta = \pi/2$). The thermal-focal length in a given plane is easily calculated from the number of waves of defocus and astigmatism and is given by (using a small angle approximation)

$$f_{\pm} = \frac{r_0^2}{2\lambda(\Delta_{\text{def}} \pm \Delta_{\text{ast}}/2)}, \quad (3)$$

where f_+ is the focal length in the plane perpendicular to the crystal c axis ($\theta = \pi/2$ or $\perp c$) and f_- is the focal length in the plane parallel to the crystal c axis ($\theta = 0$ or $\parallel c$).

Astigmatism and coma are odd aberrations and have an angle of symmetry associated with them. The wavefront analysis program calculates this symmetry angle for these aberrations, and our measurements show that these symmetry axes are aligned perpendicular and parallel to the c axis of the crystal as implied by Eqs. (2)—an expected result but previously unmeasured. The definitions and conventions discussed here were used to analyze our data.

Thermal-Distortion Measurements

We assume that the laser-diode- and flash-lamp-pumped rods are uniformly pumped so that heat is generated uniformly throughout the rod volume. Since the time between pump pulses is short (0.2 s for the lowest pulse-repetition rate used: 5 Hz) compared to the thermal-relaxation time of the rod (1.5 s; see Fig. 71.45 discussed later), pumping can be considered continuous and the temperature distribution in the rod will reach steady state after a brief warm-up period. The rods were liquid cooled, and in steady state the surface temperature of the rod will be constant for a particular pump power. A long cylindrical laser rod pumped with the above assumptions will produce a quadratic radial temperature and strain distribution that will lead to a quadratic radial index-of-refraction profile in the rod.¹² Since Nd:YLF is a uniaxial crystal, the quadratic radial profile will be different in two orthogonal directions.

Figure 71.40 shows the measured aberrations as a function of the pump repetition rate for the case of the laser-diode-pumped laser rod using π -polarized light in the rod (gain at $\lambda = 1047$ nm). Figure 71.41 shows the same measurements using σ -polarized light in the rod (gain at $\lambda = 1053$ nm). In these figures, the data points for defocus and astigmatism are fit to a straight line, while the data points for coma and spherical are

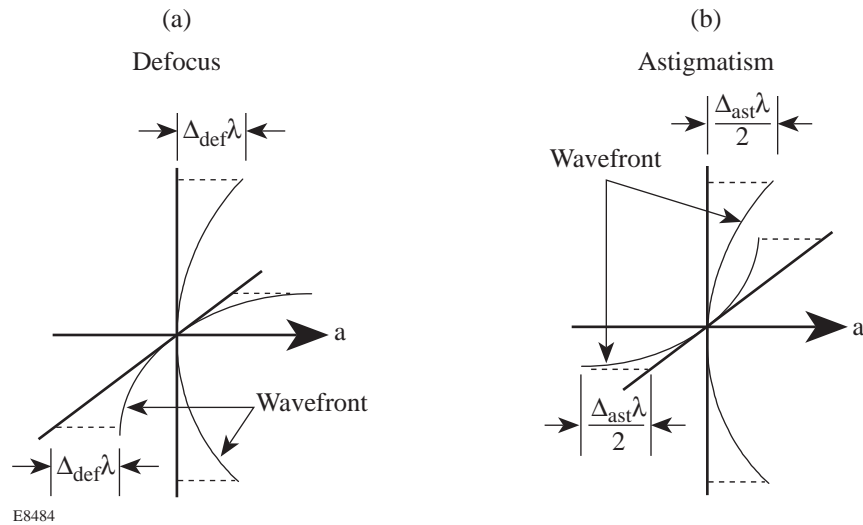
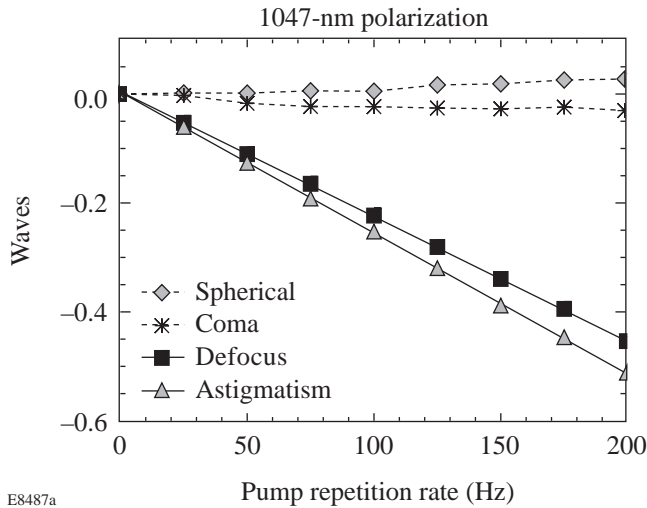


Figure 71.39 Surfaces of constant phase (wavefront shown with thin lines) for (a) pure defocus and (b) pure astigmatism as defined and used in our analysis. Here λ is the wavelength of the interferometer source (1053 nm), Δ_{def} is the number of waves of defocus measured, and Δ_{ast} is the number of waves of astigmatism measured.

E8484

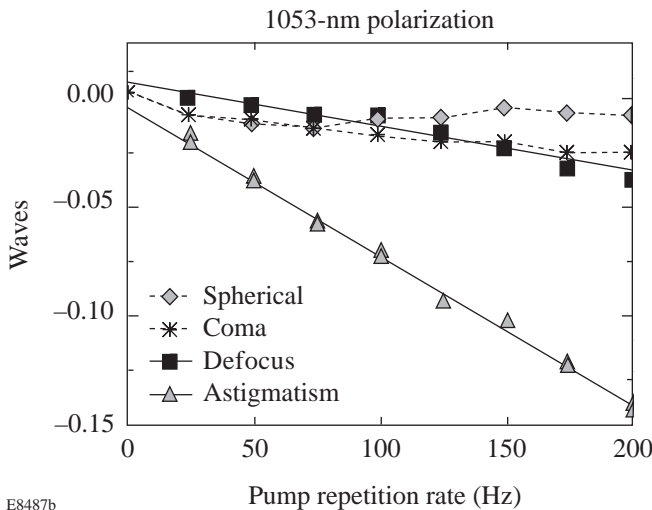
connected by dashed lines. It can be seen from these data that although a small amount of coma and spherical aberration was measured, defocus and astigmatism are the dominant aberrations. Coma and spherical will henceforth be neglected from our analysis. Thermal-focal lengths can be calculated from this data using Eq. (3) with $r_0 = 2.2$ mm (the radius of the rod

aperture used to analyze the fringe data). Figure 71.42 shows the thermally induced dioptric powers (defined as one divided by the thermal-focal length in meters) for the case of the laser-diode-pumped laser rod using π -polarized light in the rod (gain at $\lambda = 1047$ nm), and Fig. 71.43 shows the same data using σ -polarized light in the rod (gain at $\lambda = 1053$ nm). Again the data are fit to straight lines. In these figures, two dioptric powers are given corresponding to the planes parallel and perpendicular to the crystal c axis as described above.



E8487a

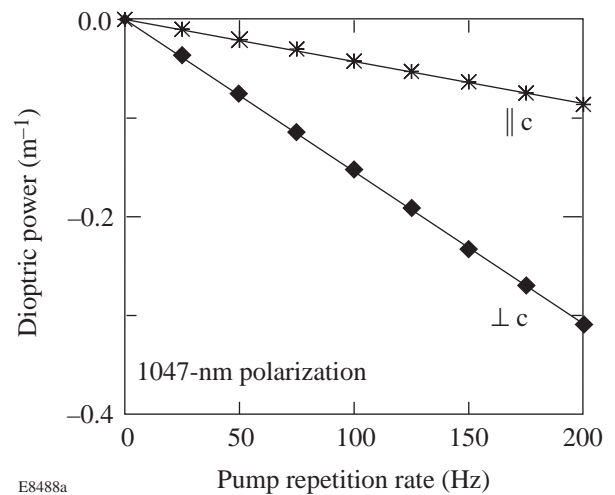
Figure 71.40 Waves of aberration measured with π -polarized light (corresponding to gain at 1047 nm) as a function of the pump repetition rate for our laser-diode-pumped Nd:YLF laser rod pumped to a small-signal gain of 1.8 at 1053 nm.



E8487b

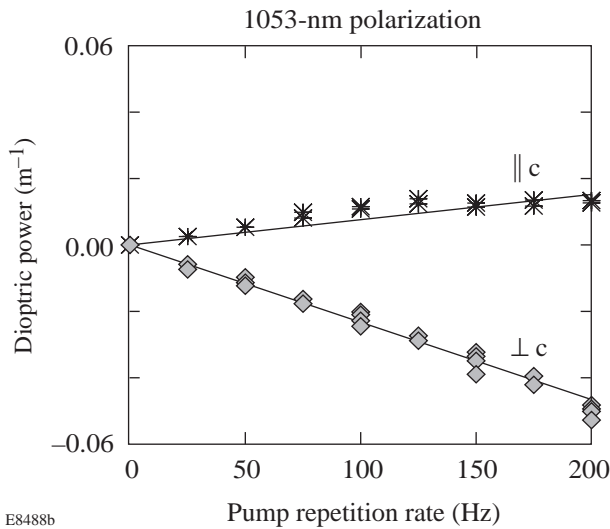
Figure 71.41 Waves of aberration measured with σ -polarized light (corresponding to gain at 1053 nm) as a function of the pump repetition rate for our laser-diode-pumped Nd:YLF laser rod pumped to a small-signal gain of 1.8 at 1053 nm.

For the case of the xenon-flash-lamp-pumped system the thermally induced aberrations using σ -polarized light in the rod (gain at $\lambda = 1053$ nm) were too small to measure since the repetition rate of the flash-lamp power supply was limited to 60 Hz. Figure 71.44 shows the thermally induced dioptric powers (with straight line fits) for the case of the xenon-flash-lamp-pumped laser rod (dashed lines) using π -polarized light in the rod (gain at $\lambda = 1047$ nm). For comparison we have also shown in Fig. 71.44 the same data for the laser-diode-pumped system (taken from Fig. 71.40 and plotted with solid lines). All data in Figs. 71.40–71.44 are taken for the rod pumped to the same small-signal gain (1.8 at 1053 nm). It can be seen that the xenon-flash-lamp-pumped system shows more thermal distortion than the laser-diode-pumped system when pumped to the same small-signal gain.



E8488a

Figure 71.42 Dioptric power (inverse of the thermal-focal length in meters) calculated from the data in Fig. 71.40 as a function of the pump repetition rate. The dioptric power for the plane containing the optic axis (crystal a axis) and the crystal c axis is labeled $\parallel c$ and for the plane containing the optic axis and the crystal b axis is labeled $\perp c$.



E8488b

Figure 71.43

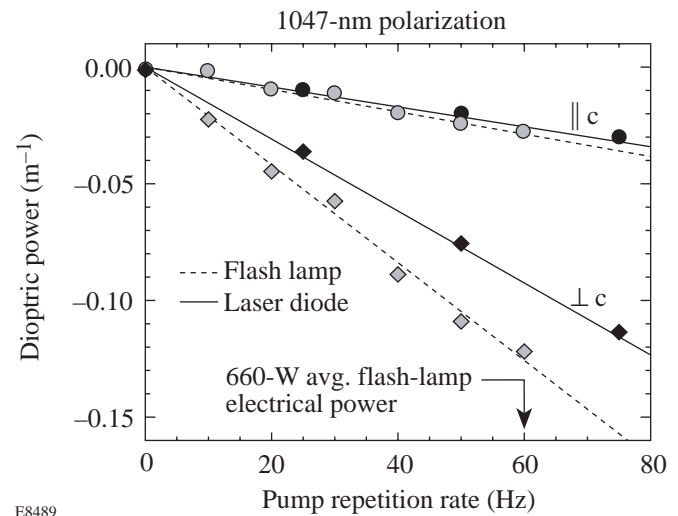
Dioptric power (inverse of the thermal-focal length in meters) calculated from the data in Fig. 71.41 as a function of the pump repetition rate. The dioptric power is labeled $\parallel c$ for the plane containing the optic axis (crystal a axis) and the crystal c axis and $\perp c$ for the plane containing the optic axis and the crystal b axis.

The dioptric powers in Figs. 71.42–71.44 can be written for the two orthogonal planes as¹²

$$D_{\perp,\parallel} = k_{\perp,\parallel} P_a/A, \quad (4)$$

where $D_{\perp,\parallel}$ are the dioptric powers in the planes perpendicular and parallel to the c axis, P_a is the total heat dissipated by the rod (equivalent in steady state to the total heat absorbed by the rod), A is the rod cross-sectional area, and the $k_{\perp,\parallel}$ are the dioptric-power coefficients defined in terms of the material parameters of Nd:YLF.

The heat dissipated by the rod was not measured; however, to compare our dioptric-power measurements to those stated in the literature, we will make similar assumptions: We assume that the total heat dissipated by the rod is proportional to the average electrical power dissipated in the flash lamps, where the proportionality constant involves many coupling efficiencies. We redefine the dioptric-power coefficients in Eq. (4) to include this proportionality constant. We can then calculate these newly defined dioptric-power coefficients using our dioptric-power measurements and the average electrical power dissipated in our xenon flash lamp. When our xenon



E8489

Figure 71.44

Comparison of the dioptric powers (inverse of the thermal-focal length in meters) as a function of the pump repetition rate measured for xenon-flash-lamp-pumped- and laser-diode-pumped Nd:YLF laser rods pumped to the same small-signal gain. The data have been fit to straight lines with the xenon-flash-lamp-pumped data shown as dashed lines and the laser-diode-pumped data (taken from Fig. 71.42) shown as solid lines.

flash lamp is operated at 60 Hz with 11 J per pulse, the average electrical power dissipated in the lamp is 660 W. This calibrates the axes in Figs. 71.42–71.44 to lamp average electrical power, and we can then state dioptric-power coefficients accordingly. Table 71.VII summarizes our dioptric-power coefficients $k_{\perp,\parallel}$, defined in this way, using the appropriate values for the rod areas.

It is coincidental that our dioptric-power measurements for our laser-diode-pumped rod are very similar to those reported by Cerullo *et al.*⁷ for their krypton-flash-lamp-pumped rod. It would be inappropriate, however, to base any conclusions on this since among other things the rods have different diameters and the coupling efficiencies are very different for the two cases. In fact, a true comparison of these data should include a detailed analysis of the cooling and coupling efficiencies mentioned above for each case, since the heat dissipated by the rod is the appropriate quantity to use in Eq. (4). This analysis would go far beyond the intent of this article.

The distortions in the xenon-flash-lamp-pumped rod were also measured at a higher gain. The capacitor-bank voltage was increased from 385 V to 460 V, corresponding to a 43% increase in pump-pulse energy from 11 J per pulse to

Table 71.VII: The coefficients of the thermal-dioptic power as defined in Eq. (4) and discussed in the text.

λ (nm)	Laser diode k_{\parallel} (mm/kW)	Laser diode k_{\perp} (mm/kW)	Xenon flash lamp k_{\parallel} (mm/kW)	Xenon flash lamp k_{\perp} (mm/kW)
1047	-0.767×10^{-3}	-2.76×10^{-3}	-0.565×10^{-3}	-2.38×10^{-3}
1053	-0.566×10^{-3}	$+0.153 \times 10^{-3}$	no data	no data

16 J per pulse. We found that the measured thermal distortions scaled linearly with this corresponding increase in average pump power as expected from Eq. (4). However, if the pump-pulse energy were increased significantly beyond this, the lamp’s spectral output would change and different results would be expected.

The thermal-time constant of the distortions in our laser-diode-pumped rod was measured with the camera and VCR frame sequencer as described above. The data are shown in Fig. 71.45. The thermal distortions were measured using π -polarized light (gain at $\lambda = 1047$ nm) in our laser-diode rod pumped at a 200-Hz repetition rate as in Fig. 71.40. Pumping was removed at time equals zero in Fig. 71.45 (with the cooling liquid left on), and the thermal distortions were measured thereafter at known intervals (determined from the frame sequence numbers of the fringe data). The data points for defocus and astigmatism were fitted to exponential curves

(shown as solid lines in Fig. 71.45), and an exponential decay time constant (time for the aberrations to decay to $1/e$ of their value when pumping was removed) of approximately 1.5 s was obtained. These measurements were also made with the 1053-nm transition, and no significant change in the thermal-time constant could be measured.

Summary

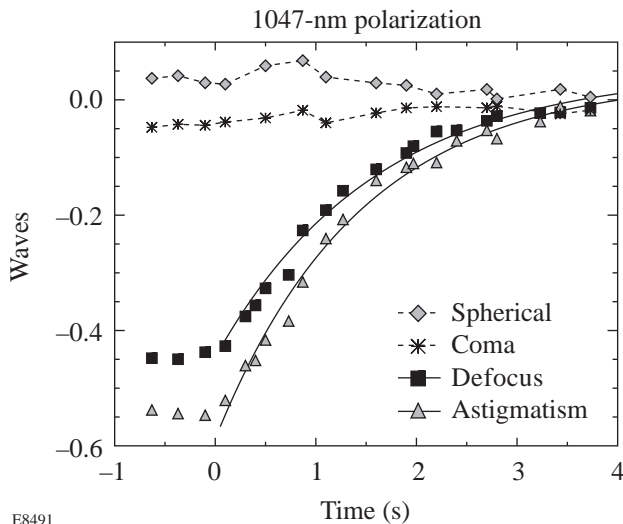
We have made detailed interferometric measurements of the thermal distortions in xenon-flash-lamp- and laser-diode-pumped Nd:YLF laser rods. In both cases, defocus and astigmatism were the dominant thermal distortions. The thermal distortions in our flash-lamp-pumped rod were greater than the thermal distortions in our laser-diode-pumped rod when pumped to the same small-signal gain. Finally, we measured the thermal-relaxation time of our laser-diode-pumped Nd:YLF rod to be approximately 1.5 s.

ACKNOWLEDGMENT

This work was supported by the U.S. Department of Energy Office of Inertial Confinement Fusion under Cooperative Agreement No. DE-FC03-92SF19460, the University of Rochester, and the New York State Energy Research and Development Authority. The support of DOE does not constitute an endorsement by DOE of the views expressed in this article.

REFERENCES

1. Laboratory for Laser Energetics LLE Review **70**, 68, NTIS document No. DOE/SF/19460-164 (1997). Copies may be obtained from the National Technical Information Service, Springfield, VA 22161.
2. J. E. Murray, IEEE J. Quantum Electron. **QE-19**, 488 (1983).
3. H. Vanherzeele, Opt. Lett. **13**, 369 (1988).
4. H. Vanherzeele, Appl. Opt. **27**, 3608 (1988).
5. H. Vanherzeele, Appl. Opt. **28**, 4042 (1989).
6. E. Reed and G. Frangineas, in *Solid State Lasers*, edited by G. Dubé (SPIE, Bellingham, WA, 1990), Vol. 1223, pp. 247–258.
7. G. Cerullo, S. De Silvestri, and V. Magni, Opt. Commun. **93**, 77 (1992).
8. Y. Ichioka and M. Inuiya, Appl. Opt. **11**, 1507 (1972).
9. M. Takeda, H. Ina, and S. Kobayashi, J. Opt. Soc. Am. **72**, 156 (1982).



E8491

Figure 71.45 Thermal relaxation of the aberrations for π -polarized light (corresponding to gain at 1047 nm) in the laser-diode-pumped Nd:YLF laser rod. The rod was operated at 200-Hz pump repetition rate, and pumping was removed at time equals zero. The thermal-relaxation time is 1.5 s.

10. K. H. Womack, *Opt. Eng.* **23**, 391 (1984).
11. L. E. Holder *et al.*, *IEEE J. Quantum Electron.* **28**, 986 (1992).
12. W. Koechner, *Solid-State Laser Engineering*, 3rd ed., Springer Series in Optical Sciences (Springer-Verlag, New York, 1996).
13. M. Born and E. Wolf, *Principles of Optics: Electromagnetic Theory of Propagation, Interference and Diffraction of Light*, 6th ed. (Pergamon Press, Oxford, 1980).

The OMEGA Target-Positioning System

System Overview

Historically, several different styles of target positioners have been developed and deployed at LLE. The initial target positioner on the OMEGA 24-beam system used a 16-target carousel, which was located inside the experimental target chamber. This approach required that the entire target chamber be vented to load the target carousel; it further constrained the experimental operations by limiting target selection to one of the 16 on the carousel. This last constraint often limited the flexibility of the experimental program to change the target parameters during the shot sequence based on the results from the initial shots in the sequence. In addition, this carousel positioner did not allow rotational alignment of the target, which is required for flat-target experiments.

In the mid-1980s, a new style of target positioner was developed to support initial x-ray laser shots. It featured six axes of adjustment as well as a gas-feed capability; however, it also required that the entire experimental chamber be vented to load a single target. In addition, the six axes were configured in a manner that required complex compound motions for target alignment.

A third positioner developed for the OMEGA 24-beam system used a shuttle approach to load individual targets without requiring the experimental chamber to be vented. This positioner featured four axes of alignment motion without the complex compound motions of earlier positioners (see Fig. 71.46). Although this positioner was developed as an auxiliary positioner for backlighter targets, it soon became OMEGA's primary target positioner because it was reliable and provided quick turnaround between shots, while it maintained the maximum flexibility for the experimental program by allowing any available target to be used during a shot sequence. This positioner became the basis for the design of the target positioner for the OMEGA 60-beam system.

The OMEGA target-positioning system (TPS) has been developed to provide an accurate method for positioning a

wide variety of targets at the required location at or near the center of the experimental target chamber within the 1-h shot cycle of the OMEGA system. This target positioner provides four alignment motions, which include three translation motions (X , Y , Z) and one rotation motion about the axis of the

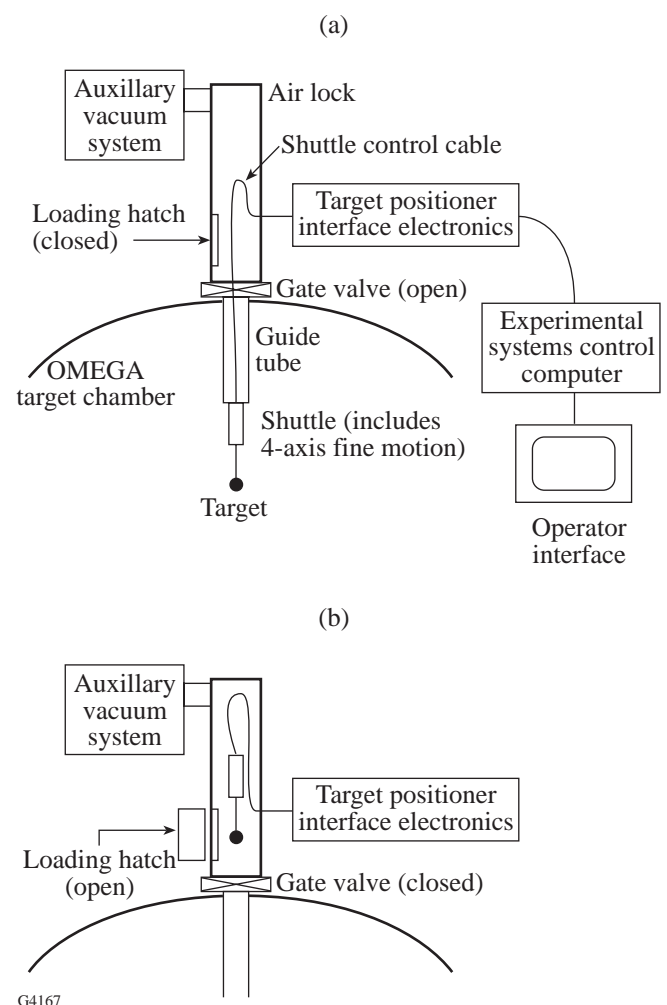
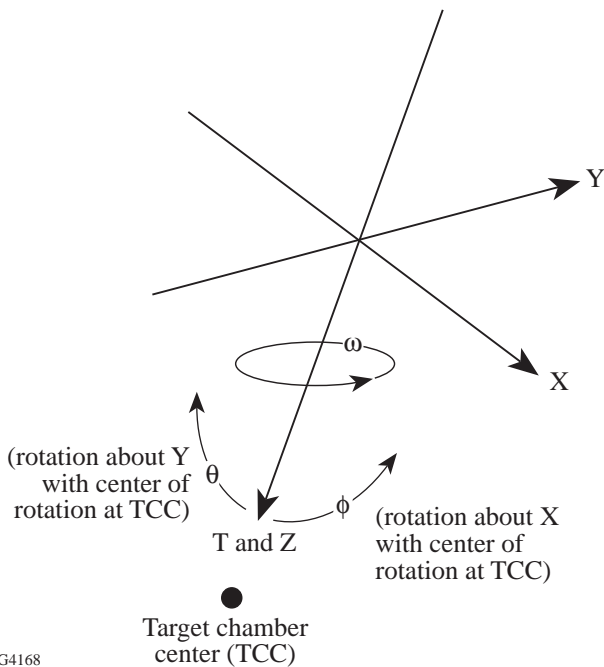


Figure 71.46 Shuttle-type target-positioning system: (a) target extended, (b) target retracted.

positioner (ω), with an option to add the remaining two rotation motions (θ , ϕ). (See Fig. 71.47 for the definitions of these motions.) The motion (T) used to transport the shuttle to the target chamber center (TCC) is independent of the fine alignment motions.

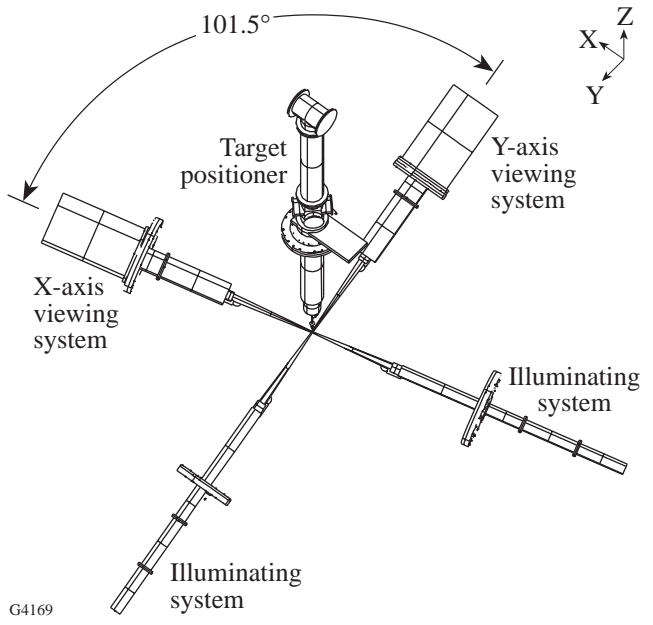


G4168

Figure 71.47
Definition of the OMEGA target-positioner axes.

The definition of TCC is provided by two nearly orthogonal target-viewing systems (TVS), which are rigidly attached to the chamber. The angle between the viewing systems is 101.5° , and the target positioner is 33.2° from being normal to the plane defined by the two viewing systems (see Fig. 71.48). This geometry does introduce coupling between the target-positioner motions and the two viewing systems; however, system operators learn to compensate and readily achieve target alignment.

A typical shot sequence begins with the target chamber evacuated to mid- 10^{-6} Torr; the target positioner is retracted and the air lock vented. A target is manually loaded onto the end of the target positioner, and the air lock is closed and evacuated below 1×10^{-4} Torr. The gate valve is opened, and the target positioner is inserted into the TCC. Once the target is located in the viewing systems, final alignment is done to $\pm 5 \mu\text{m}$ of the designated location using the fine positioning stages in the target positioner. Following the laser shot, the target positioner is retracted, the gate valve is closed, and the air lock is vented so that the process can be repeated.



G4169

Figure 71.48
OMEGA target chamber viewing system geometry. (View: normal to plane of viewing system.)

Requirements and Concept

A draft specification written in mid-1993 served as the basis for the mechanical design of the OMEGA target positioner. This specification was based on a shuttle-style device (Fig. 71.46), which was thought to provide the best combination of short cycle time and flexibility in target selection during an experimental shot sequence. The seven axes of motion are defined in Fig. 71.47, where the T and Z axes are along the axis of the target positioner. Experience has shown that the configuration of these axes (shown in Fig. 71.49) is important to minimize coupling of the motion of each axis. In addition, the θ and ϕ motions should have pivot axes as close as possible to the TCC to minimize the translation of the target when these rotations are adjusted. (The basic requirements of the target positioner specification are summarized in Table 71.VIII.) In addition, the bulk of the target positioner is to be located at least 12 in. from the TCC to minimize the amount of ablation due to the reaction products and energetic debris from the implosion.

The OMEGA target positioner is shown in Fig. 71.50. The target is attached to the fine-motion stages, which are supported on the transfer assembly (see Fig. 71.51); this unit moves within the guide tube assembly to the TCC. The guide tube assembly is the main structural member of the positioner and provides the vacuum housing for the air lock. This assem-

bly is attached to the chamber using a gate valve that allows the air lock to be independently vented. The target positioner currently deployed on OMEGA does not include the θ and ϕ

motions, although these motions are shown in Fig. 71.51. The sections of the target positioner are discussed in detail in the following sections.

Table 71.VIII: Required performance of the OMEGA target positioner.

Parameter	Specification	Comments
Required alignment motions	X, Y, Z, ω	θ and ϕ may be added
$X, Y,$ and Z motion range	1 in.	Target within a 1-in. radius
$X, Y,$ and Z motion resolution	$5 \mu\text{m}$ (0.0002 in.)	Maximum step size
ω range	360°	Continuous
ω resolution	0.25°	Maximum step size
θ and ϕ ranges	$\pm 5^\circ$	Minimum
θ and ϕ resolutions	0.25°	Maximum step size
T resolution	1 mm (0.040 in.)	Maximum step size
Stability over 60 min	Within resolution	For all axes
Maximum target acceleration	0.2 g	For all axes
Transport time	Within 5 min	From airlock to TCC
Orientation	Any port on chamber	

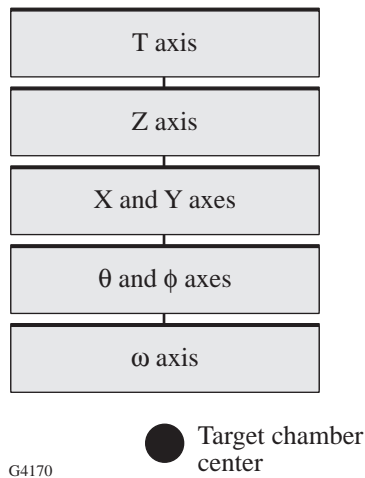


Figure 71.49
Configuration of OMEGA target-positioner axes.

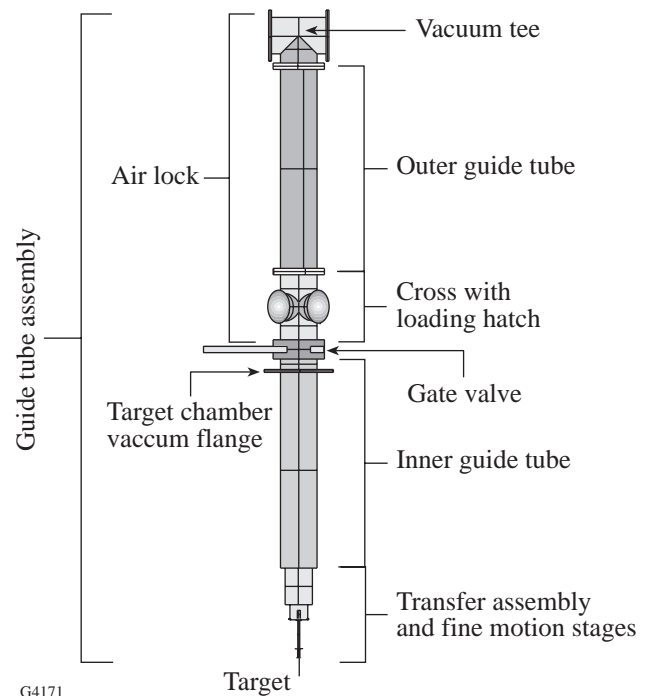
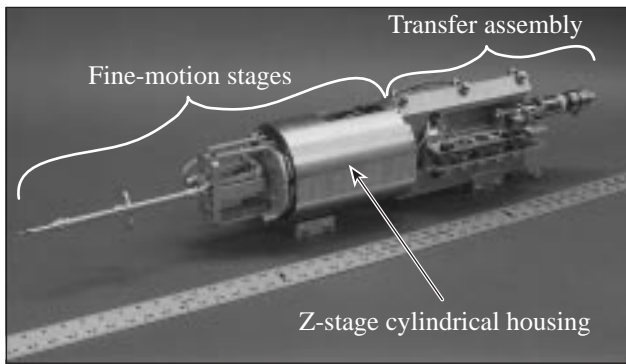


Figure 71.50
OMEGA target-positioner components.



G4172

Figure 71.51
Transfer assembly and fine-motion stages.

Transport Motion

The transport motion transports the target from the target positioner’s air lock to the TCC—a distance of 80 in. This motion is provided by the following subsystems: a guide tube assembly, a transfer assembly, and a cable assembly.

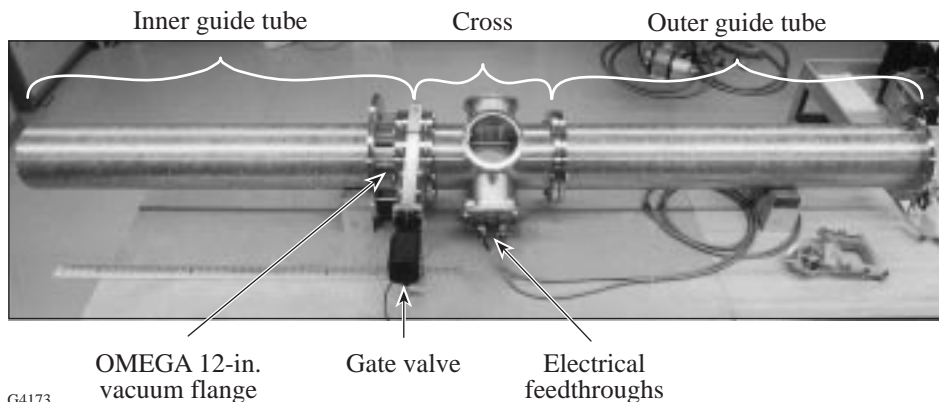
1. Guide Tube Assembly

The guide tube assembly consists of five sections: inner guide tube, gate valve, cross, outer guide tube, and vacuum tee (see Fig. 71.50). The guide tube sections are 8-in.-outer-diam stainless steel tube. The inner guide tube is inside the target chamber and includes a standard 12-in. OMEGA flange, which seals to the target chamber. The cross and outer guide tube make up the air lock for the target positioner when the transfer assembly is withdrawn to load a new target. The gate valve separates the inner and outer guide tubes. Attached to the cross are standard ISO-style electrical-feedthrough vacuum flanges for powering the insertion and fine positioning stages (see Fig. 71.52); a quick access door for manually loading targets; and a viewport. The fourth flange on the cross will be used for an auto target loader, which will be added to the positioner in the future. The vacuum tee terminates the outer end of the guide

tube assembly and provides the interfaces to the roughing and vent valves, the turbo molecular high-vacuum pump, and the high-vacuum valve, which isolates this pump (see Fig. 71.53).

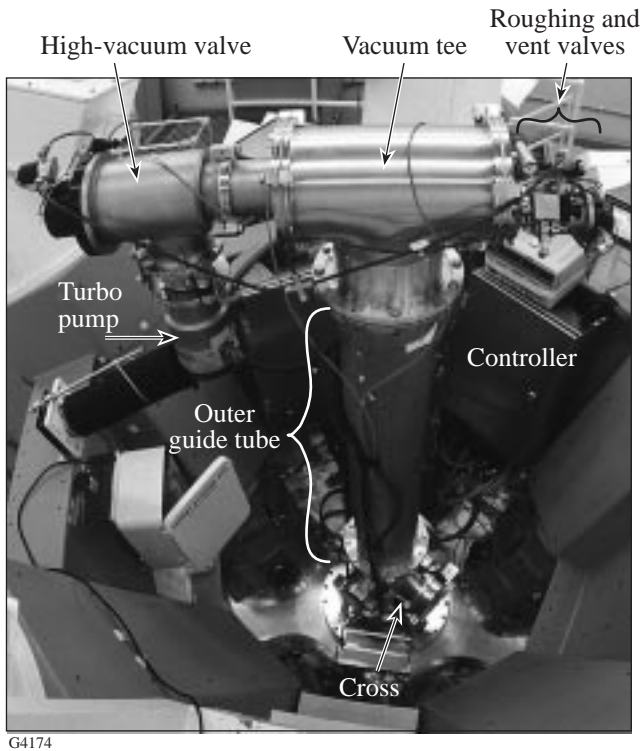
The guide tube assembly provides the structural support for the target positioner. This structure is approximately 94 in. long and is designed to provide the required stability of $\pm 5 \mu\text{m}$ ($\pm 0.0002 \text{ in.}$) at the center of the target chamber. Finite element analysis (FEA) was used to calculate the normal modes of this structure and determine how it would respond to vibration from other equipment attached to the target chamber. This modeling determined that an input of $100 \mu\text{g}$ at the target chamber flange would displace the target by $0.4 \mu\text{m}$ at the first mode of 22 Hz. Modeling determined that adding a support to the vacuum tee increased the first mode to 72 Hz and decreased the forced response to $0.2 \mu\text{m}$. However, in practice, this additional support has not been required on the target positioner currently deployed on OMEGA.

The guide tube assembly supports the cylindrical rails and drive rack for the transport assembly. The double rail design shown in Fig. 71.54(a) was chosen because it is simple and provides adequate straightness of motion. The technique for mounting the rails was taken from the six-inch manipulator (SIM) developed at LLNL and involves cross tapping the rails and using screws from the outside of the guide tube to secure the rail to the inside of the tube. The heads of the screws were then welded to the outside of the guide tube to maintain the vacuum integrity of the guide tube. This technique provided a simple fabrication method and yielded a stiff mounting for the rails after the screws are welded. One of the rails is spaced away from the inside surface of the tube [see Fig. 71.54(b)] to provide the proper clearance for the transport mechanism. The drive rack support is mounted to the inside surface of the guide tube using the same technique. The drive racks in the outer guide tube and the cross can be adjusted axially to allow them to be meshed with the drive rack in the inner guide tube. The



G4173

Figure 71.52
Guide tube assembly. (Note: The vacuum tee is not shown.)



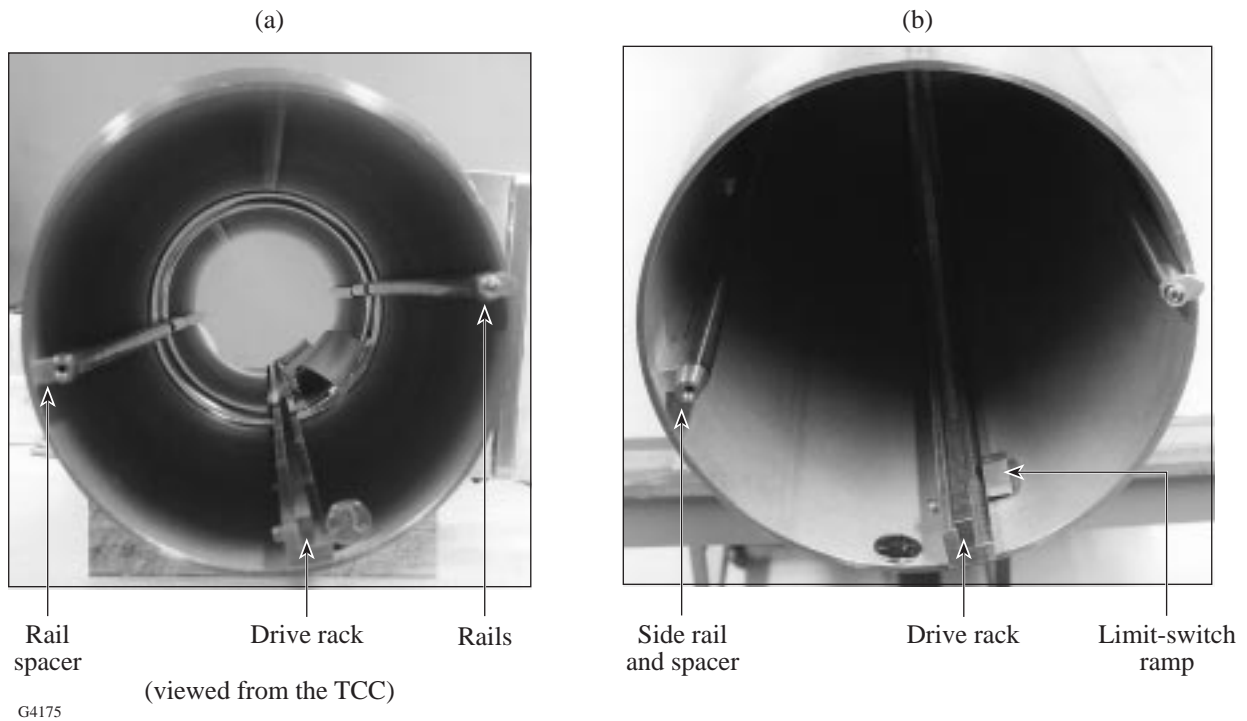
G4174

Figure 71.53
Target positioner on the top port of the OMEGA target chamber.

drive rack has a small gap at the joint between the outer guide tube and the cross and a 2-in. gap across the gate valve. The guide rails also have a 2-in. gap across the gate valve. The transfer assembly is designed to bridge these gaps.

2. Transfer Assembly

The transfer assembly is made up of the transfer body and the gear housing and provides 80 in. of motion inside the guide tube [see Fig. 71.55(a)]. It is constructed with ball-bearing rollers that run on the rails in the guide tube. On one side of the transfer body the rollers form three V's; the opposite side of the transfer body has fixed lower rollers to take the spring preload on the drive gears, and spring-loaded upper and side rollers to prevent binding during the translation in the guide tube [see Fig. 71.55(b)]. Three sets of rollers on each side allow the transfer body to bridge the gap in the rails at the gate valve. The drive motion is provided by a small gear motor driving three drive gears through a worm gear reducer [see Fig. 71.55(c)]. The gear housing deployed with the current target positioner uses two drive gears rather than the three gears shown in Fig. 71.55(c). The two drive gears are separated by a distance that allows the unit to bridge the gap at the gate valve. The three drive gears are used to improve the smoothness of the motion across the gap in the drive rack at the gate valve.



G4175

(viewed from the TCC)

Figure 71.54
(a) End view of the guide tube rails and drive rack; (b) closeup of the guide tube rails and drive rack.

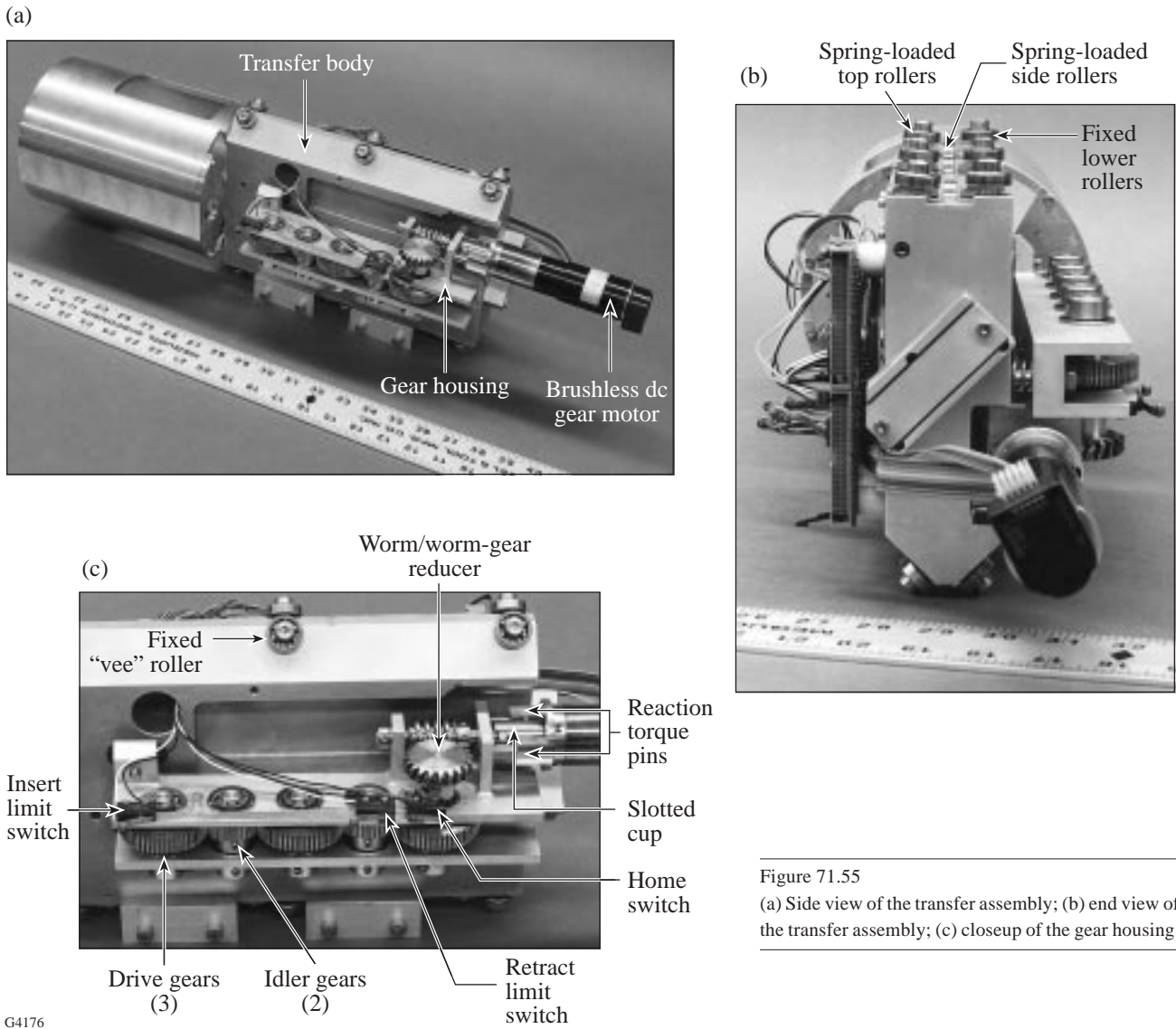


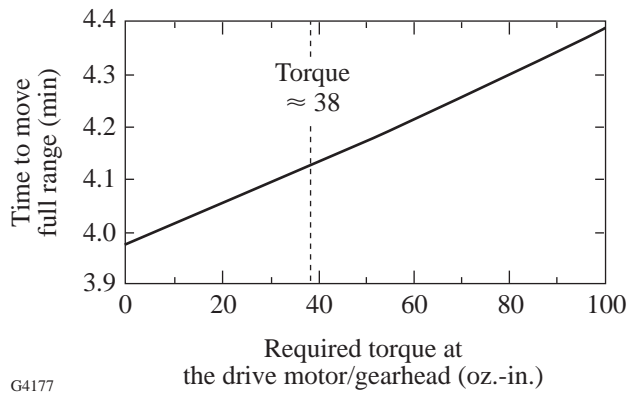
Figure 71.55
 (a) Side view of the transfer assembly; (b) end view of the transfer assembly; (c) closeup of the gear housing.

The drive motor for the transfer motion was initially a brush-style dc motor with integral gear head and magnetic encoder manufactured by MicroMo Electronics. The brushes have had poor lifetime in the high-vacuum environment, so the motors were replaced every 6 to 8 weeks to minimize the possibility of a failure during an experimental shot sequence. The transfer motion motor has now been replaced with a brushless dc motor manufactured by MicroMo [see Fig. 71.55(a)]. The gear head chosen for this application is a planetary style that provides robust performance and withstands the full stall torque of the motor. The gear head is cleaned and lubricated for vacuum service at LLE.

The motor is sized to provide a transit time to the TCC of less than 5 min. The weight of the shuttle is 25 lbs (the

estimated weight of the conceptual design was 27.3 lbs). The required torque at the motor/gear head was calculated from the estimated weight, and the motor's performance specifications (motor speed versus output torque) were used to calculate the shuttle's transit time for a range of torque settings. (These data are shown in Fig. 71.56.) The estimated torque for this application was ≈ 38 oz.-in. The transit time was estimated at 4.1 min and would increase to 4.3 min if twice the torque was required. Thus, the transit time is not a strong function of the torque required to move the shuttle.

The output shaft of the transfer motor is coupled to the drive gears with a 10:1 worm/worm-gear reducer, as shown in Fig. 71.55(c). This reducer provides the proper overall gear ratio for the drive motor and ensures that the transfer assembly



G4177

Figure 71.56
T-axis transit time versus torque required at the drive motor.

does not drive backward (due to gravity) when power is removed from the motor. The gear head on the motor is constructed with pressed-in shaft bearings, so the gear head cannot support the thrust loads generated by the worm/worm-gear reducer. These thrust loads required the worm to be mounted on a shaft, which is supported with adequate thrust-bearing capacity. The drive motor is coupled to the worm shaft by a slotted cup that engages the cross pin in the worm shaft. The reaction torque at the motor is taken by the two pins shown in Fig. 71.55(c). This arrangement allows the drive motor to be quickly removed from the gear housing and replaced in the event of a motor failure.

A belt drive was initially used to couple the two drive gears; however, this was abandoned because the belt could not be tensioned adequately for the load and the belt would slip as the transfer body moved across the gate-valve gap when the target positioner was mounted in a vertical orientation. A bevel-gear drive was also tried and dropped in favor of the compact and robust gear train shown in Fig. 71.55(c).

Motion along the T axis is restricted by limit switches that are activated at each end-of-travel [see Figs. 71.54(b) and 71.55(c)]. This motion uses an incremental encoder that must be zeroed at a repeatable location whenever power is lost to the controller. This switch is mounted with the end-of-travel limit switches and is tripped by the ramp for the retraction switch. In this manner, the T axis can be reset to home every time the transfer assembly is retracted from the TCC.

The brush-style drive motor initially used for the T axis incorporated a magnetic incremental encoder that produced 40 counts per revolution. This has been replaced with a brushless-

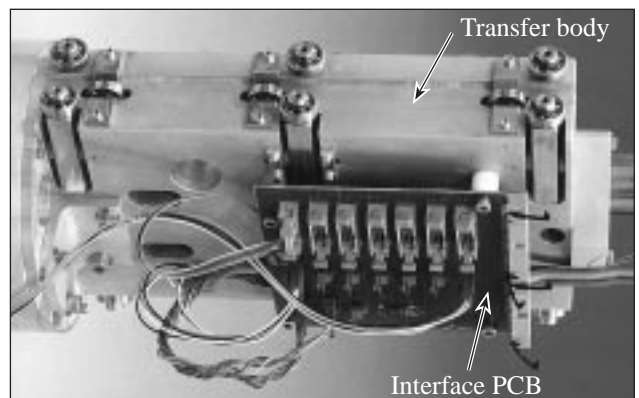
style drive motor, which uses an optical encoder that produces 384 counts per revolution. (See Table 71.IX for a summary of the resolution of the target-positioner motions.)

Table 71.IX: Calculated performance of the OMEGA target positioner.

Parameter	Specification	Final Value
T-axis resolution	1 mm	0.0125 mm
T-axis transit time	5 min	≈ 4 min
Z resolution	5 μm	0.1 μm
X and Y resolution	5 μm	0.8 μm
θ and φ resolution	0.25°	0.6 × 10 ⁻⁶ °
ω resolution	0.25°	0.004°

3. Cable Assembly

The cable assembly consists of two ribbon cables, a tensioning pulley, an interface printed circuit board (PCB) mounted to the transfer body, and two electrical vacuum feedthroughs mounted in the tee section of the guide tube assembly. This assembly provides power to the gear motors used for each of the alignment motions in the target positioner. It also provides feedback from the encoders and limit switches to the controller, which is remote from the target positioner. The tensioning pulley rides on the same rails as the transfer body. Two constant-force springs provide the necessary tension on the pulley to prevent the cables from tangling without producing excessive load on the transfer motion motor. The electrical feedthroughs are shown in Fig. 71.52 and the PCB in Fig. 71.57.



G4178

Figure 71.57
Printed circuit board on the transfer body.

Fine Positioning Motion

The final alignment of the target is accomplished with the fine-motion stages that provide four degrees of freedom: X , Y , Z , and ω (with the option of later adding θ and ϕ motions). These stages are cascaded from the transport assembly in the manner defined in the specification (see Fig. 71.49). All fine motions are powered with brush-style dc gear motors from MicroMo. The gear heads are a spur gear style with high ratios and fine resolution; however, these gear heads will not take the full stall torque of the motor: the output gear will break under a stall condition, and the gear head will need to be replaced.

1. Z Stage

The Z motion is supplied by a lead screw driving a yoke with three cylindrical pads [see Fig. 71.58(a)] that run on the inside of a 5.5-in.-inner-diam cylindrical housing (see Fig. 71.51). One of the pads is spring loaded against the cylindrical surface, and the other two pads are rigidly mounted to the yoke. This approach prevents binding during the full range of motion while maintaining accurate linear motion in any orientation. This design also allows the X - and Y -stage motors to be packaged within the volume of the Z motion, thus keeping the overall assembly compact and lightweight [see Fig. 71.58(b)]. A shoulder screw in the spring-loaded pad runs in a slit in the cylindrical housing to prevent rotation of the yoke [see Fig. 71.58(a)]. This screw also serves as the hard stop for the motion as well as the trip for limit switches [see Fig. 71.58(c)]. The lead screw provides 0.05 in. of translation per revolution, the motor gear head is a 272:1 ratio, and the transit time for the full range of travel (± 1 in.) is approximately 48 s. The final resolution of the Z stage is listed in Table 71.IX.

2. X and Y Stages

The X and Y linear motions of the target are approximated by rotating about two orthogonal axes located 18 in. from the target. This approach was used successfully on the earlier shuttle-style target positioner developed and used on the OMEGA 24-beam system. A two-axis gimbal is used to generate these motions. Each rotation axis is produced by using two 1/8-in.-diam silicon nitride balls in brass conical seats. The two balls are preloaded by using cone point set screws with locking jam nuts [see Fig. 71.59(a)]. The drive motion for each gimbal is provided by a lead screw, which is mounted directly on the output shaft of the motor/encoder/gear head, as shown in Fig. 71.59(b) for the X stage and Fig. 71.58(b) for the Y stage. The lead screw provides 0.05 in. of motion per revolution; this yields a rotation of 2.35° because the lead screw is offset 1.218 in. from the pivot axis of the gimbal. The gear head is a spur gear style with a 1670:1 ratio to provide the required

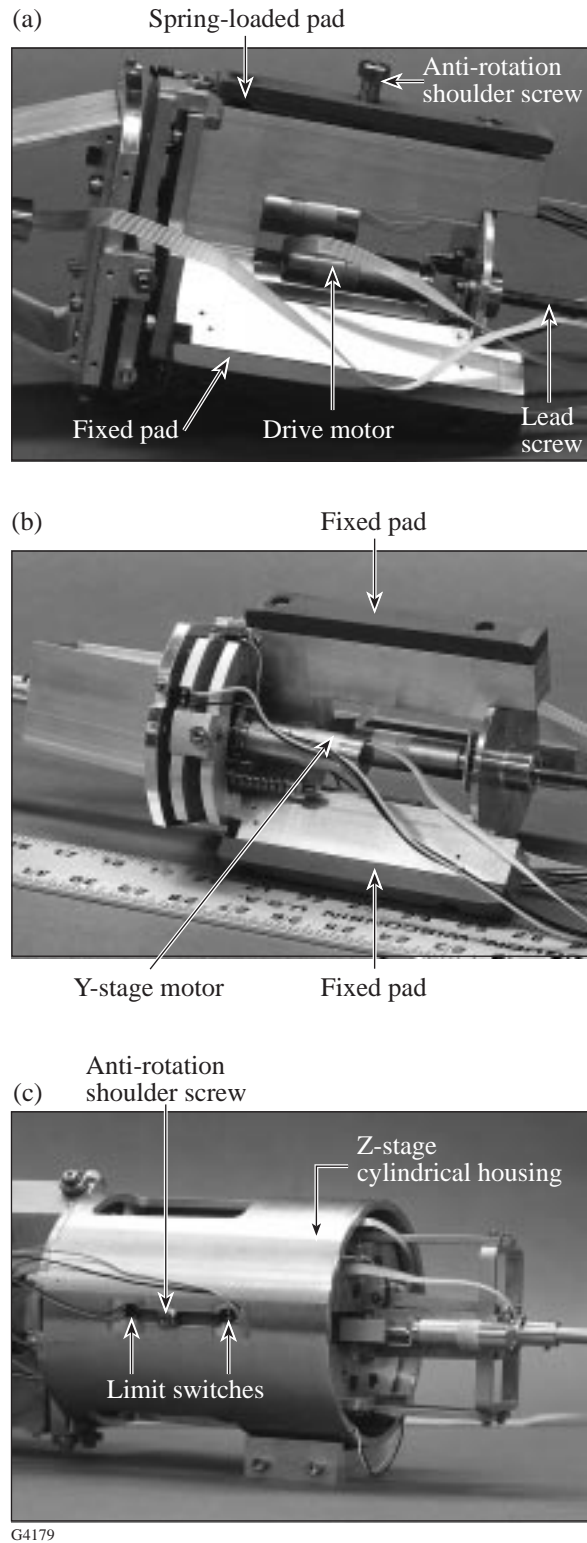


Figure 71.58 (a) Z-stage yolk assembly; (b) Y-stage motor packaged within the Z-stage yolk assembly; (c) Z-stage limit switches.

resolution for the X and Y motions. The motor-mounting plate is slotted to allow the motor/lead screw to translate as the screw is turned; the reaction torque on the motor is taken by two pins in the base plate, which ride in slots in the motor-mounting plate. The lead screw nut is mounted in the base plate. The gimbal plate is spring loaded against the lead screw to eliminate backlash. The tip of the lead screw is an 1/8-in.-diam silicon nitride ball, which seats against a flat hardened-steel pad in the gimbal plate. The base plate for the X stage is rigidly

attached to the yoke of the Z stage. The gimbal plate of the X stage is also the base plate for the Y stage. This concept allows a compact, simple package for the two translation motions at the TCC. Although this style of motion leads to coupling of the X and Y motions to the Z motion, system operators quickly learn to compensate for this coupling, which does not exceed 0.03 in. of Z motion over the full range of X or Y travel. The final resolutions of the X and Y stages are listed in Table 71.IX.

3. OMEGA Stage

The ω motion is rotation about the axis of the target positioner. The motor/encoder/gear head is the same as used on the X and Y stages. A 1/4-in.-diam drive shaft is rigidly coupled to the gear head output shaft, and the end of the drive shaft closest to the target is supported with a polymer sleeve bearing. A target holder threaded to the end of the drive shaft (Fig. 71.60) holds the target mount with a beryllium copper spring finger. The first plasma shield shown in Fig. 71.60 prevents ablation of the sleeve bearing, which supports the drive shaft. The second plasma shield provides line-of-sight protection for the remainder of the target positioner. The ω axis is supported from the Y -axis gimbal plate with a spacer as shown in Fig. 71.59(b). This spacer can be replaced with the θ and ϕ stages, which are described in the next section (see Fig. 71.51). The final resolution of the ω axis is listed in Table 71.IX.

4. θ and ϕ Stages

The OMEGA target-positioner specification requested the additional rotational motions θ and ϕ to allow precise alignment of nonspherical targets. These motions need to provide

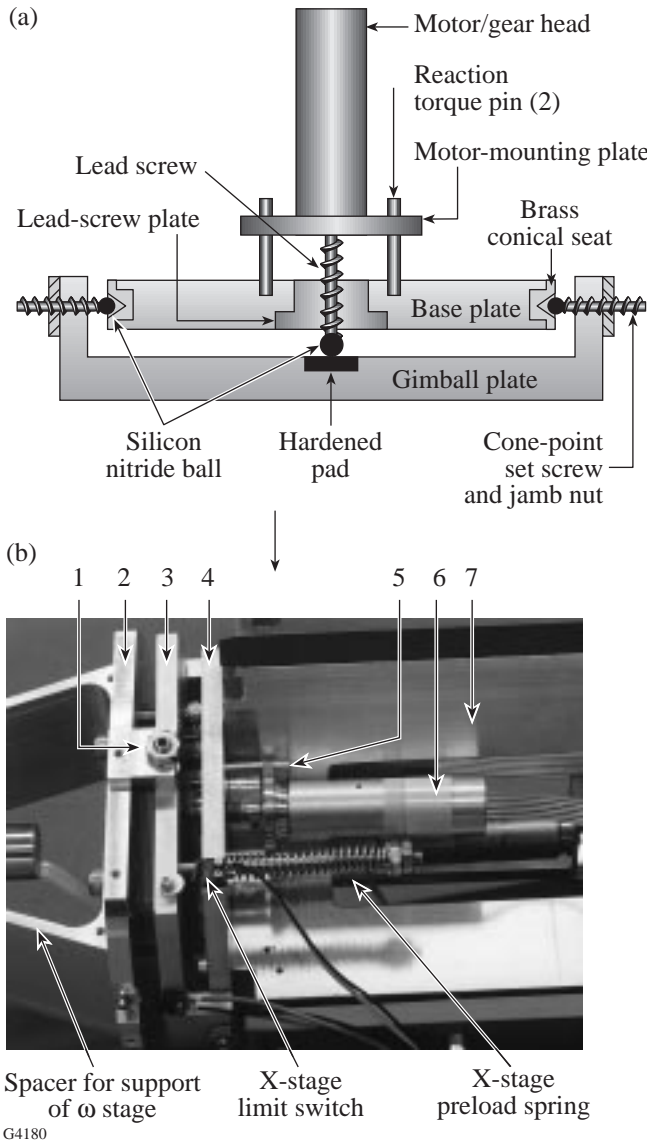


Figure 71.59
 (a) X -, Y -stage concept; (b) X -, Y -stage closeup. (1) Y -stage cone-point set screw and jamb nut; (2) Y -stage Gimbal plate; (3) X -stage Gimbal plate; Y -stage base plate; (4) X -stage base plate; (5) reaction torque pin; (6) X -stage drive motor; (7) Z -stage yolk.

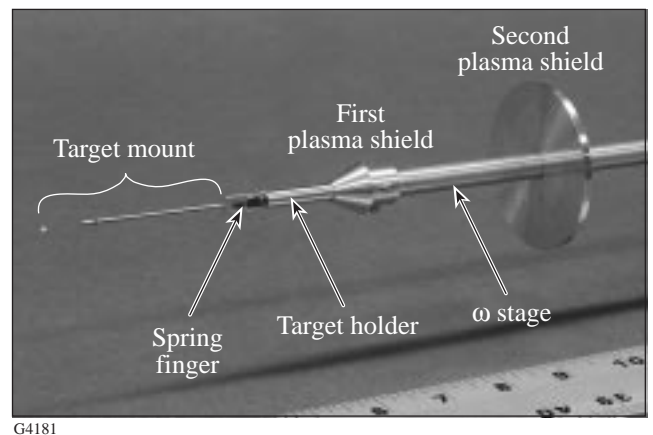


Figure 71.60
 Closeup of the target holder and plasma shields.

$\pm 5^\circ$ of rotation about the TCC; historically, this was accomplished with goniometric stages. Goniometric stages are difficult to package in the space envelope of the target positioner, so an alternative approach was developed using four-bar linkages. The geometry of these linkages is shown in Fig. 71.61(a).¹ This concept supports the ω axis on the bar labeled c in Fig. 71.61(a), so the rotation angle of the target located at the end of the ω axis is defined as θ . The law of cosines yields the following relationships for the four-bar linkages:

$$\psi = \cos^{-1}\left(\frac{h^2 + a^2 - b^2}{2ha}\right) + \cos^{-1}\left(\frac{h^2 + d^2 - c^2}{2hd}\right), \quad (1)$$

$$\tau = \cos^{-1}\left(\frac{c^2 + d^2 - a^2 - b^2 - 2ab \cos \phi}{2cd}\right), \quad (2)$$

$$h^2 = a^2 + b^2 + 2ab \cos \phi, \quad (3)$$

where ϕ is referred to as the crank angle.

The target's angle of rotation is

$$\theta = \pi - (\tau + \psi). \quad (4)$$

The location of a point P relative to the origin shown in Fig. 71.61(a) is

$$P_x = b \cos(\phi) + r \cos(\theta + \alpha), \quad (5)$$

$$P_y = b \sin(\phi) + r \sin(\theta + \alpha). \quad (6)$$

In the design of the θ and ϕ mechanisms the links shown as b and d in Fig. 71.61(a) are equal in length, and the geometry of the mechanism for the OMEGA target positioner, as shown in Fig. 71.61(b), yields the following relationships:

$$c = u \left(\frac{a}{u+w} \right), \quad (7)$$

$$b = \frac{w}{\cos \left[\tan^{-1} \left(\frac{a/2}{u+w} \right) \right]}, \quad (8)$$

$$\alpha = \tan^{-1} \left[\frac{u}{c/2} \right], \quad (9)$$

$$r = \frac{u}{\sin \alpha}, \quad (10)$$

where the linkage is designed to provide rotation about the remote point P , shown in Fig. 71.61(a). By defining the variables a (width between the fixed pivots), w (height of the mechanism), and u (distance from the mechanism to the

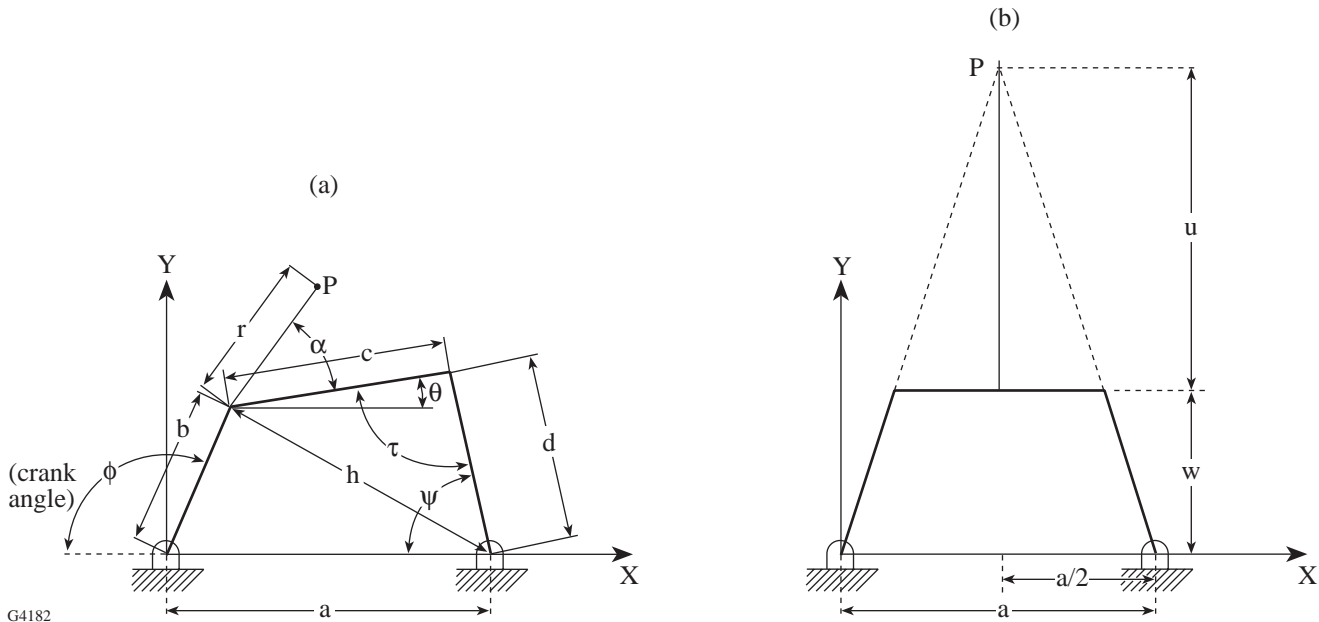


Figure 71.61
(a) Four-bar linkage geometry; (b) θ -and ϕ -stage geometry.

target), one may numerically solve for the angle of the target, θ , as a function of the crank angle ϕ by using Eqs. (7)–(10) and Eqs. (1)–(4). This has been done to understand the motion for various design dimensions, and the final design parameters are given in Table 71.X for both the θ and ϕ stages. The relationship of the rotation angle of the target to the rotation of the crank is nearly linear, as shown in Fig. 71.62. Equations (5) and (6) are used to calculate the movement of the target in the axial and lateral directions over the rotation range of 5° . These results are given in Figs. 71.63(a) and 71.63(b).

The θ and ϕ stages have been built in a nested fashion to minimize the size of the assembly and allow it to fit in the allotted space between the X/Y stages and the ω stage [see Figs. 71.64(a) and 71.64(b)]. Both the θ and ϕ stages are driven by the same dc gear motors as the X and Y stages. These motors are coupled to the stage crank shafts using a worm/worm-gear reducer. The θ motor is packaged within the Z -stage yolk (see Fig. 71.64); the ϕ -motor location is shown in Fig. 71.64(b). The final resolution of the θ and ϕ stages is listed in Table 71.IX.

Table 71.X: Final design parameters for the θ and ϕ axes.

Parameter	θ Stage	ϕ Stage
u (in.)	12.00	11.97
w (in.)	3.50	3.00
a (in.)	1.25	1.25

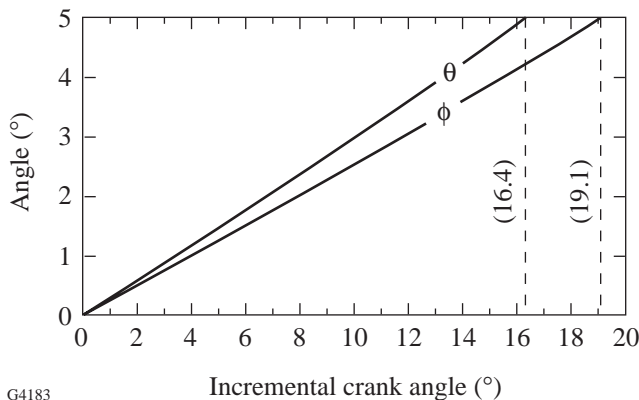


Figure 71.62
 θ and ϕ rotation versus crank angle.

Controls

1. Operator Interface

The experimental system operator (ESO) controls the TPS/TVS through a graphical user interface (GUI) residing on a computer terminal located in the control room (see Fig. 71.65). This GUI displays push buttons for control of TPS motions including selection of jog modes, direction, and jog-step size. Values representing the actual (implied) absolute position of each axis are useful. In addition, feedback of actual position within range (and/or limit-switch status) is displayed for each axis. The window provides for actuation of shutters, selection of illumination intensity, magnification option, and enhanced video options, etc., for TVS control.

2. Target-Positioner Control Elements

The OMEGA target positioner is comprised of two discrete and operationally independent functional areas (see Fig. 71.66): (1) the auxiliary vacuum controls that control entry into the target chamber while remaining under a high vacuum condition, and (2) the multiple-axis motion controller necessary for precision motion control of up to six individual axes.

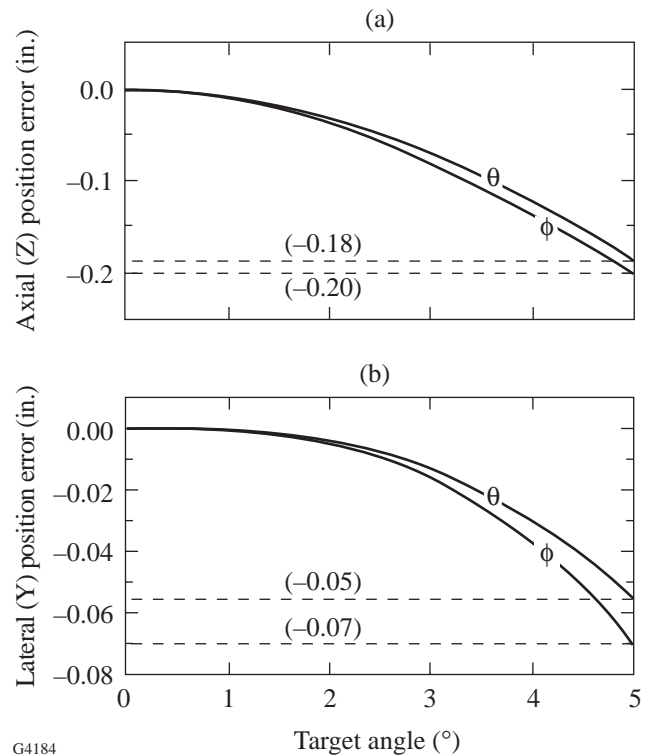
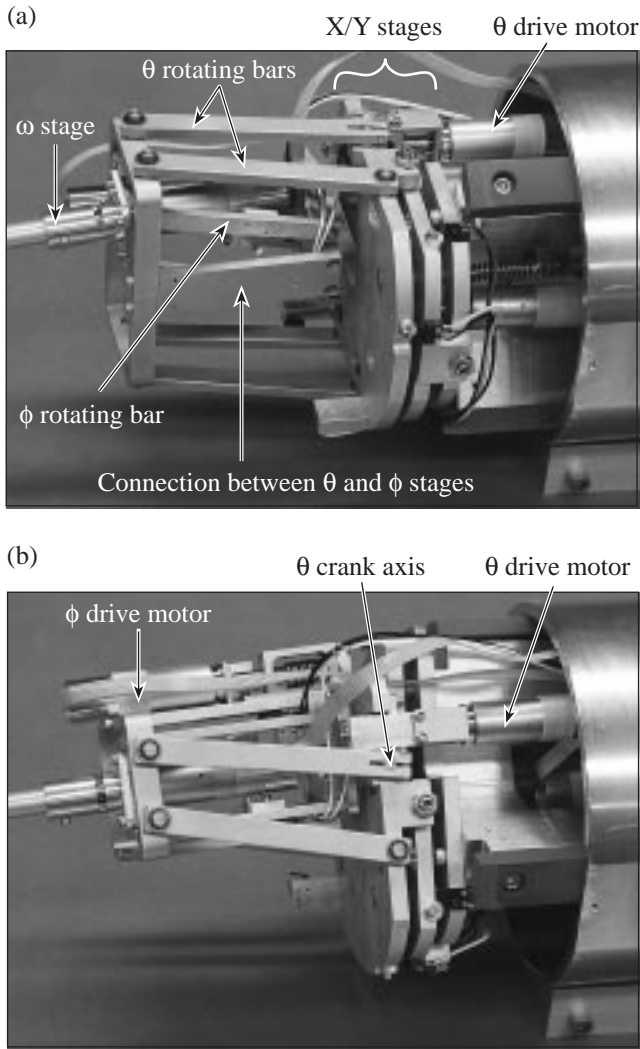


Figure 71.63
(a) θ and ϕ axial position error; (b) θ and ϕ lateral position error.



G4185

Target-Positioner Auxiliary Vacuum Controls

The primary function of the auxiliary vacuum controls is to sequence the pumps, solenoid valves, and an 8-in. gate valve such that the positioner, loaded with a target, may be inserted inside the target chamber without perturbing the chamber's high-quality vacuum condition. The process involves network communications with other auxiliary vacuum controllers to arbitrate the sharing of the roughing pump manifold resource. In addition, the auxiliary vacuum controls provide a remote control and monitor of TPS functions both in the control room and locally at the target chamber's personnel platform.

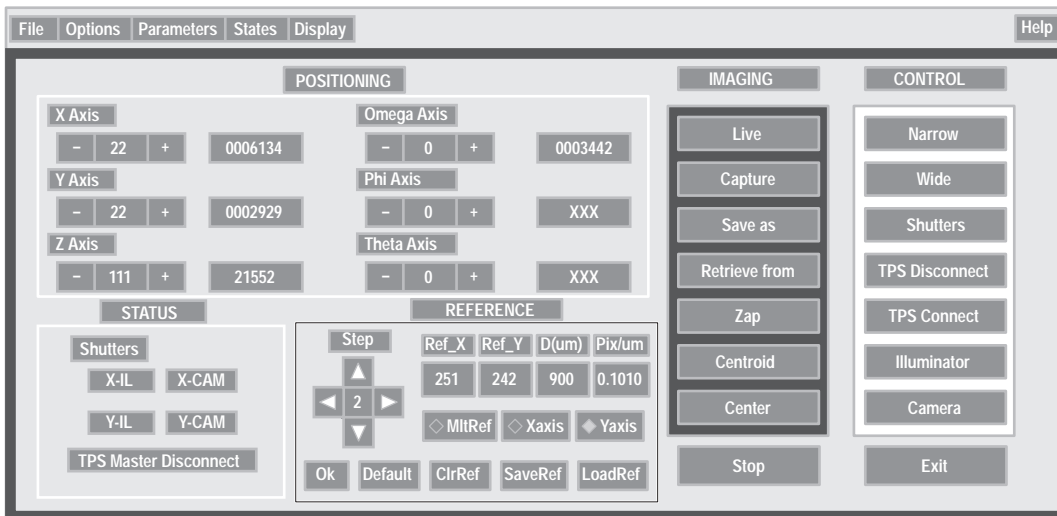
During airlock evacuation the auxiliary vacuum controls monitor a vacuum sensor to automatically sequence from rough pumping to turbo pumping operation. Once the airlock is properly evacuated and insertion has been commanded, the gate valve is opened, enabling the transport axis motion. The controls establish the "home reference position" to the transport motion axis to maintain coarse positioning accuracy to within ± 0.001 in. over an 80-in. range of travel in order to arrive within the video capture range of the TVS.

Target-Positioner Precision Motion Controller

OMEGA's TPS motion controller provides the control elements for the X, Y, Z, θ , ϕ , and ω axes that provide precise alignment and rotation of the target to the center of the

Figure 71.64

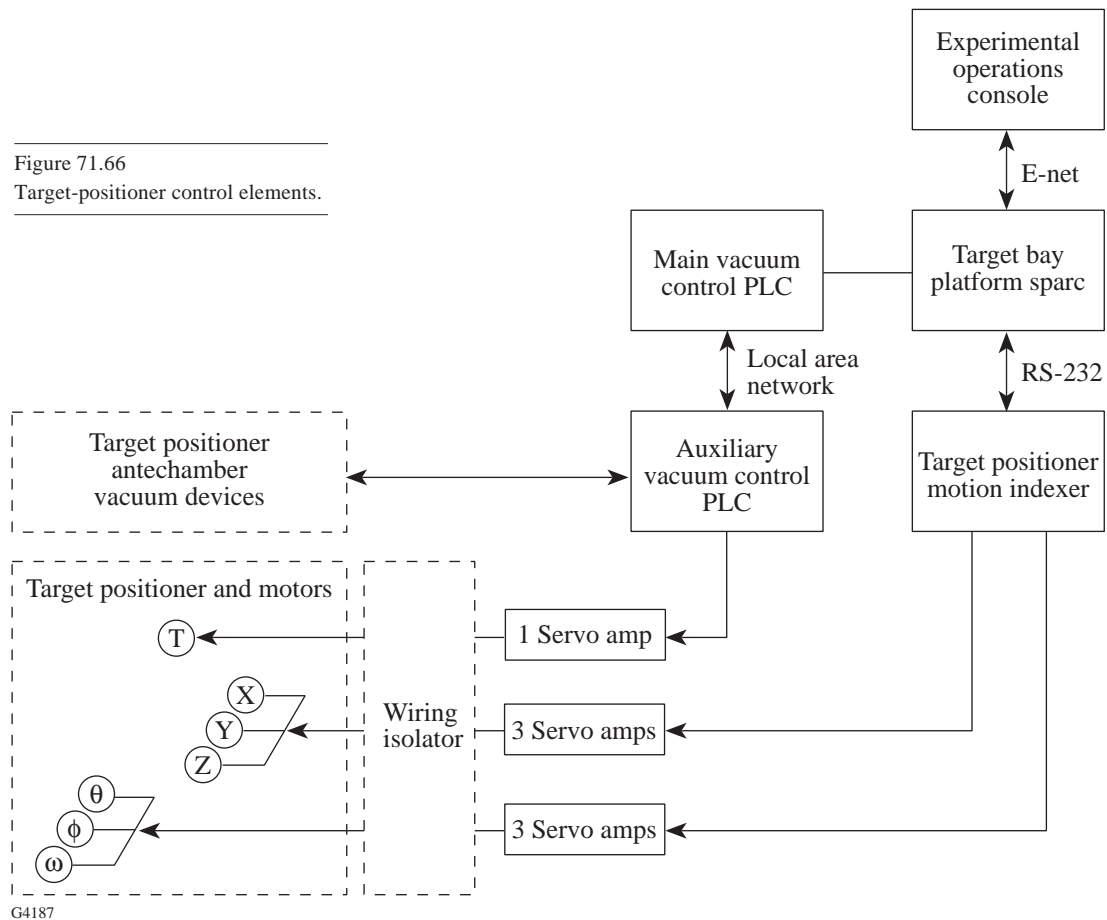
(a) θ and ϕ stages; (b) ϕ -stage drive-motor mounting.



G4186

Figure 71.65
TPS graphical user interface.

Figure 71.66
Target-positioner control elements.



chamber. These six independent functions are provided from a commercially available unit purchased from Galil Motion Control, Inc. Motion instructions are issued via a serial data communication link from the experimental executive computer to the Galil motion controller during alignment operations. The Galil instruction set is based on an ASCII format and includes programmable variables for servo parameters such as gain, velocity, acceleration, and filter terms. These and other parameters are retained in static zero power RAM for convenience.

A motion controller is a part of a closed-loop servo system, which also includes a power amplifier, motor, and encoder. A typical closed-loop-position servo system is shown in Fig. 71.67. The controller is the element that initiates motion by generating an analog command signal that, when applied to the power amplifier, results in an electric current flowing in the motor windings. This current creates torque and subsequent mechanical motion. The encoder senses the position change in the motor and feeds this information back to the controller, which tracks the motion progress over time.

Incremental encoders operate by generating output pulses that represent the motor shaft position and include two signals that, for the case of the TPS, generate ten pulses per revolution. The two signals are displaced by 90° in phase, which enables the controller to determine the direction of rotation according to which signal leads or lags the other. Motor displacement can therefore be determined by counting the number of pulses, and the frequency of the resultant pulse train is proportional to motor velocity.

The controller performs the basic intelligent operations of the system:

- interpreting commands sent from the host computer (experimental executive) via a serial communication interface,
- generating the command signal profile,
- decoding position-feedback information into motion displacement and velocity,

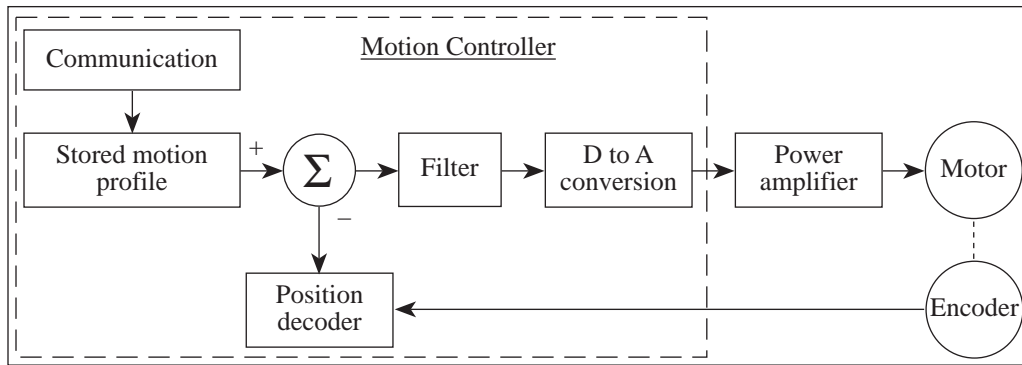


Figure 71.67
Typical closed-loop-position servo system.

E8617

- closing the position loop,
- compensating the loop by filtering to achieve stability and prevent oscillation, and
- interpreting end-of-travel limit switches to prevent possible damage to the motion mechanisms.

Command Profile

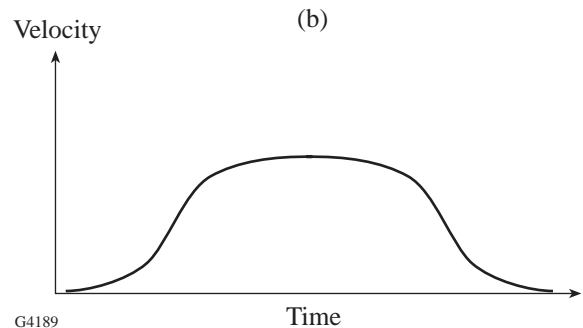
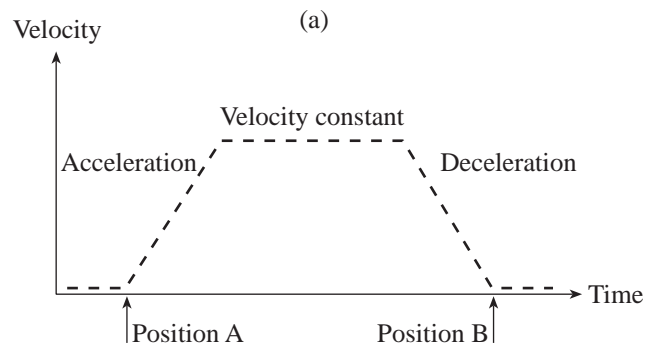
The target is suspended at the end of the target-positioner mechanism from a carbon fiber, which is several microns in diameter. The mass of the stalk is kept intentionally low, and the resultant thin structure is extremely fragile. Consequently, the controller must deliver smooth and reliable motion to minimize (lateral) forces applied to the target and its stalk during alignment procedures. Sudden TPS accelerations or decelerations must be limited to levels that ensure the stalk does not break or the target does not become dislodged from the stalk.

A “trapezoidal velocity profile” applies a linear function to the motor that provides continuous acceleration to maximum velocity and continuous deceleration to a full stop [Fig. 71.68(a)]. However, a more complex command profile known as an “S curve” [Fig. 71.68(b)] is sometimes preferred because it imparts a smoother, less-instantaneous acceleration change.

To date, the TPS controller has utilized the trapezoidal velocity profile successfully. However, should future targets or their stalks become more sensitive to acceleration forces, the controller is capable of generating S-curve velocity profiles.

Compound Coordinated Motions

The mechanical design of the ϕ and θ axes couples ϕ rotation with X and Z motions and θ rotation with Y and Z motions as discussed in a previous section. If the ϕ or θ axes are moved to the full range of motion, the target will shift outside the capture range of the TVS. For this reason a motion controller



G4189

Figure 71.68
(a) Trapezoid velocity profile; (b) S-curve velocity profile.

was selected that is capable of implementing electronic gearing where one or more axes are slaved to follow a master axis at a fixed ratio, thereby providing a motion vector.

Wiring Isolator

Early operational experience with the OMEGA target positioner confirmed that the supporting electronics systems and components were prone to damage from the laser-fusion event. During the event, laser energy is incident upon the target and the tip of the target stalk. This creates a transient high-temperature plasma comprised of charged particles, some of which recombine while others fly in all directions. The electrons, being the lightest, travel at the highest velocity to the target chamber walls. The target-positioner mechanism being the closest conductive mass near the center of the target chamber intercepts a significant portion of these charges, which can couple back into control circuitry of the TPS. The transient nature of this electrical phenomenon occurring with typically nanosecond rise times can damage semiconductor components and perturb information stored in memory devices. These effects require that the wiring and cabling in the target chamber interior be shielded from line-of-sight particles and that the remote electronics be isolated from the TPS using a disconnect switch. Just prior to the shot, relay contacts open in each of the 70+ conductors in the wiring harness to protect the control electronics. After the shot the relay is commanded closed once again, thereby enabling the TPS retrieval process.

Summary

The OMEGA target positioner has been developed to provide a means of positioning a target at the TCC and precisely aligning this target using up to 4° of freedom, X , Y , Z , and ω . A compact two-axis stage was developed to provide θ and ϕ rotation of the target, but this stage is not currently used on OMEGA.

All motions are servo controlled, and a GUI is used in the OMEGA control room to provide convenient control of the target positioner.

The OMEGA target positioner has been used to support and align a wide variety of targets in the experimental chamber including spherical implosion targets, multiple flat-foil instability targets, and hohlraums for indirect-drive experiments.

ACKNOWLEDGMENT

This work was supported by the U.S. Department of Energy Office of Inertial Confinement Fusion under Cooperative Agreement No. DE-FC03-92SF19460, the University of Rochester, and the New York State Energy Research and Development Authority. The support of DOE does not constitute an endorsement by DOE of the views expressed in this article.

REFERENCES

1. J. E. Shigley and C. R. Mischke, *Standard Handbook of Machine Design* (McGraw-Hill, New York, 1986).